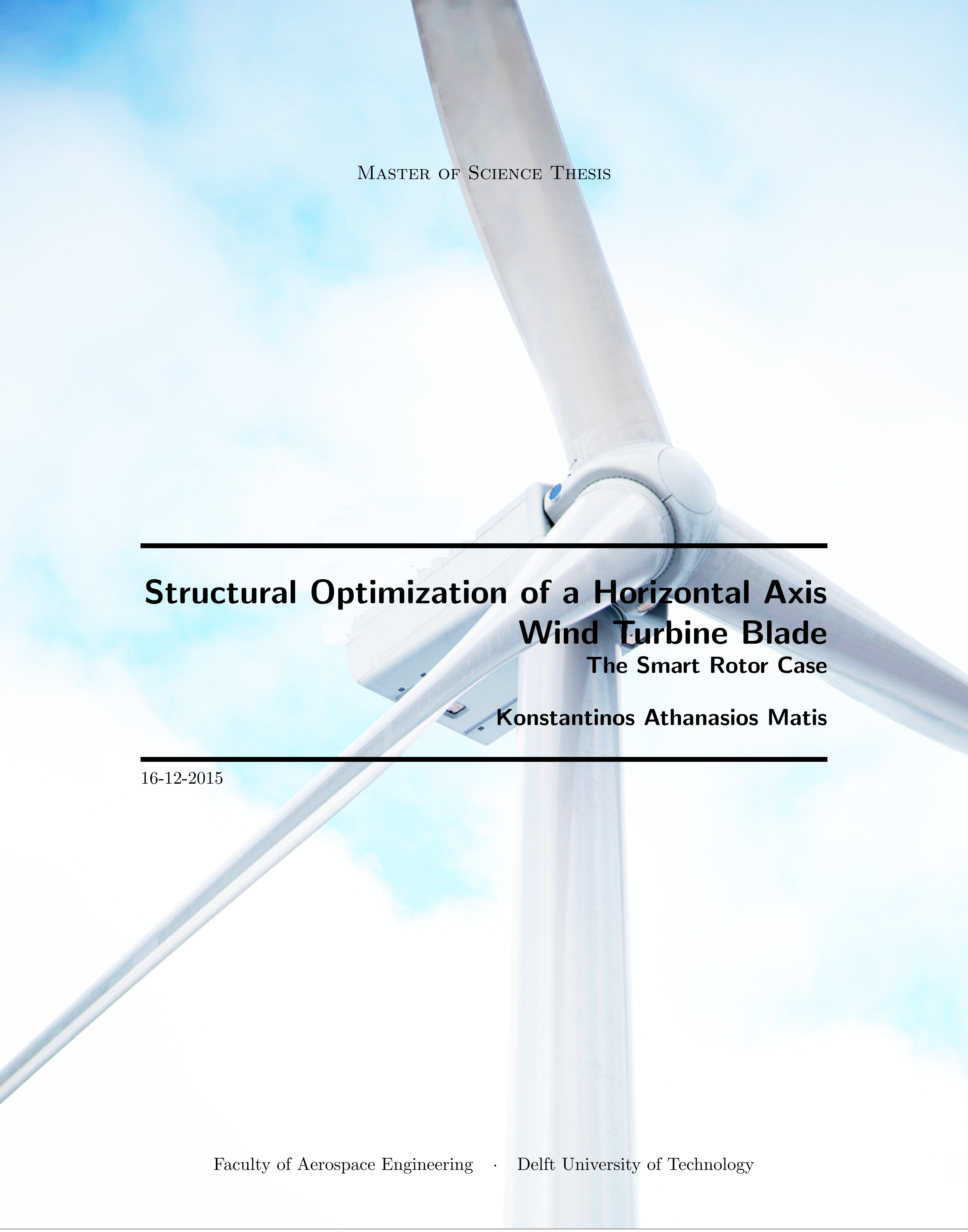

Master of Science Thesis

Structural Optimization of a Horizontal Axis Wind Turbine Blade

The Smart Rotor Case

Konstantinos Athanasios Matis

16-12-2015

Faculty of Aerospace Engineering · Delft University of Technology

Challenge the future

Structural Optimization of a Horizontal Axis Wind Turbine Blade

The Smart Rotor Case

MASTER OF SCIENCE THESIS

For obtaining the degree of Master of Science in Sustainable Energy Technology at Delft University of Technology

Konstantinos Athanasios Matis

16-12-2015

Faculty of Aerospace Engineering · Delft University of Technology

Delft
University of
Technology

Delft University Of Technology
Department Of
Wind Energy

The undersigned hereby certify that they have read and recommend to the Faculty of Aerospace Engineering and Faculty of Applied Sciences for acceptance a thesis entitled **"Structural Optimization of a Horizontal Axis Wind Turbine Blade"** by **Konstantinos Athanasios Matis** in partial fulfillment of the requirements for the degree of **Master of Science**.

Dated: 16-12-2015

Head of department: Prof. Dr. G.J.W. van Bussel

Supervisor: Dr. Ir. W.A.A.M. Bierbooms

Dr. Ir. L.O. Bernhammer

Reader: Dr. C. Kassapoglou

Summary

The main purpose of this project was the creation of a tool, based on the research performed by Scheldbergen [25] and Roscher [24], capable of performing Finite Element Analysis (FEA) on a Horizontal Axis Wind Turbine (HAWT) blade and minimize its weight by altering the various thicknesses locally, always satisfying a number of structural constraints.

The first goal was the development of a geometry creation algorithm based on a Non Uniform Rational Basis Splines (NURBS) algorithm developed by Ferede [14], with a more complex spanwise/chordwise discretization technique in order to more accurately design a discretized HAWT blade. The second goal was the alteration of the material creation algorithm developed by Scheldbergen [25], so that different stacks at various blade locations can be assigned. Moreover, the aerodynamic loads generation algorithm of Scheldbergen [25] was modified to apply for different airfoils along the blade span. Also, Blade Element Momentum (BEM) theory was used for the calculation of the aerodynamic loads and the software XFOIL was used for the aerodynamic analysis of the airfoils (pressure distribution on the airfoil at corresponding angles of attack and Re numbers).

An initial HAWT blade design was created, matching the SANDIA 5 MW wind turbine blade [23] geometry and materials. Furthermore, the flapwise/edgewise stiffness, moments of inertia, mass and mode shapes were also validated. Additionally, the SANDIA blade was analyzed in DNV GL Bladed in order to validate the aerodynamic loads on the blade.

Following, the tool was designed to process the geometry, the materials and the gravitational/centrifugal/aerodynamic loads of the blade and translate them to an input for the FEA software MSC Nastran for Linear Static Analysis (SOL 101), Buckling Analysis (SOL 105) and Modal Analysis (SOL 103). The post processing algorithm of Scheldbergen [25] was modified to apply for a HAWT (instead of a VAWT), transforming the results of the FEA analysis into optimization constraints (ultimate load, buckling, tip deflection and fatigue). The final part of the algorithm involved the minimization of the blade's mass by altering the thickness at various locations, using the MATLAB function fmincon.

Concluding, a case study of a smart rotor blade equipped with trailing edge flap (TRF) was examined. A ± 2° flap was used at 90-100% of the chord and 78-98% of the span. Two kinds of optimization were performed for the HAWT and smart rotor scenarios; one that included ultimate stress, tip deflection and fatigue constraints (UL-TD-FA) and one that also included buckling constraints (UL-BU-TD-FA). It was found that the buckling constraint was the limiting factor of the optimization and the fatigue constraint was the least dominant. The initial design of the smart rotor blade showed a **16.5% decrease** of the maximum **fatigue damage** and a **2% decrease** in the **maximum stress**. The optimized smart rotor blade mass was 0.5 % lower in the UL-TD-FA scenario and 2.5% in the UL-BU-TD-FA scenario compared to the HAWT blade.

The tool created is capable of creating a flexible and fairly accurate representation of a HAWT and smart rotor blade. It also provides the ability to structurally analyze the blade under the most significant structural criteria and minimize the blade's weight under specific loading conditions. The tool constitutes a good starting point for more detailed structural analysis of smart rotors and more complex structural optimization of HAWT and smart rotor blades.

Acknowledgements

During the time I spent working on the MSc thesis project, I realized that its completion would not have been possible without the assistance of other people. Hence, I would like to give my acknowledgments to those who were involved and supported me in my thesis.

I would like to express my deepest gratitude to my supervisor Lars Oliver Bernhammer for trusting me with this interesting and exciting subject and helping me to extend my knowledge on wind turbines, structural design and finite elements.

Lastly, I would like to thank my family for believing in me and for supporting me both financially and emotionally through all these years, and my friends for the great time we had together.

Delft, The Netherlands
16-12-2015

Konstantinos Athanasios Matis

Contents

List of Figures

List of Tables

Nomenclature

Latin Symbols

A	Membrane stiffness matrix from classical laminate theory	$-$
Aeq	Matrix for linear equality constraints	$-$
AOA	Angle of attack	deg
b	Inverse slope of the S-N fatigue life curve	$-$
beq	Vector for linear equality constraints	$-$
C	Viscous damping matrix.	$-$
$c(x)$	Non-linear inequality constraints.	$-$
C_p	Pressure coefficient	$-$
$ceq(x))$	Non-linear equality constraints	$-$
D	Bending stiffness matrix from classical laminate theory	$-$
d	Width of the airfoil at each position	m
E	Elastic modulus	Pa
EI_{edge}	Edgewise stiffness	Pam^4
EI_{flap}	Flapwise stiffness	Pam^4
F	Force	N
f	Prandtl correction factor	$-$
F_D	Fatigue damage	$-$
h_c	Thickness of the sandwich core material	m
h_f	Thickness of the sandwich panel material	m
h_{ref}	Reference height	m
I_{edge}	Edgewise area moment of inertia	m^4
I_{flap}	Flapwise area moment of inertia	m^4
I_{medge}	Edgewise mass moment of inertia	kgm^2
I_{mflap}	Flapwise mass moment of inertia	kgm^2

k	Inter-element continuity factor	$-$
lb	Vector of lower bounds on the design vector	$-$
M	Bending moment	Nm
m	Mass	kg
n	Number of layers	$-$
N_f	Number of cycles to failure	$-$
n_i	Number of cycles at a stress level i	$-$
P	Polynomial degree	$-$
p	Dynamic pressure	Pa
R	Blade radius	m
r	Local position on the blade's span	m
S	Allowable shear stress	Pa
t	Thickness of an element	m
TD_{all}	Allowable tip deflection	m
u	Displacement	m
ub	Vector of upper bounds on the design vector	$-$
v_{inf}	Wind velocity	$\frac{m}{s}$
v_{rot}	Rotational velocity	$\frac{m}{s}$
v_r	Resultant velocity	$\frac{m}{s}$
w	Layer number	$-$
x	Design Variable	$-$
X_c	Allowable compressive stress in x-direction	Pa
x_{hinge}	x coordinate of hinge point of an airfoil	$-$
x_{TE}	x coordinate of the trailing edge of an airfoil	$-$
X_t	Allowable tensile stress in x-direction	Pa
Y_c	Allowable compressive stress in y-direction	Pa
Y_t	Allowable tensile stress in y-direction	Pa
z_0	Relative roughness	$-$
Greek Symbols		
γ_f	Partial safety factor for loads	$-$
γ_m	Partial safety factor for materials	$-$
μ	Air's dynamic viscosity	$\frac{kgs}{m^2}$
ν_{xy}	Poisson ratio	$-$
ω	Natural frequency.	rad/s
ϕ	Inflow angle	deg
ρ	Density	kg/m^3
$\sigma_{x,y}$	Stress in the x,y direction	Pa
τ_{xy}	Shear stress	Pa

ε	Strain	–

Abbreviations

BU	Buckling
$CFRP$	Carbon Fiber Reinforced Plastic
EV	Buckling eigenvalues
FA	Fatigue
FEA	Finite Element Analysis
FI	Failure index
$GFRP$	Glass Fiber Reinforced Plastic
$HAWT$	Horizontal Axis Wind Turbine
$NURBS$	Non-Uniform Rational Basis Splines
SF	Safety factor
TD	Tip Deflection
US	Ultimate Stress
$VAWT$	Vertical Axis Wind Turbine

Chapter 1

Introduction

A significant amount of the power produced and consumed today in Europe comes from wind turbines. The European Commission published in October 2009 a plan where 20% of EU electricity's demand would be covered from wind turbines by 2020 (265 GW) and 33% by 2030 (400GW). This means that an increase of 15% by 2020 and 28% by 2030 in power production will have to be achieved. Furthermore, a part of the plan is to produce 55 GW by 2020 and 150 GW by 2030 from offshore wind farms. In order to achieve this target, the wind industry and research institutes have focused on developing new technologies to create larger wind turbines and at the same time attain a low cost and high lifetime. Ashuri [5], argues:

1. It is a fact that offshore winds are stronger and more stable that onshore which leads to higher energy production of a wind turbine.
2. It is also a fact that the energy capture per land area is higher for larger machines.
3. If fewer and larger wind turbines are used in a wind farms (for the same power),then several costs like operation and maintenance or infrastructure could be decreased significantly.

However, there are several obstacles in the upscaling of wind turbines. Among the most significant obstacles are the high aerodynamic forces encountered by large wind turbines blades. A concept to reduce the aerodynamic loads and at the same time achieve a more effective control of the blade's loading was introduced the past decades. This concept was influenced by the airplane industry and dealt with the use of active aerodynamic devices on the blades. Rotors that will use this kind of devices come by the name 'smart rotors'. The past decade numerous concepts have been investigated by research institutes about the establishment of active aeroelastic devices on wind turbines; however, no blade equipped with such devices has been constructed on industrial scale till today. In order for this to happen, it should be proven that the benefits of smart rotors are such that they increase the ratio of the energy produced to total cost. As it will be described in chapter 2, current research has shown that the introduction of smart rotors may reduce the variation of the loads exerted on the blade, since they can alter the lift locally which affects the ultimate loads, buckling, tip deflection and mostly fatigue loads.

This thesis project is a part of the ongoing research on the advantages/disadvantages of smart rotors compared to the conventional HAWT blades. The concept of this research is to analyze the structural benefits of a wind turbine blade equipped with railing edge flaps (TRF) by designing a MATLAB tool capable of performing structural analysis. In 2013 a complex tool was developed by Schelbergen [25] for structural optimization on Vertical Axis Wind Turbines (VAWT) and was modified in 2014 by Roscher [24]. The initial goal of the current research was to modify and evolve this tool in order to apply for a HAWT and a more realistic blade design. Significant alterations and additions were implemented on this algorithm in order to represent the blade's geometry more accurately, increase the meshing options and develop more complex composite material stacks and aerodynamic loading.

After that, the determination of the structural integrity of the designed blade was required and the minimization of the blade's mass. To do so, a post processing MATLAB code had to be further developed capable of calling the FEA software MSC Nastran, translate the FEA results into structural constraints and perform the optimization using the MATLAB function fmincon. The final blade design would be that with the minimum mass that does not fail under a number of specified failure criteria. Once the conventional blade was designed, structurally analyzed and optimized, the final goal of this project concerned the creation of a smart rotor blade and comparison between the two designs.

The main reasoning behind the tool can be understood by dividing it into five sub processes as shown in figure 1.1. In the first process, the user defines a set of inputs which characterize the blade's geometry, the applied materials, the aerodynamic loads/operational conditions and the optimization parameters. Following, these inputs are transformed into the appropriate format for FEA in MSC Nastran. The methodology behind the blade model development and its translation to the FEA input is analyzed thoroughly in chapter 3. The third and fourth stage of the algorithm are analytically explained in chapter 4 and involve the execution of MSC Nastran and the post processing of the results into optimization constraints. At the same chapter the optimization technique is elucidated. Concluding, at chapter 6 the results of the structural optimization for the conventional and the smart rotor blade are presented, explained and compared.

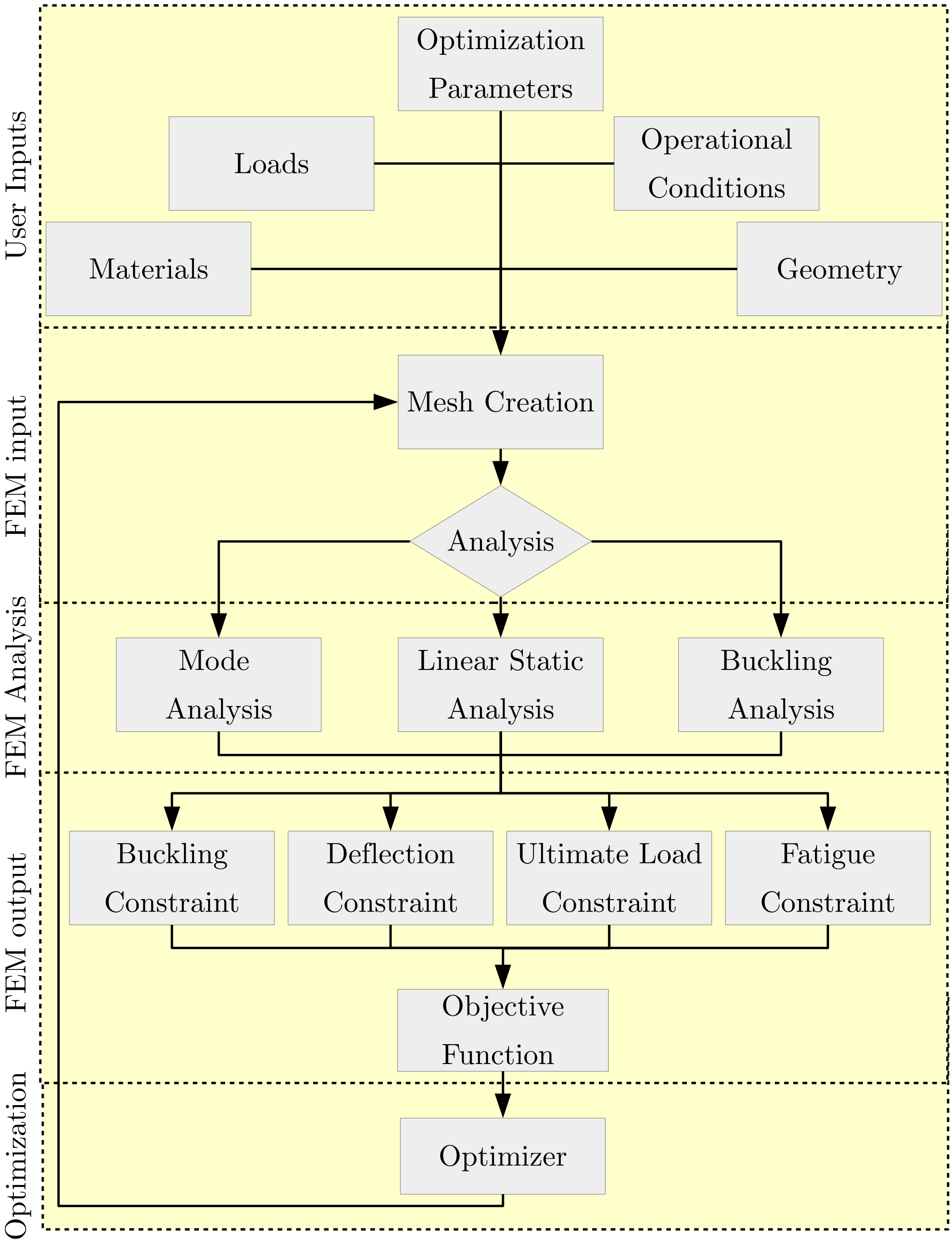

Figure 1.1: Tool stages flowchart

Chapter 2

Literature Review

Among the most significant aspects in rotor design is the development of control techniques and algorithms. Industrial turbines include two main control mechanisms. The first alters the orientation of the blade (pitch) according to the wind's velocity, direction and the second adjusts the generator's torque through a power electronics converter. All control techniques serve the purpose of either power regulation and speed adjustment or load mitigation. The main control mechanisms currently used or investigated by the industry or research institutes are:

- Collective Pitch: the blades are pitched equally.
- Advanced Pitch Control:
  - Cyclic Pitch: the blades are pitched equally but with a phase shift between them.
  - Individual Pitch of the blades (IPC).
- Distributed blade control (Smart Rotors).

Conventional pitch regulated rotors, reduce the inflow angle as the wind speed increases which leads to a decrease in the Angle of Attack (AOA) and the forces. Nonetheless, Wingerden [30] argues that turbines with collective pitch control are incapable of reacting to turbulence and can only handle relatively small wind changes. This is due to the different azimuth position of each blade at any moment in time, which means that each blade is under different loading conditions mainly because of wind shear. This effect becomes even greater at larger rotors. A more advanced control method involves the individual pitch of blades depending on their azimuth position. IPC method can be used for load reduction; however, this comes with an increased demand on the pitch system and it also affects the forces on the full blade and not locally. Furthermore, the pitch system is subject to heavy wear and prone to failure, with a significant maintenance cost.

In contrast with those techniques, smart rotors use a different technology which has long been used in airplanes. The blade's loads are controlled by modifying the blade's geometry locally which provides faster control than traditional pitching and lighter/smaller control units and actuation mechanism. Also, the control devices along the blade can be controlled actively and independently. In the following sections a part of the current knowledge on smart rotors and their load mitigation capabilities will be presented.

2.1 Smart Rotors

A smart wind turbine rotor consists of sensors, control units and actuators. Depending on a data set (e.g. wind speed, wind direction, loads, stresses), the sensors provide a response that is analyzed by microprocessors and used as an input to a control algorithm. The controller decides what actions the actuators have to take in order to alter the control unit's position which subsequently modifies the aerodynamic loads on the blade. Numerous smart rotor mechanisms have been considered and examined during the past decade, some of which are:

1. Trailing edge flaps
2. Deformable trailing edge geometry
3. Microtabs
4. Active twist
5. Camber control
6. Suction/blowing
7. Plasma actuators

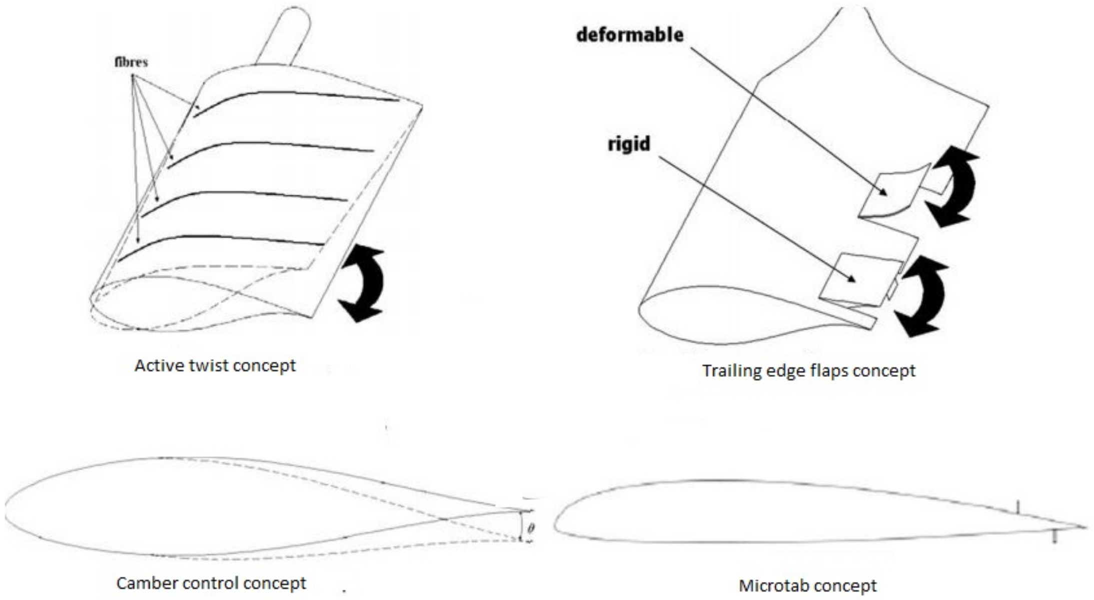

Active twist concept

Trailing edge flaps concept

Camber control concept

Microtab concept

Figure 2.1: Different smart rotor types(Barlas [8])

Since smart rotors are not already established devices on wind turbines, limited feedback has been given upon their performance. Nevertheless, research so far has focused on trailing edge flaps (TRF or flaps) and microtabs. A part of this project concerns the state of the art on past and ongoing research about the potential load reduction resulting from the implementation of TRF. Barlas 2008, highlighted a number of research issues that have to be investigated to make smart rotors an established technology. Some of the most important are:

- The optimum size and position of the control surfaces to have the largest load reduction with the minimum cost.
- The influence on C_l/C_d and power production. The control devices alter significantly the aerodynamic properties of the blade.
- Unsteady aerodynamic effects that might emerge.
- The effect on pitching moment.

Furthermore, smart rotors affect greatly the structural behavior of the blade since they alter simultaneously the shape and the aerodynamic loading on the blade. From a structural perspective the following issues should be investigated.

- The influence of smart rotors on the global stiffness of the blade and on local/global buckling.
- The way bending moments and ultimate stresses are affected.
- The way fatigue loads are affected.
- The risk of a possible actuator failure.

In this research, the influence of TRF on the bending moments, ultimate stresses, buckling and fatigue was examined. As it will be described later in this section, recent experiments have shown that the use of TRF on wind turbine blades can reduce the ultimate and fatigue loads on the blade, which can be translated to a reduce of the mass/cost of the blade. Nevertheless, there are two issues arising concerning the cost effectiveness of this blade. The first issue deals with the manufacturing, installation and maintenance costs of the control devices, sensors and actuators compared to the similar costs of a pitch mechanism. The second issue concerns the mass/cost reduction of the blade (due to lower ultimate and fatigue loads) and whether this decrease can compensate the rest costs.

When a flap is deflected downwards it changes the camber of the blade and increases its lift since it causes a greater curvature of the flow. A wind turbine blade equipped with TRF is graphically presented below.

2.1.1 TRF Positioning and Load Reduction Potential

Recent research has shown that greater load reduction using TRF can be achieved compared to the traditional pitch control methods. In 2004, Troldborg [28] investigated the reduction of fluctuating loads on a Ris-B1-18 wind turbine airfoil using TRF. The shape of the flaps, the flap chord to section ratio, the flap amplitudes, the flap frequency were

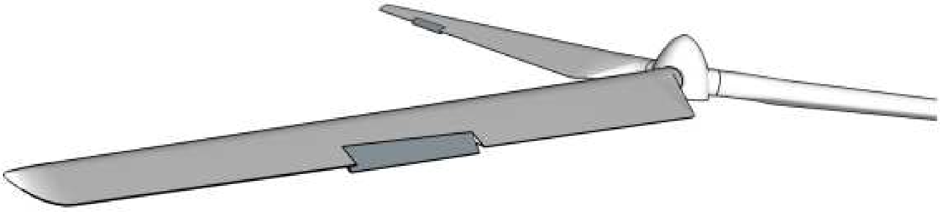

Figure 2.2: Wind turbine blade equipped with TRF (Baek [6])

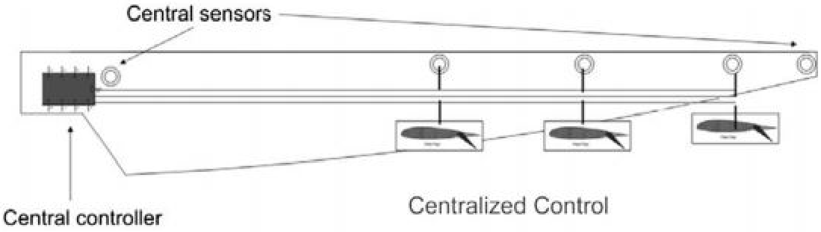

Figure 2.3: Controller, sensor and actuation system of a blade equipped with TRF (Barlas [8])

investigated together with flap oscillations for steady and unsteady flows. The lift force/-drag force /normal force/tangential force/flap hinge coefficients were examined for three flap shapes 1) soft curved, 2) strongly curved and 3) rigid flaps. Furthermore, 4 flap chord to section ratios were examined (0.05, 0.1, 0.15, 0.2), 6 flap angles (-15^0, -10^0, -5^0, 5^0, 10^0, 15^0) and angles of attack ranging from -8^0 to 18^0. The soft curved and strongly curved flaps showed higher lift to drag ratios compared to the rigid flaps.

Buhl et al. [11] studied the loads on blades equipped with deformable TRF on a 33 m blade along with the TRF airfoil aeroelastic response. The flaps were used in order to reduce the fluctuations of the normal forces on the airfoil and fatigue was measured using the theory of equivalent loads. A 3D BEM based aerodynamic model was created together with a 2D model for the trailing edge deformations. Moreover, the aerodynamic model and a spring/damper model were coupled. Several positions of the flaps on the blade were tested in order to find an optimum. Figure 2.4 shows the various flap positions and the corresponding reduction in fatigue of the flapwise root moment.

The experiments showed a maximum of 63% reduction of the blade's flapwise root bending moment for an inflow wind with 10% turbulence and 10 m/s average velocity, using a flap 36% of the blade's span. Moreover, it was found that for a given flap length, higher fatigue reduction can be achieved by dividing the flaps into sections. Furthermore, when the wind velocity experienced a stepwise change from 10 to 12 m/s, the standard deviation of the normal force on the airfoil showed a reduction up to 95% and including turbulence this reduction reached up to 81%. However, when using realistic values for the time lag and the actuation velocities the reduction of the normal forces was between 25% and 38%. This shows the high effect of 1) the time lag in the actuators and sensors and 2) the actuation velocity on the reduction of the normal force.

Bak et al. [7], conducted wind tunnel experiments at a Risoe-B1-18 airfoil equipped with adaptive trailing edge geometry (ATEG). Steady state and dynamic tests were conducted

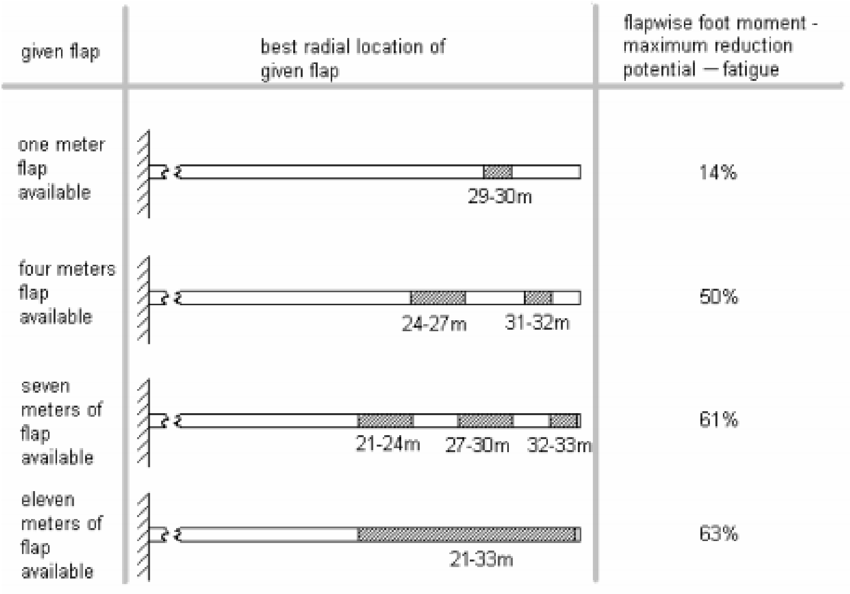

Figure 2.4: Buhl et al. [12] optimum placement of various flap arrangements

for this airfoil using piezoelectric actuators at the trailing edge as ATEG. It was shown that under steady state conditions, the operation of the flaps (towards the pressure or the suction side) changed (increased in one case and reduced in the other) the lift significantly and left the drag uninfluenced. Additionally, a step change and sinusoidal changes of the ATEG were tested to prove the ability of ATEG to cancel load variations at the airfoil (reached up to 80%).

Andersen et al. [4] also investigated how the TRF influence the fatigue loads. First a 6.3m flap was placed at the NREL 5MW reference turbine blade, then two 6,3m flaps (12.6m) and finally three 6,3m flaps (18.9m). Different positions of the sensors and actuators were also examined and flaps had a $\pm 8^0$ deflection range. Furthermore, an optimization engine was used to find the optimum position for one flap on the blade. The optimal position was found at 94% of the blade's span, for a stiff blade and at 71.5% for a soft blade. When using one flap, a fatigue reduction on the flapwise root moment fatigue load of 25% was observed for a soft blade and 17% for a stiff blade. On the other hand, when two and three flaps were used the reduction was 34% and 37% respectively. The reason for this great reduction was because this research used lower turbulence intensity and wind shear compared to the IEC standards.

Lackner et al. [18] investigated the load reduction on a 5MW wind turbine equipped with TRF, using the aeroelastic design code DNV GL Bladed. Moreover, the combination of two methods for reducing the loads was examined in this research. Lackner placed the TRF between 70 and 90% of the blade span with a 10% chordwise length and a $\pm 10^0$ deflection range. This deflection range led to a significant lift change while the drag coefficient showed small variations. Furthermore, the fatigue loads were reduced by 12-15% under rated operation and normal turbulence. Lackner argues that a hybrid system that combines IPC with TRF could be able to reduce aerodynamic loads even by 20%.

Markou et al. [19] arrived at the conclusion that TRF can reduce more the loads of wind turbines in wakes compared to individual pitch control. In this research controllers for two different scenarios were designed, one of a wind turbine that had individual pitch control and one equipped with TRF. The inputs used were the blade flap root moments and the local inflow angle measurements in order to get as an output the fatigue loads. Load reductions up to 73% for a blade equipped with TRF were observed on the meandering wakes that appear in wind farms. Also, the TRF that showed the highest deflections had a better performance. However, if non-ideal flaps were used the expected fatigue load reduction would be 20 to 30%.

Baek [6] investigated from an aerodynamic and aeroelastic perspective three active aerodynamic devices: 1) a microtab with a length 1% of the chord, 2) a miniflap with a length 1% of the chord and 3) a TRF with a length 10% of the chord and a $\pm 10^0$ deflection on 20% of the chord. The software FLEX5 was used for simulations on the Upwind 5MW reference turbine. The miniflap and the TRF were tested in the wind tunnel of LM Wind Power. Baek took into consideration also the extreme loads besides the fatigue loads. Also, he investigated the change that the TRF cause to the tower bottom, the tower top, the shaft torsion and the hub moment. A load reduction of 16% was found using TRF and 22% using individual pitch. If both techniques were used then a reduction of 26% would be possible on flapwise fatigue loads. Baek also reports that if the fatigue loads are decreased by 25% then the blade weight can be reduced by 7%, however this would lead to higher tip deflections. Furthermore, the edgewise load does not influence the loads significantly. More precisely, a decrease of 10% of the edgewise loading would lead to less than 1% decrease of the blade weight. Moreover, a decrease on the loads at the hub and the tower top were observed. Baek worked on rated wind speed and concluded that the load reduction potential at the blade root in power production and start-up is rather low; however this is not true for other components of the turbine.

Bergami [9] developed an aerodynamic model (based on the BEM-based aerolastic simulation code HAWC2) for a 2D airfoil equipped with flaps. Furthermore, the results of this model were compared with CFD simulations and a panel code method. This model took into account attached and separated flow conditions. Using this model on the NREL 5 MW wind turbine he found that at normal operation above the rated wind speed, loads that have frequencies below 1Hz contribute at most on the blades flapwise fatigue. Regarding the position of the flaps, Bergami placed them at 77% to 97% of the blade length and at the outer 20% of the blade span. Moreover, the alleviation of loads should focus on wind speeds above rated because at these velocities the fatigue loads are larger. Bergami found a reduction of 15% on the blade root flapwise fatigue damage equivalent load during its lifetime. He also states in his research that if the TRF control method was combined with an individual pitch method, this reduction might reach 30%. Furthermore, the load alleviation might lead to an increase in annual energy production. More precisely, the results of Bergami combined with the research of Baek [6] show a possible increase in the annual energy production from 1.5% to 14%.

Bernhammer et al. [10] investigated the reduction of the vibration level on the specific parts of a wind turbine equipped with TRF. This research basically includes a fatigue load and an extreme load analysis taking into account a number of load cases. The NREL 5MW turbine was simulated using DU-SWAT software and simulations were run with and without an individual flap control. This research was an extension of that made by Baek [6]. A 34% fatigue load reduction for the out-of-plane blade root moment was found and

7% for the in-plane; however, a 27% increase of the torsional moment was also observed. The impact of TRF on the shaft and nacelle moments and forces together with the tower's top and root moments and forces were also investigated. Furthermore, the impact of TRF on extreme turbulence during power production, extreme operational gusts and extreme change of direction for various wind bins was analyzed. It was found that the nacelle for aft moments, tower torsion, root bending moments and maximum tip displacements were reduced significantly.

Barlas et al., 2011, used flaps on 18% of the blade span with 10%c with a ±8 deflection and found a 14% reduction in the root bending moment fatigue load. However, Barlas stated that a flexible flap with a strong curvature controls more effectively the aerodynamic loads. Also, a flap with that has a length 5% of the chord and a $\pm 10^0$ deflection can control most of the wind variations. However, a flap with a length 10% of the chord and a $\pm 5^0$ deflection is preferred due to its ability to better increase the lift with no significant increase of the drag.

The most important findings of this section are presented in table 2.1 and 2.2. Table 2.1 summarizes the size and position of the flaps on the blade that the researchers have decided in their projects.

Researchers	Length (of the blade span)	Chordwise Length	Position at the blade span	Pitch
Wingerden	10.5 cm	50%	-	2 °
Barlas	18%	10%	-	8 °
Andersen	20%	20%	71-94%	-
Bergami	20%	20%	77-97%	-
Buhl	21% each flap	10%	Various arrangements	4 °
Lackner	-	10%	70-90%	10 °
Baek	20 %	10%	-	10 °

Table 2.1: Various flap arrangements that have been tested

Researcher	Finding 1	Finding 2	Finding 3
Bernhammer	A 34% fatigue load reduction for the out-of-plane blade root moment and 7% for the in-plane	A 27% increase of the torsional moment	The nacelle for aft moments, tower torsion, root bending moments and maximum tip displacements were reduced significantly
Buhl	63% reduction of the blades flapwise root bending moment for inflow with 10% turbulence and 10 m/s average wind speed, using a flap 36%	There is a high effect of the time lag in the actuators and sensors and the actuation velocity on the reduction of the normal force	By dividing the flaps into sections higher fatigue reduction was achieved
Bak	under steady state conditions, the move of the flaps changed the lift significantly but left the drag uninfluenced	ATEG have the ability to cancel the load variations at the airfoil even up to 80% at its optimal use	-
Andersen	using one flap, a fatigue reduction on the flapwise root moment of 25% is observed for a soft blade and 17% for a stiff one	when two and three flaps were used, the reduction was 34% and 37% respectively	
Lackner	Fatigue loads reduced 12-15% under rated operation and normal turbulence	A Hybrid system with flaps and IPC could reduce the loads by 20%	-
Bergami	At normal operation above rated wind speed, loads with frequencies below 1Hz contribute most on flapwise fatigue	Reduction of 15% on the blade root flapwise fatigue damage equivalent load during its lifetime	If the TRF was combined with IPC, reduction might reach 30%
Markou	TRF can reduce more the loads of wind turbines in wakes compared to IPC	Load recuctions up to 73% were observed for a blade with ideal TRF. If non-ideal flaps were used the reduction would be 20-30%	
Baek	Load reduction of 16% using TRF and 22% using IPC. Turbulence intensity has a significant role in the flap load reduction performance	When using IPC and TRF combined a reduction 26% of flapwise fatigue loads is achieved. Using TRF the rotor radius could be increased by 2-3% and the energy yield by 1-2% . If the fatigue load is reduced by 25%, the blade weight can be reduced by 7%	A decrease of 10% of the edgewise loading would lead to a decrease less than 1% of the blade weight.

Table 2.2: Significant findings on smart rotor load alleviation

2.2 Structural Design

During the blade design process, numerous parameters are taken into consideration. The final blade geometry design is accomplished through an iteration process after considering the energy extraction, loads, structural design, and manufacturing costs. Structural design deals with the selection of materials, their thickness and orientation. Additionally, it interconnects the disciplines of design and manufacture in order to create a solution which is optimum in terms of performance and cost. The design process requires analysis on the critical components to ensure their performance. This analysis consists of the following parameters:

1. The blade must be stiff enough in order to avoid hitting the tower when deflected by high flapwise moments.
2. Local stiffness must be sufficient in order to ensure that local and global buckling is avoided when the blade is under compression.
3. Resonance must be avoided.
4. The blade must be able to withstand the various extreme loadings (extreme wind, turbulence, emergency braking).
5. The blade should be able to resist time varying loads (wind variation, wind shear, blade rotation) through its lifetime. In other words the blade should have a high fatigue life.
6. The weight of the blade should be minimum.
7. The material cost must be as low as possible.
8. The blade must be manufacturable.

So, the structural integrity can be measured by a number of criteria. These criteria are mentioned below and will be analyzed in more detail in chapter 4.

- Ultimate strength
- Fatigue strength
- Local buckling
- Global buckling
- Resonance (Campbell diagram)
- Tip deflection

This means that the materials should have high strength, high fatigue strength, high stiffness and low density. The aforementioned properties are found at composite materials which will be described in the following section.

2.3 Materials

The behavior of the blade under specific loading depends on the structure's geometry and materials. One of the most important challenges in wind energy is to develop new materials in order to make the blade lighter and larger in order to produce more power, and at the same time assure that it can withstand the various loads. Research has focused on composite materials due to their low weight and good structural performance. Composite materials consist of different material layers, each of which constitutes of: 1) fibers in various orientations which add strength and stiffness, 2) the matrix which holds the fibers together and distributes the load. The properties of a composite material are determined by the properties of the fiber material and the matrix material, the fiber volume fraction and the orientation of the fibers. In wind industry Glass-Fiber Reinforced Plastics (GFRP) and Carbon-Fiber Reinforced Plastics (CFRP) are widely used mainly due to their high strength-high stiffness and low weight.

A typical wind turbine blade has the form shown in figures 2.6 and 2.5. The cross section can be divided into the spar caps, shells, shear webs and leading/trailing edge. The spar caps are the main carriers of bending loads;however, the shells also have a contribution to bending strength. The spar caps are usually placed at the maximum distance between them and they are connected through a shear web. The shear web-spar cap structure is usually in the form of an I-Beam or a box.

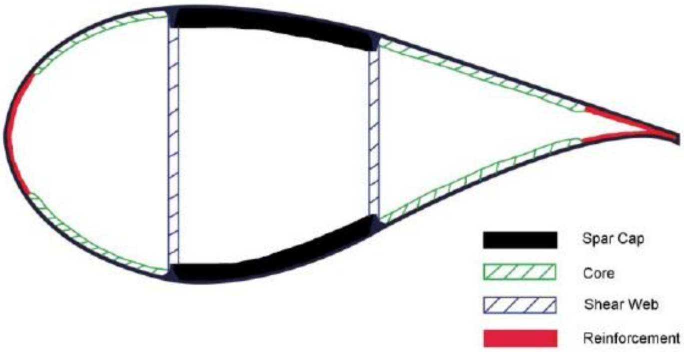

Figure 2.5: Representative blade cross section (Sandia 100m [15])

The materials of the various sections of a representative blade as shown in 2.5, differ greatly between them and along the span. There is a great number of failure criteria and loading conditions on the blade which make the design of the materials highly complex. For each loading condition and at each location on the blade a different failure criteria becomes dominant and other criteria become less important. Thus, every part has a specific 'role' (e.g. adds flapwise/edgewise stiffness, adds strength for buckling etc) in order to create a blade that can endure all the possible loading scenarios at minimum cost.

Shells are usually composed of a thin skin material and a thick core material that increases the shell's stiffness. The shell should be stiff enough in order to prevent bending and local buckling. Furthermore, shells often include diagonal fibers to account for torsional stiffness and also have fibers along the blade's span to provide stiffness for edgewise bending and assist the spar caps in flapwise bending. Additionally, it is common to reinforce the trailing edges of the blade close to the root in order to support shells in edgewise bending. Regarding spar caps, a great amount of the fibers are unidirectional and oriented along the blade to carry the bending forces. On the other hand, shear webs usually contain fibers in diagonal direction in order to provide shear stiffness.

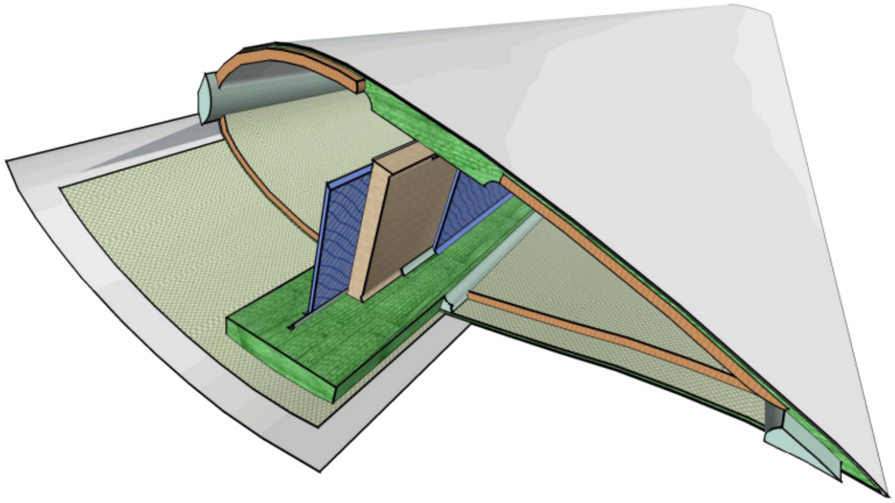

Figure 2.6: 3-D blade cross section cut (Lectures of Design and Manufacturing of Wind Turbine Blades [3])

2.4 SANDIA 5MW HAWT Blade

The Sandia National Laboratories, managed and operated by the Sandia Corporation, are major United States energy research and development national laboratories. Research performed on Sandia laboratories is mainly focused on the non-nuclear components of nuclear weapons, however it also includes a wide variety of topics related to renewable energy, materials science, computational biology, mathematics, psychology etc. A part of this research was the 5MW, 61.5MW wind turbine blade that was developed [23], mainly based on the NREL offshore 5MW HAWT baseline wind turbine [16].

The purpose of this project was to structurally design a HAWT blade that meets the IEC design criteria and could be used as a base for detailed design such as blade optimization. The NREL 5MW wind turbine blade did not contain a detailed material design and its structural properties were only descibed by the distributed stiffnesses and moments of inertia. Therefore Sandia created a more detailed design of the laminae layup that was based on the UpWind program [29] and the Sandia 100-m project [15]. Also, the geometry of the blade used the existing data from the DOWEC study [17] (which are the same with the NREL). The first goal of this project was to match the mass and spanwise distibuted properties with the NREL project. Then, FEM analysis was performed for a number of load cases based on the IEC standards in order to match the IEC criteria. As stated by Sandia, the blade designed can be very useful as a starting point for other researches on blade design optimization, blade design tool verification, material/structural study and standards evaluation. In the context of this thesis, the Sandia blade design was used for the verification of the design tool and also for blade optimization.

2.5 Multidisciplinary Optimization

These concepts are usually multidisciplinary and interactive between the different disciplines. All the different designs in the multidisciplinary optimization have scores that are evaluated through a function. The aim is to minimize/maximize this function in order to find the optimum solution to the problem. The solution of a multidisciplinary optimization is more accurate than the one obtained by optimizing each discipline sequentially since it also exploits the interactions between the disciplines, however at the cost of increasing the problem's complexity. Such optimization normally contains:

- **Design Variables:** independent variables of the function.
- **Constraints, Boundaries:** conditions that must be satisfied.
- **Objective function:** a function that has to be maximized or minimized.

In order to make the concept of multidisciplinary optimization more clear, a simplistic approach of the optimization that was conducted as part of this project is presented. The goal is to minimize the weight of a HAWT blade and subsequently minimize its cost. Nonetheless, there is great number of disciplines interconnected to each other (structural, aerodynamic, electrical etc.) and all those disciplines contain a vast number of sub principles. Nevertheless, the larger the number of attributes included in the optimization, the higher the problem's complexity and simulation time. Therefore, the optimization strategy focuses on structural optimization by altering the various thicknesses on the blade. This means that 1) the cost/mass of the blade is the objective function, 2) the thicknesses are the design variables, 3) the physical/structural limits on the thicknesses are the boundaries and 4) the structural behavior of the blade under specific loading conditions (ultimate stress, deflection, buckling fatigue etc) are the constraints that have to be satisfied.

Chapter 3

Development of the Blade and Loads

As presented in figure 1.1, the design and optimization process of the HAWT blade is divided into 5 main steps. The first two steps involve the creation of the input file (.bdf) for MSC Nastran. After that, the FEM analysis is executed, the FEM output file (.f06) is post processed and finally the blade's weight is minimized. Regarding the creation of the FEM input file, this process can be divided into the following three sub-processes.

- **Geometry design** - Configuration of the blade's geometry (twist, chord, airfoils, etc).
- **Material design** - Configuration of materials (plies, stacks and stack assignment at the respective sections)
- **Loads** - Configuration of operational conditions and loading on the blade.

The methodology and the reasoning behind these sub-processes will be analyzed thoroughly in the following sections.

3.1 Geometry

In FEM analysis, the blade has to be divided into numerous elements each of which constitutes of a number of nodes. A series of steps are required in order to design the blade's geometry and translate it into nodes and elements. The first part of the methodology that was followed includes the creation of points (control points) that describe the beam axis. The chord length and twist angle of the blade are indicated at each control point. The control point coordinates and the chord length should be normalized by the blade radius because the blade length might alter during the optimization, so these values will have to also change proportionally. The next step is to divide the blade into a number of spanwise sections, each of which has an assigned airfoil. Using a Non-uniform rational basis spline (NURBS) algorithm, a smooth transition of the shape from one section to the next is achieved by taking into account the various airfoils and the chord/twist distribution.

NURBS is a mathematical model used in order to represent curves and surfaces. It is widely used in computer-aided design (CAD), manufacturing (CAM) and many more applications. NURBS generally offer great flexibility in shape modelling. Ferede et al. [14] created a tool (MATLAB code) based on NURBS used for the modelling of wind turbine blades. This tool creates a parametric design of a wind turbine blade, while the user is capable of varying the blade's shape and properties. Blades with generic complex shapes (like sweep, curvature) can be designed and their shape can be optimized. The blade is parametrized in terms of its beam axis, twist angle and weighted airfoil shape at a control point. There is a number of position vectors that define the beam axis which is the one that controls the geometrical shape (sweep, curvature). Weighted airfoils are used, which are airfoil shapes multiplied by the chord at a control point.

The tool developed by Ferede [14], Schelbergen [25] and Roscher [24] has been modified in order to apply on a HAWT; however, three important additions have also been made. First, the blade can have more than one airfoil along the span, making it possible to create a more accurate aerodynamic design. Second, each spanwise section can have a different length and a different number of elements. Third, the user can decide the number of parts (panels,spar caps, trailing edge, leading edge etc.) in the chordwise direction and the number of panels assigned to each part. The reason behind these changes is because the difference in the airfoil shape and the chord length along the span creates a mesh with a varying element aspect ratio (x/y side), so a different number of elements per section leads to better defined mesh (homogeneous aspect ratio).

More precisely, in the spanwise direction, the blade is divided into a number of equal sections with a different mesh density. The mesh density vector has the same length as the number of sections. Each value of this vector reflects the normalized number of elements by the number of elements that section would have if all sections had the same number of elements.

Regarding the chordwise direction, the user must specify the number of sections. After that, there are two ways to define the panel density. In the first method, the number of chordwise panels has to be defined along with the length of each chordwise section by specifying its chord percentage. In the second method the number of panels and their sequence must be input. The following example of the two methods about an airfoil with divided into 11 sections is presented (5 in the lower side, 5 in the upper side and 1 the shear webs).

- method 1: [0 x_1 x_2 x_3 x_4 1]*n for the lower part of the airfoil and x_5*n for the shear web. The lower part is divided into 5 sections (0-x_1,...,x_4-1) and the number of panels (n) is divided according to the rounded percentage value of each section. The upper side of the airfoil is divided in an identical way. The total number of panels is 2*n+round(x_5*n).

- method 2: [p_1 p_2 p_3 p_4 p_5] for the lower part of the airfoil and p_6 for the shear web. The user specifies the number of panels of each chordwise member.

In the research of Schelbergen[25] the mass was computed by a summation of each section, considering a constant shell thickness along the blade. Nonetheless, in reality the thickness should depend on the specific local curvature and loading such that each blade's section can vary. For this reason, Roscher [24] tested various interpolation techniques for the mass and thickness on the tool created by Schelbergen. It was shown that the cubic spline interpolation provided more accurate results compared to the linear and weighted polynomial interpolations. The cubic spline interpolation requires a number of points that the curve passes through. These points are the root, the tip and the middle of each intermediate section. The number of spanwise sections requires attention because a small number means also a small number of cubic spline interpolation points which might lead the interpolation results to decline greatly from the initial mass.

Summarizing, the geometry sub-section of the Matlab tool developed requires the set of inputs presented below and delivers the grid coordinates that describe the blade's geometry. The flowchart of figure 3.1 shows the main reasoning of the geometry analysis process.

- Set the coordinates of the control points.
- Define the airfoils used along the span of the blade (x-y coordinates).
- Define the chord and twist distribution along the span of the blade.
- Set NURBS parameters (degree of polynomial, inter element continuity etc.). As stated by Ferede [14] the optimum continuity factor (k) is equal to k = p1.
- Set the chordwise location of the spar as a percentage of the chord length.
- Define the number of spanwise and chordwise elements along the span.

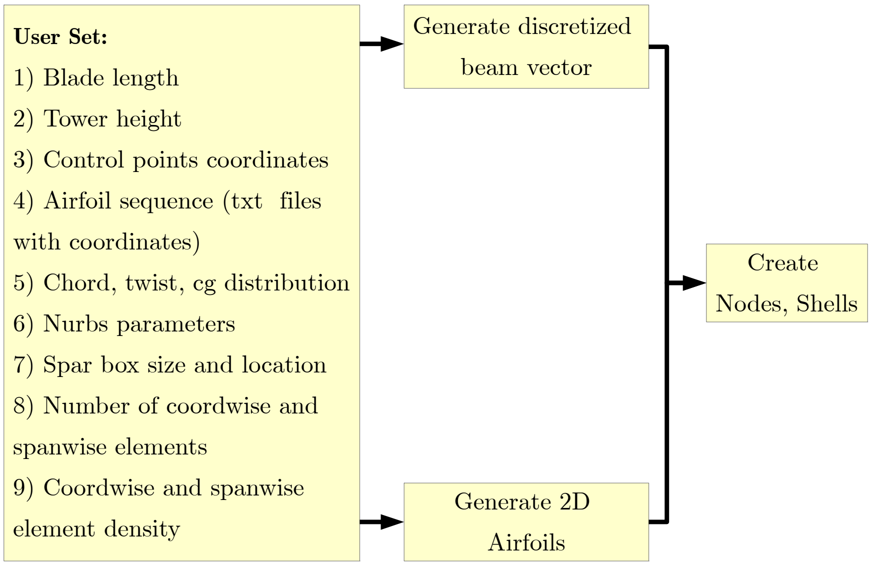

Figure 3.1: Geometry generation flow chart

3.2 Materials

Similar to the geometry part of the tool, the material part is a modified version of the algorithm designed by Schelbergen [25]; however, with also some very important additions. The most significant modification of the tool is to provide the ability for creating different stacks for each chordwise section and along the span. The main reasoning behind the stack creation and calculation of the structural properties of each stack (stiffness matrix, allowable stresses) is presented at the flowchart of figure 3.2.

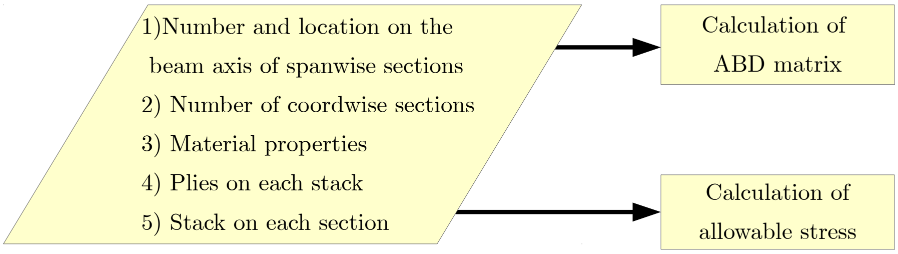

Figure 3.2: Material Flow Chart

In detail, first the number of sections that the blade is divided along the span is specified together with the starting and ending point of each section. Each spanwise section is constituted of the same stacks but with a varying thickness. An algorithm created by Roscher [24] is used in order to interpolate with cubic splines the thickness along each section in order to achieve a smooth thickness transition.

After that, a list of materials (plies) with their following properties have to be specified:

- Stiffness in x,y,xy direction (Pa).
- Poisson ratio.
- Density (kg/m^3).
- Tensile strength in x,y direction (Pa).
- Ply thickness.

Each stack is created by specifying the sequence of the identification numbers of the appropriate materials. Additionally, a parameter that shows which stack is a sandwich material is used. If the value assigned is 0, then the stack is not a sandwich structure. In case of a sandwich structure, the value assigned shall be equal to the stack's sandwich core material thickness.

Finally, the identification number of each stack on the corresponding chordwise and spanwise section has to be specified. Once all inputs are set, the algorithm then calculates the stiffness (ABD) matrix of each stack and the tensile/compressive allowable stresses in the x,y directions. The procedure can be better understood in chapter 5 where the inputs of the initial blade design are presented.

3.2.1 Stiffness Matrix

In order to conduct the FEM analysis, the stiffness matrix (stress-strain relation) of each element has to be input in the FEM solver. Classical lamination theory (CLT) is used in order to calculate the stiffness matrix (ABD) of each stack. CLT theory is very similar to the classical plate theory for isotropic materials, with the main difference that it applies to orthotropic continuous fiber reinforced composite laminates which have more complicated stress-strain relations. The purpose of CLT is to develop the relations between external loading (transverse and in-plane loading) and displacements by satisfying the conditions of static equilibrium.

In order to calculate the stiffness matrix of each stack, the first step is to calculate the stiffness matrix for each ply of the stack from relations 3.1 and 3.2. The properties Ex, Ey Vxy, Gxy of each ply have to be known. The methodology for calculations can be found in Phillipides [22].

$$Q_s = \begin{bmatrix} \frac{E_{XX}}{1-V_{XY}*V_{YX}} & \frac{E_{YY}*V_{XY}}{1-V_{XY}*V_{YX}} & 0 \\ \frac{E_{YY}*V_{XY}}{1-V_{XY}*V_{YX}} & \frac{E_{XX}}{1-V_{XY}*V_{YX}} & 0 \\ 0 & 0 & G_{XY} \end{bmatrix} \tag{3.1}$$

where:

$$V_{YX} = \frac{E_{YY}}{E_{XX} * V_{XY}} \tag{3.2}$$

The stiffness matrix of the ply is transformed from its principal axis to the stack's global coordinate system by substituting the transformation matrices 3.3, 3.4 to relation 3.6.

$$T_1 = \begin{bmatrix} m^2 & n^2 & 2mn \\ n^2 & m^2 & -2mn \\ -mn & mn & m^2 - n^2 \end{bmatrix} \tag{3.3}$$

$$T_2 = \begin{bmatrix} m^2 & n^2 & mn \\ n^2 & m^2 & -mn \\ -2mn & 2mn & m^2 - n^2 \end{bmatrix} \tag{3.4}$$

where:

$$m = \cos\theta, \tag{3.5a}$$

$$n = \sin\theta \tag{3.5b}$$

$$Q = (T_1)' * Q_s * T_2 \tag{3.6}$$

The ABD matrix is calculated by adding the contribution of each ply using the three relations in 3.7, where z is the distance of each ply from the middle of the stack, n is the number of layers and w is the layer number. Coordinates x and y are in the in plane directions of the plate, and z is assumed positive downwards.

$$A = \sum_{w=1}^{n} Q(k)(z(w+1) - z(w)), \tag{3.7a}$$

$$B = \sum_{w=1}^{n} \frac{Q(k)(z(w+1)^2 - z(w)^2)}{2}, \tag{3.7b}$$

$$D = \sum_{w=1}^{n} \frac{Q(k)(z(w+1)^3 - z(w)^3)}{3} \tag{3.7c}$$

So, the resulting stiffness matrix that connects the forces (N) and moments (M) to the strains (ϵ) and curvatures (k) is shown in relation 3.8, where A is called the extensional stiffness, B is called the coupling stiffness, and D is called the bending stiffness of the laminate.

$$\left\{ \begin{array}{c} N_x \\ N_y \\ N_{xy} \\ M_x \\ M_y \\ M_{xy} \end{array} \right\} = \left\{ \begin{array}{cc} A & B \\ B & D \end{array} \right\} \left\{ \begin{array}{c} \varepsilon_x \\ \varepsilon_y \\ \varepsilon_{xy} \\ \kappa_x \\ \kappa_y \\ 2\kappa_{xy} \end{array} \right\} \tag{3.8}$$

As mentioned previously, in the wind turbine blade industry sandwich composite structures for the shell panels and the shear webs are often used. Usually sandwich composites are composed of two identical stiff panels, separated by a light core material (e.g. foam). By adding a core material, the thickness of the stack is increased together with its stiffness, without a significant increase of the weight. The skin panels carry the tensile and compressive loads while the core carries the shear loads. Furthermore, the panel foam greatly affects local buckling since it increases the stiffness of the stack. Similarly the thickness of the inboard shear web foam influences shear web buckling.

If a stack is a sandwich structure, then the user shall specify the materials of one of the two identical panels, the core material properties and the core material thickness. Afterwards, the ABD matrix of the panel is calculated following the methodology described. Using relations 3.9 the ABD matrix of the total stack is calculated.

$$A = 2A_f \tag{3.9a}$$

$$D = 2D_f + \frac{1}{2}(h_f + h_c)^2 A_f \tag{3.9b}$$

where:

- A_f: the A matrix of the panel.
- D_f: the D matrix of the panel
- h_f: the thickness of the panel.
- h_c: the thickness of the core material.

The procedure of creating the ABD matrix is summarized in the flowchart presented in figure 3.3.

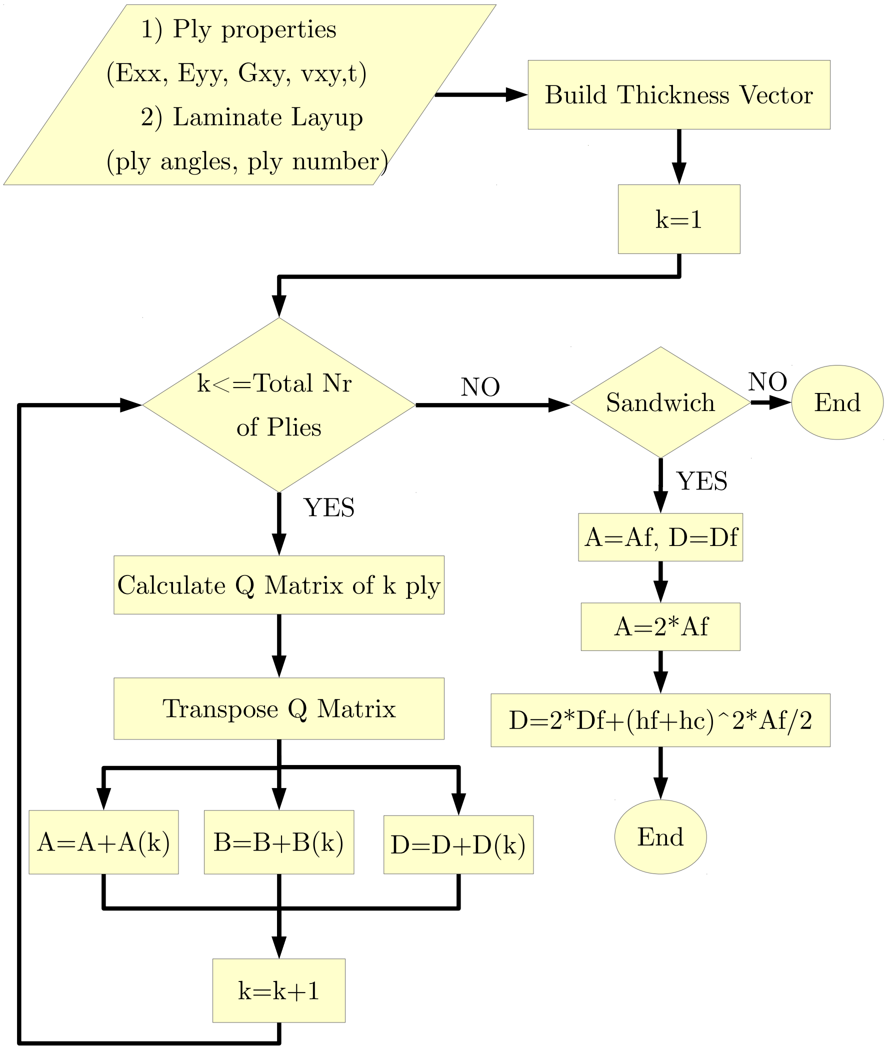

Figure 3.3: ABD matrix creation flowchart

3.2.2 Allowable Stresses

The stiffness matrix is used for the FEM analysis; however, in order to evaluate the results of the FEM solver, the ultimate/allowable stresses of each stack are needed. On each optimization iteration, the FEM solver outputs the stresses on each element and those stresses are compared with the allowable stresses of the corresponding stack in order to examine the occurrence of failure. The Tsai-Hill failure criterion presented in equation 3.10 is used to evaluate the ultimate stress at each direction (X,Y) and under compression (c),tension (t), shear (S) for each stack. The calculation procedure of the allowable stresses is presented in the algorithm of figure 3.4.

$$\frac{\sigma_\chi^2}{\mathrm{X}^2} - \frac{\sigma_\chi \sigma_y}{\mathrm{X}^2} + \frac{\sigma_y^2}{Y^2} + \frac{\tau_{\chi y}^2}{S^2} = 1 \tag{3.10}$$

3.3 Loads

Once the elements are created and the materials are assigned to them, the final part of the FEM input algorithm deals with the forces that act on the blade. The number of forces exerted on wind turbine blade's is rather large; however, they can be divided into the following main categories (Wind Energy Handbook [13]):

- Gravitational loads
- Inertial loads (centrifugal loads)
- Aerodynamic loads
- Operational loads (due to braking, yawing, pitching etc.)

The tool created does not take into account any operational loads. Also, the analysis is static and conducted on a number of azimuth positions, which means that no fluctuation of the wind speed can be included along with other dynamic phenomena such as wake effects. Furthermore, the tool is capable of analyzing one load case only per run. Regarding the gravitational load, the thickness and density are calculated for each stack and used as an input in MSC Nastran. The mass of each element is then calculated in MSC Nastran using the area of each element. The centrifugal forces that act due to rotation are also calculated internally in MSC Nastran.

3.3.1 Aerodynamic Loads

The aerodynamic loads depend on the environmental conditions and the blade's geometry which was created in previous steps. The FEM solver requires a pressure force applied on each node. These pressure forces are created after a series of steps that will be described in this section. For the calculations at this part of the tool, blade element momentum (BEM) theory is used. The wind velocity v_{inf}, rotational velocity v_{rot} and the resultant velocity v_r can be seen in figures 3.5 and 3.6 from Wind Energy Handbook [13].

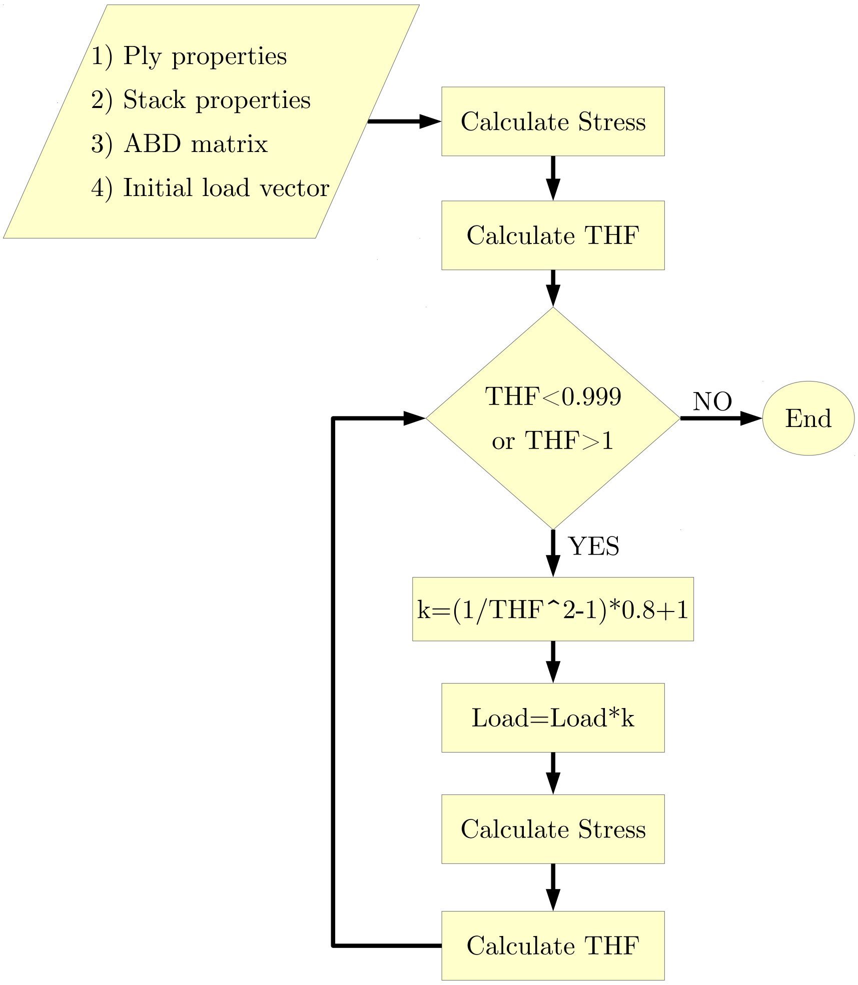

Figure 3.4: Allowable stress calculation flowchart

The tool developed is a modified version of that developed by Schelbergen [25] with some significant additions. First of all, the user has the option to divide the blade into any number of aerodynamic sections, each of which will have a different a chordwise pressure coefficient distribution. Second, the wind shear log/log law (equation 3.11) is used and the wind speed v_{inf} at each spanwise position (h) is calculated depending on the azimuth position, the relative roughness z_0 and the reference height h_{ref}.

$$v_{inf}(h) = v_{inf}(h_{ref}) \frac{ln(\frac{h}{z_0})}{ln(\frac{h_{ref}}{z_0})} \tag{3.11}$$

Third, in order to account for the conservation of momentum, an induction factor is also

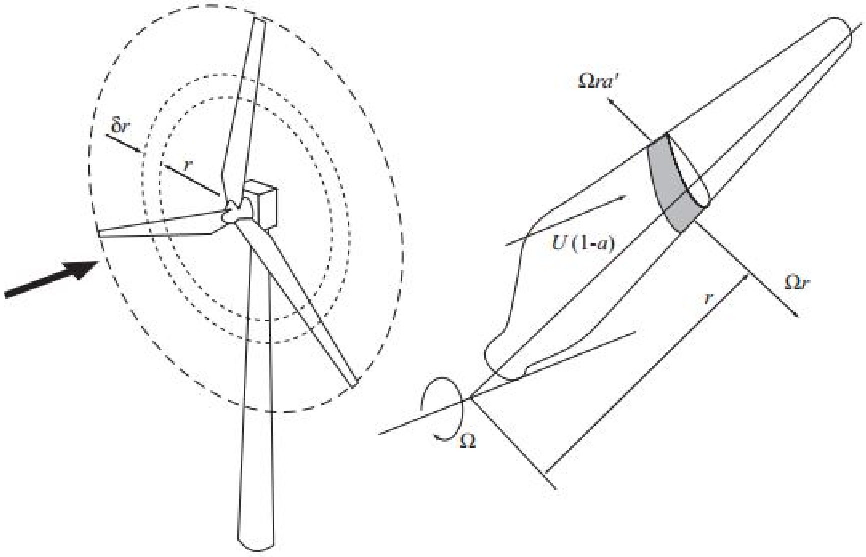

Figure 3.5: 3D HAWT velocities

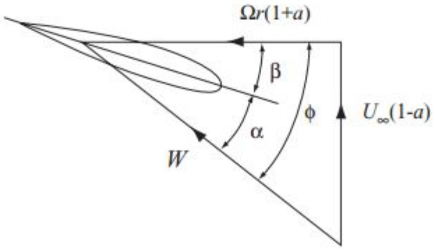

Figure 3.6: 2D HAWT velocities

included by the user. The resultant velocity at each spanwise position comes from the combination of the wind velocity vector and the rotational velocity vector (taking into account also a spanwise varying rotational induction factor). Fourth, the inflow angle ϕ (the angle between v_r and v_{rot}) is calculated for each spanwise position. The angle ϕ is equal to the sum of the angle of attack (AOA), the pitch and the twist angle, so since all variables are known for each spanwise position, then the AOA can be directly calculated. Fifth, the Reynolds number is calculated using equation 3.12.

$$Re = \frac{\rho d v_{rot}}{\mu} \tag{3.12}$$

where:

- ρ: air's density
- d: width of the airfoil at each position
- μ: air's dynamic viscosity

Afterwards, the dynamic pressure (p) is calculated using equation 3.13.

$$p = \frac{1}{2}\rho C_p {v_r}^2 \tag{3.13}$$

Another important addition is the application of Prandtl's factor for the tip losses shown in equation 3.14. At each spanwise position (r), the dynamic pressure is multiplied with the corresponding Prandtl factor.

$$f = \frac{2}{\pi}\cos^{-1}\left\{\exp\frac{-(\frac{B}{2})[1-(\frac{r}{R})]}{(\frac{r}{R})\sin\varphi}\right\} \tag{3.14}$$

Since the AOA and Re number are known at each spanwise and azimuth position, using the software XFOIL the chordwise pressure coefficient distribution for each spanwise aerodynamic section is calculated. A typical pressure distribution has the form of that presented in figure 3.7. The pressure coefficients are post processed in Matlab in order to apply one vector on each node.

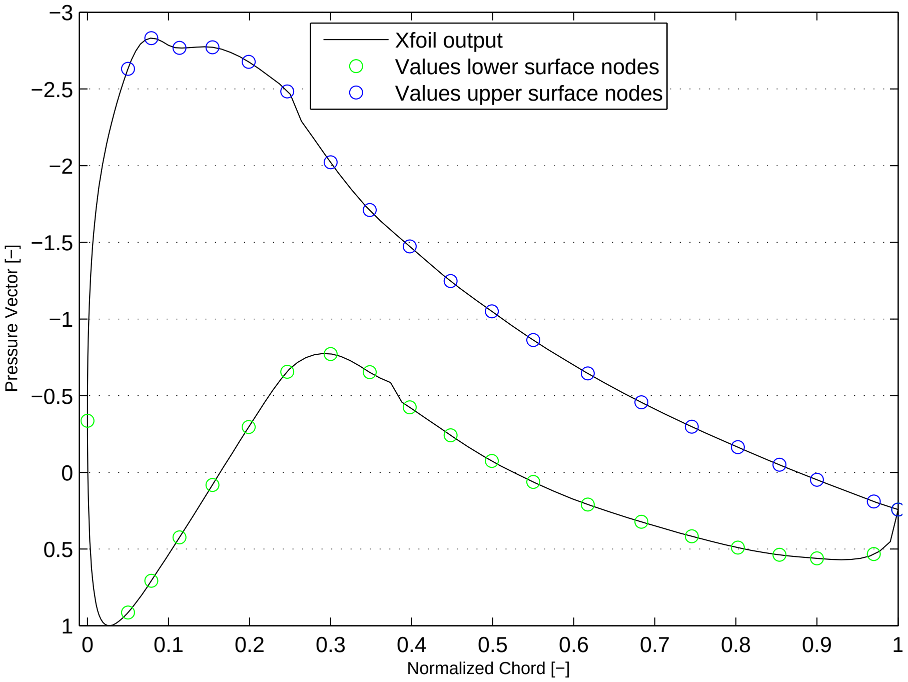

Figure 3.7: Cp versus normalized chord for DU99-W-405 airfoil

Finally, the pressure on each node can then be calculated by multiplying the pressure coefficient on that node with the corresponding dynamic pressure of that spanwise location.

In order to perform the FEM analysis, the following input parameters have to be defined by the user. In figure 3.8 the main reasoning of the load creation part of the tool is presented.

- Tip speed ratio (-).

- Wind velocity at hub height (m/s).
- Azimuth positions (deg).
- Log wind shear law roughness.
- Axial induction factor.
- Pitch angle (the twist angles are already known from the geometry design).
- Air properties (density, dynamic viscosity).
- Location of each section (as a percentage of the blade span) with different pressure Cp-x distribution.
- Cpx files for each aerodynamic section.

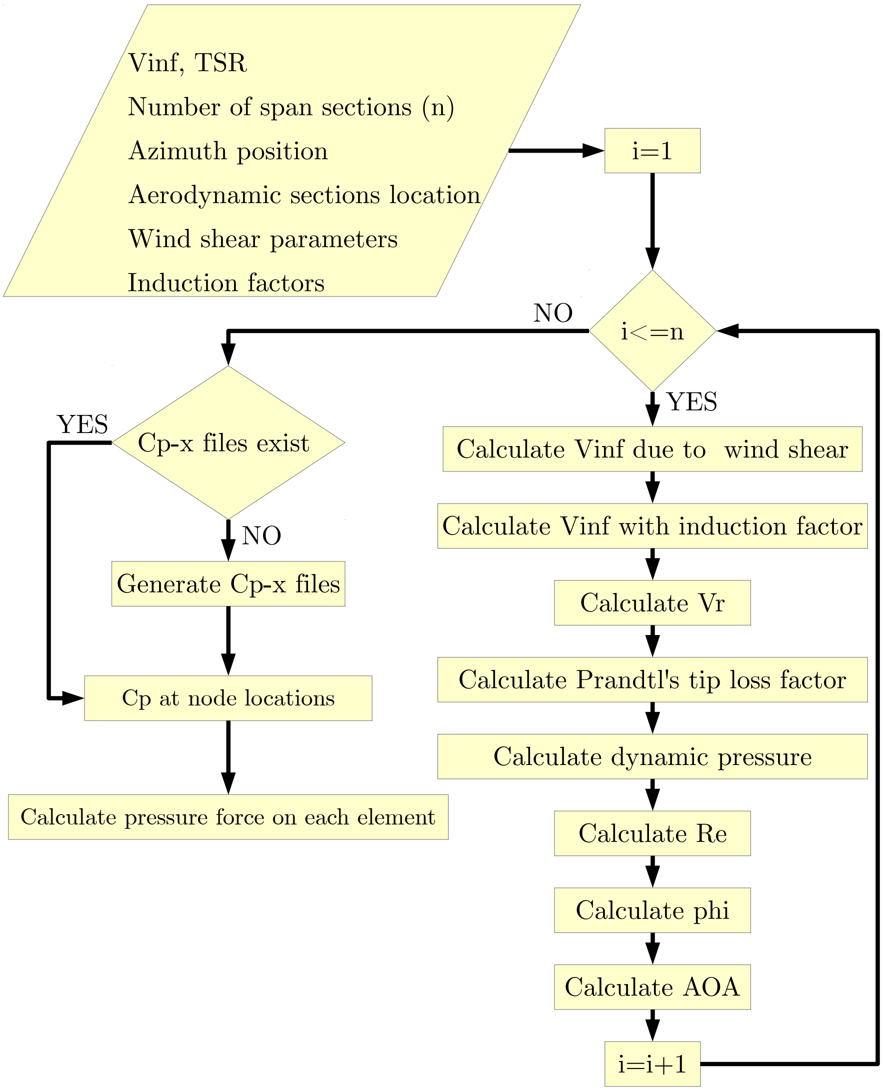

Figure 3.8: Aerodynamic loads flow chart

3.4 MSC Nastran Commands

The input to MSC Nastran should contain all the necessary information about the aerodynamic/structural properties of the blade along with the loading conditions. A well defined design is accomplished in the context of this thesis through the use of the following commands (MD/MSC NASTRAN 2010, Quick Reference Guide [21]):

- <u>GRID</u>: This command specifies each node's xyz coordinates.
- <u>MAT2</u>: In this entry, the stiffness terms of a 2-D anisotropic stress-strain relationship (σ=G*ϵ) are defined for each stack along with its density. For each stack, two MAT2 commands are specified, one that describes the axial stiffness and one that describes the bending stiffness.
- <u>PSHELL</u>: Each PSHELL command indicates a set of shell element properties. These are: 1)the shell's thickness and 2) the axial/bending material properties of the shell (using the appropriate MAT2 identification numbers).
- <u>CQUAD4</u>: This entry specifies each element and assigns at it a set of properties. More precisely, it includes the identification numbers of the 4 grid points that form each element and the identification number of the appropriate PSHELL.
- <u>GRAV</u>: This command specifies the magnitude and direction of the gravitational vector at a selected coordinate system. This vector is multiplied with the mass matrix in order to obtain the gravity force at each node.
- <u>RFORCE</u>: With the use of this entry, the centrifugal force due to the blade's rotation is specified.
- <u>PLOAD4</u>: Through this entry, the aerodynamic loads are applied in the form of a pressure force on each node of each element.

In the FEM input file also the type of analysis (solution) must be specified; however, this will be thoroughly described in the next chapter.

3.5 Smart Rotor

In order to create a deflected airfoil, first an airfoil from the pool must be chosen and the points x_{hinge} and x_{TE} shown in figure 3.9 must be defined. Point x_{hinge} determines the starting point of the deflection and x_{TE} the ending point. If it is assumed that the deflection angle ϕ is small, then the x coordinates of the the deflected airfoil are the same with the original and the y coordinates that are between x_{hinge} and x_{TE} are computed using relation 3.15. The y_2 value calculated is added on the corresponding y value to get the coordinates of the new airfoil. In figure 3.9 an example is presented of an airfoil equipped with a 5° flap ranging from 90-100% of the chord (green) and the original airfoil (blue).

$$y_2 = -\frac{(x - x_{hinge})^2 \phi}{x_{TE} * x_{hinge}} \tag{3.15}$$

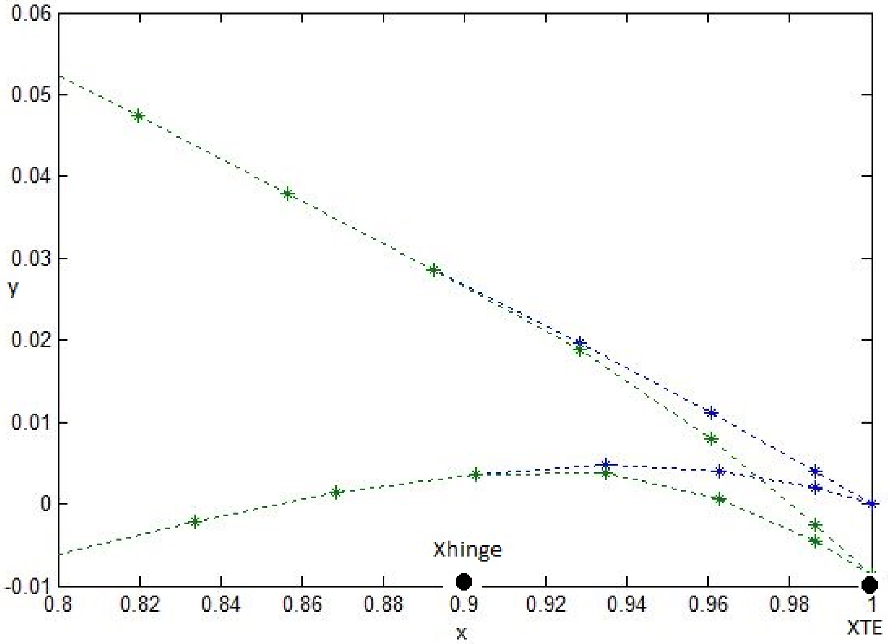

Figure 3.9: Flap Deflection

Once the airfoil is designed, a similar process as the one describe in subsection 3.3.1 is followed in order to compute the pressure loads on the blade. The user decides the spanwise range of the flap airfoil and generates the Cp-x files in XFOIL. Multiple flaps with various angles and at various locations on the blade could be designed and applied. Nevertheless, besides the influence on the structural properties of the blade, the flap should be investigated also about its effect on power production.

Chapter 4

Optimization and Constraints

Once the analysis in the FEM solver is run, the results of this analysis are post processed and evaluated in MATLAB. The local thicknesses of the designed blade are then altered using fmincon in order to achieve the minimum mass that the blade can have under the specified loading conditions, avoiding structural failure. In this chapter, the post process methodology of the failure criteria along with the the optimization logic will be analyzed.

4.1 Distributed Blade Properties

Before the failure criteria are analyzed, it is of great use in blade design to calculate the blade's stiffness and moments of inertia thus it is a common input in aeroelastic codes. In the context of this project no aeroelastic analysis was performed; however, these properties were used for validation of the initial design.

The flapwise and edgewise stiffness distributions along the blade are normally calculated by equations 4.1 presented below.

$$EI_{flap} = \int\int E(x,y)x^2 dxdy \tag{4.1a}$$

$$EI_{edge} = \int\int E(x,y)y^2 dxdy \tag{4.1b}$$

Nevertheless, the solution of this integral for each element can be fairly complex. Therefore, a simplified process was followed in this project. Since the element dimensions are small, it is a common practice in structural design to consider that when the blade is under pure bending, each element is under tension or compression. For this reason, even though we are looking at the flapwise, edgewise stiffness of the blade, the A matrix is used and not the D matrix. Expression 4.2 was used for the calculation of E_{flap}.

$$E_{flap} = A_{XX} - \frac{A_{XY}^2}{A_{YY}} \tag{4.2}$$

The second moment of area of a rectangle with respect to its centroidal axis is given by equation 4.3.

$$I_{flap} = \int\int_{A} x^2 dxdy = \frac{bh^3}{12} \tag{4.3}$$

Nonetheless, it is necessary to calculate the second moment of area relative to a parallel axis (steiner's rule) as shown in equation 4.4, where d is the arm of the element.

$$I^{'}_{flap} = I_{flap} + Ad^2 = \frac{bh^3}{12} + Ad^2 \tag{4.4}$$

E_{flap} is multiplied with I_{flap} in order to compute the stiffness of an element. This procedure is followed for each element of a cross section and the final stiffness of the cross section comes from the summation of the EI values. In order to calculate the edgewise inertia a similar approach is used with the only difference being the corresponding arm of the element and the E_{edge} which is calculated from relation 4.5.

$$E_{edge} = A_{YY} - \frac{A_{XY}^2}{A_{XX}} \tag{4.5}$$

The flapwise mass moment of inertia I_m is computed for each element using relation 4.6 which includes again the summation of the mass moment of inertia of a rectangle plus the steiner's term. Similarly, the mass moment of inertia of a section is calculated by the summation of the I_m values of each element of the section. A similar approach is used for the calculation of the edgewise moment of inertia.

$$Im_{flap} = (x^2 + t^2)\frac{M}{12}/ + Md^2 \tag{4.6}$$

4.2 Failure Criteria-Constraints

The main reasons for structural failure of wind turbine blades are due to:

- **Ultimate strength**: dependent on material strength.
- **Fatigue strength**: dependent on material strength.
- **Global stiffness/Deflection**: dependent on material stiffness.
- **Natural frequencies**: dependent on material mass and stiffness.
- **Global and local buckling**: dependent on material strength and stiffness.

Once the geometry and the materials have been defined and the loads have been applied on the blade, the user must specify which failure criteria will be calculated. Depending on the selection, some of the following types of MSC NASTRAN solutions (SOL) will be executed and the results will be post processed in MATLAB in order to evaluate each criterion.

- **SOL 101: Linear Static Analysis**
- **SOL 103: Normal Mode Analysis**
- **SOL 105: Buckling Analysis**

For each element a score is assigned for every criterion except buckling, with values higher than 1 indicating failure. Those scores are called failure indexes.

4.2.1 Ultimate Loads

To define the ultimate loads on the blade, SOL 101 is selected. The stresses on each element are read from MSC NASTRAN f06 output file and using a Mohr's circle algorithm they are translated to the global coordinate system. The translated stresses are then compared with the allowable stresses using Kassapoglou criterion presented in equation 4.7 and the ultimate stress failure index FI_U is created for each element. The maximum FI_U is selected between all azimuth positions for every element.

$$FI_{Uij} = \frac{\sigma_{ij} SF_U}{\sigma_{uij}} \tag{4.7}$$

where:

- i,j: shows the stress direction (axial, transverse, shear).
- σ: is the element stress at the i,j direction.
- SF_{US}: is the overall safety factor for ultimate stress.
- σ_{ult}: is the allowable stress of the element at the i,j direction.

Furthermore, the algorithm has the option to calculate the forces and moments on each element and through post processing create their distributions along the span. Additionally, besides stresses the user can also request the strain results of each element.

4.2.2 Tip Deflection

In order to obtain the tip deflection, the displacement output of SOL 101 is processed in MATLAB. As shown in equation 4.8, the maximum displacement(u) is divided by the allowable deflection (TD_{all}) defined by the user. Tip deflection depends on the blade's flapwise material stiffness. In blade design, the main contributors to flapwise stiffness are the spar caps, therefore they also have the largest influence on tip deflection.

$$FI_{TD} = \frac{max(u)}{TD_{all}} \tag{4.8}$$

4.2.3 Fatigue

A highly important design aspect of wind turbine blades is their strength to fatigue loads. It is a fact that there are several fluctuating loads affecting wind turbines. These loads come from a great variety of sources such as turbulence, tower shadow, wind shear, yawed flow etc. All these fluctuating loads create fatigue on the blades and the rest components of the turbine which leads to a decrease of their lifetime, increase of the maintenance and therefore the overall cost of energy. For example, wind variations and wind shear create alternating flapwise and edgewise bending, which results to fatigue of the materials. Furthermore, due to the blade's rotation, the edgewise bending alters which also leads in its turn to fatigue loads.

The fatigue life of a composite material can either be regarded as the loss of adequate stiffness or a loss of adequate strength. During the design, the fatigue load cycles that the blade experiences during power production over the full operational wind speed range have to be taken into consideration. In contrast to metals, in composites materials fatigue damage occurs in a more complicated manner. First, the matrix cracks and the cracks combine, then debonding between the matrix and the fibres occurs, after that comes the delamination and finally the fibers break.

In order to evaluate the fatigue failure criterion, the commonly used Miner's sum is applied in combination with a rainflow counting algorithm. A similar approach is used at the Sandia project and is thoroughly described at Appendix A of the Sandia 100m Blade report. Through rainflow counting, utilizing the stresses found for each azimuth position, the stress ranges and their cycles are obtained for each element per revolution. The accuracy of the fatigue results increases as the number of azimuth positions increase since more load cycles are introduced. Equations 4.9 are used in order to calculate the fatigue damage of each element, assuming that the blade rotates in its lifetime under the same operational/loading conditions.

$$F_D = \sum_i \frac{n_i}{N_f} \leq 1 \tag{4.9a}$$

$$N_f = \left(\frac{S(\gamma_f \gamma_m)}{C}\right)^{-b} \tag{4.9b}$$

where:

- S_i: is the stress level i.
- n_i: is the number of cycles at stress level i.
- N_f: shows the number of cycles to failure.
- γ_f, γ_m: are the partial safety factors for loads and materials respectively.
- C: strength of material.
- b: inverse slope of the S-N fatigue life curve.

The ultimate stress, tip deflection and fatigue analysis emerge from post processing of the SOL 101 stress results. All processes related to SOL 101 are presented in the flowchart of figure 4.1. The selection of which analysis will be conducted is made by the user through a number of switch variables:

- k_u: for ultimate stress analysis.
- k_m: for forces and moment results.
- k_d: for displacement results.
- k_e: for strain energy results.
- k_f: for fatigue analysis.

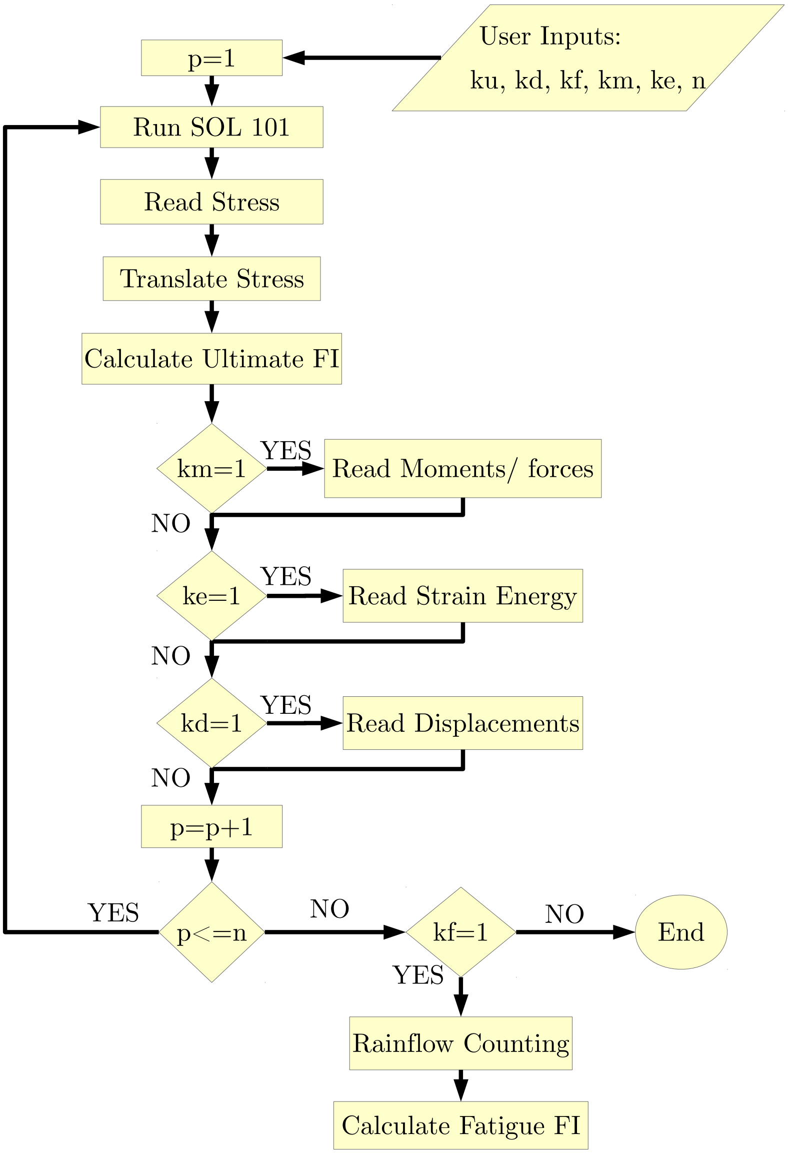

Figure 4.1: Flowchart of processes related to solution 101

4.2.4 Buckling

The increasing trend of optimization for structures is leading to thin walled and slender structures which tend to buckle under axial loading. More precisely, buckling is a failure mode connected with thin structures that are under compression load and their strength limit has not been surpassed, leading the structure to become unstable which means that there is a point that even if the loading stops increasing, the structure continues to deflect. Buckling on the blade can reduce its compressive strength and stiffness and may lead to the development of other failure modes such as fiber failure.

Linear buckling analysis is performed in MSC NASTRAN using Using SOL 105. The main reasoning behind buckling analysis can be understood if one considers the linear equation of motion for a preloaded structure presented below (MSC NASTRAN Linear Static Analysis manual [20]):

$$M\ddot{u} + C\dot{u} + Ku + K^d u = P(t) \tag{4.10}$$

And the harmonic solution:

$$u = \phi * \sin(\omega t) \tag{4.11}$$

Which ignoring the damping term leads to:

$$-\omega^2[M]\phi \sin(\omega t) + [K + K^d]\phi sin(\omega t) = 0 \tag{4.12}$$

Which is in the form of an eigenequation.

$$([K + K^d] - \omega^2[M])\phi = 0 \tag{4.13}$$

Where:

- M: mass
- C: viscous damping
- K: material stiffness
- K^d: differential stiffness (connected to the potential energy change)
- P(t): force
- ϕ : eigenvector which represents virtual displacements
- ω : natural frequency

For a static analysis the inertia term is cancelled since the frequency of vibration is zero. A non-trivial solution of the above equation can be obtained from an eigenvalue that makes [K+K^d] vanish. In general, a structure has an infinite number of degrees of freedom, however in FEM the number of degrees of freedom is finite. The number of eigenvalues (so also the number of buckling loads) is equal to the number of degrees of freedom. This gives:

$$[K + \lambda K^d]\phi = 0 \tag{4.14}$$

where λ is an eigenvalue that reflects the factor that the applied load must be multiplied in order to reach the critical buckling load. These eigenvalues are the results of the FEM analysis and are post processed in MATLAB. An eigenvalue with a value lower than 1 indicates failure. The failure index of buckling is calculated as shown in equation 4.15. The safety factor for buckling is also input to MSC NASTRAN.

$$FI_{BU} = {EV_{min}}^{-1} \tag{4.15}$$

4.2.5 Modes

The eigenfrequencies of the blade can be calculated using SOL 103. Furthermore, the campbell diagram of the blade can be created by computing the eigenfrequencies for a varying rotor angular velocity. The option to include the eigenfrequencies as constraints in the optimization has also been added. An upper limit on each eigenfrequency can be set as a constraint and a lower limit as a boundary condition. If the eigenfrequency surpasses the upper limit, then the failure index becomes larger than 1. This option can be used in order to optimize the thicknesses of the blade to avoid resonance; however, in the optimizations executed in this project the mode constraints were not included. An interesting methodology for the blade's optimization would be to minimize the blade's weight satisfying the ultimate stress, tip deflection, buckling, fatigue constraints and use this optimized design for eigenfrequency optimization in case resonance occurred in the optimized design.

4.3 Optimization

The nonlinear constrained multidisciplinary minimization algorithm fmincon (developed by MATLAB) is used for the mass minimization of the blade. This algorithm's goal is to find a vector x that is a local minimum to a scalar function f(x), always satisfying a set of independent variable boundaries and a set of equality/inequality constraints (MATLAB manual). One of the key characteristics behind the reasoning of fmincon is to convert a complex problem into an simpler problem that can be solved through an iterative process.

Fmincon offers four different algorithms for optimization, each of which has a different mathematical background. Similar to Schelbergen [25], the Sequential Quadratic Programming (SQP) algorithm was selected due to the fact that it performs better than every other tested method in terms of efficiency, accuracy, and percentage of successful solutions (MATLAB SQP Manual [1]). The SQP algorithm transforms a constrained problem into a sequence of unconstrained problems which solutions converge to the solution of the original (constrained) problem. The objective and the constraint functions are combined into a merit function that has to be minimized. Penalty functions are used on the constraints according to their position relative to the constraint boundaries. Small steps are taken relative to the current point and the gradients of the merit function are computed. More information about the optimization options is provided in **??**.

In practice, the main purpose of fmincon is to minimize an objective function f(x) with a design vector x, satisfying the following conditions (MATLAB fmincon manual [2]).

$$c(x) \leq 0 \tag{4.16a}$$

$$ceq(x) = 0 \tag{4.16b}$$

$$A * x \leq b \tag{4.16c}$$

$$Aeq * x = beq \tag{4.16d}$$

$$lb \leq x \leq ub \tag{4.16e}$$

where:

- c(x): are non-linear inequality constraints. For example, if the blade's mass is f(x) and the thickness is x, then the ultimate stress, buckling, tip deflection and fatigue are c(x) equations and their value should be less than zero in order for the blade to not fail under these criteria.
- ceq(x): are non-linear equality constraints. Similar to c(x) with the only difference that the functions values should be equal to 0.
- A: is a matrix that includes linear inequality constraints applied on the design vector. If A is an m-by-n matrix, then there are m constraint functions on a variable x with n components.
- b: is a vector for linear inequality constraints. If A is an m-by-n matrix then b vector has m components.
- Aeq: Matrix for linear equality constraints. Similar to A, if Aeq is an m-by-n matrix, then there are m constraint functions on a variable x with n components.
- beq: Vector for linear equality constraints. If Aeq is an m-by-n matrix then beq vector has m components.
- lb: Vector of lower bounds on the design vector.
- ub: Vector of upper bounds on the design vector.

At the end of each optimization iteration, the function value, the design vector, the step value and the constrain violation are shown.

4.3.1 Objective Function

The main goal in wind energy is to maximize the energy yield of the turbine while minimizing the cost. In the context of this project, the optimization tool minimizes the cost/mass of the whole blade by optimizing the various thicknesses of the blade. However, in reality the various materials don't have the same cost. Also, it is common practice when optimizing composite materials that the number of plies and the ply angles are altered and not the whole thickness of the stack. It is recommended for future research to extend the capabilities and the accuracy of the optimization tool by taking into account the various costs of each material and develop a more complex method that optimizes the number of plies and the ply directions. Furthermore, an initial algorithm for altering the blade radius has been created, that also takes into account the blade area and the maximum power coefficient, but no optimization case that includes this parameter was analyzed. The introduction of the rotor radius in the optimization is also recommended for future research. In short, the optimization tool designed uses as objective function the blade's mass only and the rotor area remains unchanged. The objective function is normalized by its initial value.

4.3.2 Design Variables

As mentioned earlier, the design variables are the factors that are altered in order to achieve the minimum mass. The user can choose which section thicknesses will form the design vector. It is suggested to group thicknesses because a smaller number of design variables can greatly reduce the optimization time. Nonetheless, the number of design variables should describe in a realistic way the structure. Furthermore, the closer the initial design is to the optimum solution, the less the convergence time. Moreover, it is recommended that the initial design does not violate any constraints. Similar to the objective function, the design vector is normalized by its initial value.

4.3.3 Non-Linear Constraints

All the structural criteria described previously in this chapter are expressed as non-linear inequality constraints. Each criterion has failure indices which are translated to inequality constraints by abstracting 1 as shown in equation 4.17. The optimized design should be structurally durable and satisfy all possible failure criteria, however if a large number of constraints is analyzed: first there is the possibility for the optimization to become overconstrained and second the optimization time will increase.

$$c = FI - 1 \tag{4.17}$$

The algorithm developed has also the option to include boundaries and linear constraints; nonetheless they were not needed in any of the test cases examined.

4.3.4 Optimization Options

The user has to define a number of options for the optimization. Information on these options can be found in MATLAB fmincon manual [2].

- DiffMinChange: This option defines the minimum step size. As stated by Schelbergen [25], this variable is very important because if it is set too low then during the optimization the FEM input might not change so the FEM output will also not change. In that case, the gradient computed by the optimizer will be zero and it will be impossible to determine the direction of the merit function in the design space.
- DiffMaxChange: Similar to the above, this option defines the maximum step size. By altering this value the accuracy of the gradient approximations changes.

- Tolx: This value shows the termination tolerance on x. This means that fmincon stops if the solver attempts to make a step smaller than TolX.
- TolFun: This value shows the termination tolerance on the objective function value. This means that fmincon stops if during a step from x_i to x_{i+1}, f(x_i) f(x_{i+1}) ¡ TolFun is true for the objective function values.

The user has also the option to choose whether to run multiple processors in parallel for a faster optimization by enabling the useparallel option. This is highly recommended since it can reduce greatly the optimization time especially if the simulation is executed in a cluster of computer units.

Chapter 5

Initial design

In order to test the validity of the algorithm, a case study was developed that uses as inputs the geometry and the materials of the 5MW, 61.5m Sandia wind turbine blade. Furthermore, this design was analyzed in MSC Nastran, as desribed in chapter 4, and finally the blade's thicknesses were optimized using fmincon. In this chapter the tool inputs are described together with the tool's validation. The reasoning behind each input was analyzed in chapter 3. During the creation of the algorithm, the following targets were set in order to check the validity of the FEM input part of the code.

- Match the total mass of SANDIA.
- Match the mass distribution of SANDIA.
- Match the spanwise edgewise and flapwise stiffness distribution of SANDIA.
- Match the spanwise edgewise and flapwise moments of inertia distribution of SANDIA.
- Match the chord and twist distribution of SANDIA.
- Match the modal frequencies of SANDIA.

5.1 Geometry Inputs of HAWT Design

In order to accurately represent the geometry of the Sandia blade, after iteration the blade was divided in 10 control points along the span. As shown in table 5.1, for every control point the x,y and z coordinates were provided along with the chord and twist angle. The coordinates and the chord were normalized by the blade length which was set to 61.5m.

Next, the blade was divided in 15 spanwise sections. At the beginning of each section an airfoil was assigned. The airfoils and their span range are shown in table 5.2. Instead of adding intermediate sections like Sandia did in order to represent ply drops more accurately, the shape of the airfoil, the chord and the twist angle are interpolated between sections to achieve smooth transition and continuity. By using a narrow spar cap with an

Point Nr.	normalized x (-)	normalized y (-)	normalized z (-)	normalized chord (-)	Twist (deg)
1	0	0	0	0.0551	13.308
2	0.022	0	0	0.0551	13.308
3	0.166	0	0	0.0741	13.308
4	0.233	0	0	0.0756	11.48
5	0.366	0	0	0.0691	9.011
6	0.433	0	0	0.0652	7.795
7	0.566	0	0	0.0569	5.361
8	0.7	0	0	0.0489	3.125
9	0.933	0	0	0.0339	0.37
10	1	0	0	0.0177	0

Table 5.1: Geometry inputs for initial design

Span (%)	Airfoils
0	circle
6.67	circle
13.33	DU99-W-405
20	DU99-W-405
26.67	DU99-W-350
33.33	DU99-W-350
40-46	DU97-W-300
46.67	DU91-W-250
53.33	DU91-W-250
60-66.	DU93-W-210
66.67	DU93-W-210
73.33	NACA-64-618
80	NACA-64-618
86.67	NACA-64-618
93.33	NACA-64-618
100	NACA-64-618

Table 5.2: Airfoils used along the blade's span

adequate thickness of carbon, cap buckling is reduced, therefore the caps were placed at the 0.35-0.55 % of the chord.

After iteration, a NURBS polynomial degree equal to 5 and an inter-element continuity of 4 were found to be a good balance of computational time and accuracy since above this number there was not a significant increase in the accuracy of the results. The final geometry can be seen in figure 5.1, the rest views are shown in **??**.

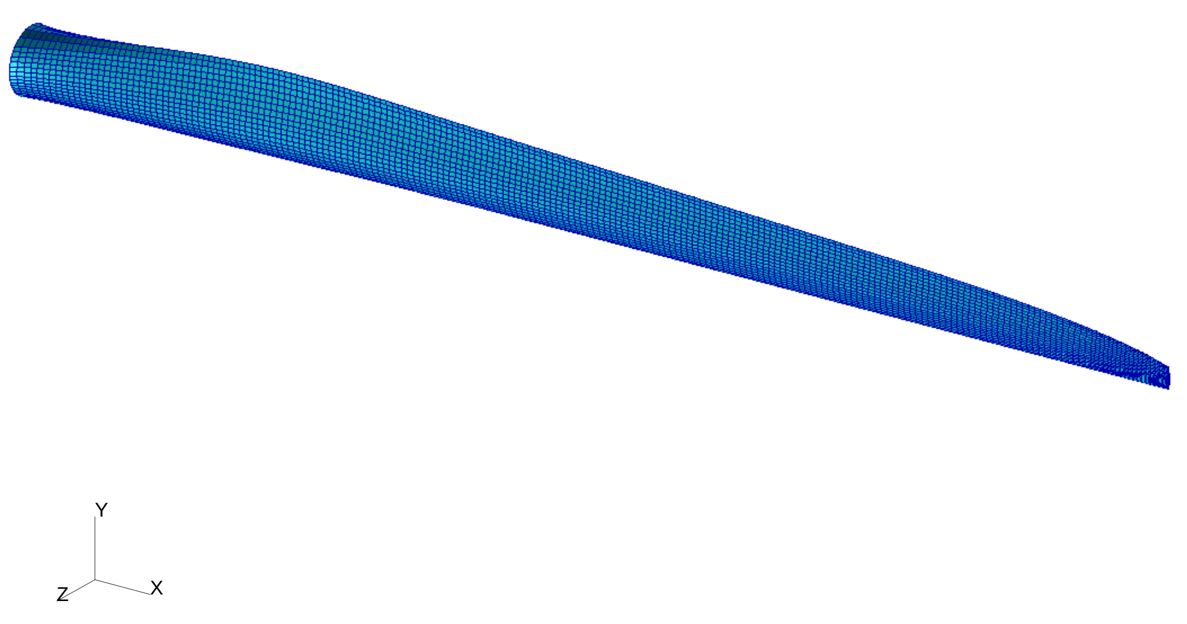

Figure 5.1: Final geometry in MSC Patran

5.2 Materials

As previously mentioned, in order to evaluate the validity of the tool created, a blade that matches the aerodynamic and structural properties of the Sandia 5-MW blade is designed. The structural properties are highly dependent on the geometry and materials used. The geometry is related to the chord, twist and airfoil distribution and the materials on the type of ply-materials used, the stacking sequence of the plies and the angle of each ply. Detailed information about the material properties and stacking sequence/angles can be found in the Sandia Excel spreadsheet (NuMad.xls) and the Matlab tool NuMad that is created for analysis in Ansys and provided by Sandia.

The stacks differ along the span and chord in order to account for the various failure phenomena (deflection, maximum moment-stress, buckling etc.)that may occur on different locations and in order to keep the weight/structural integrity balance as low as possible. Along the cross section, the blade is discretized into 11 different parts as shown in figure 5.2. Along the span, the blade is divided into 6 sections, as shown in figure 5.3, each of which is constituted of the same materials and stacking but different thickness. Below, some important design considerations are presented.

- The spar box includes two shear webs (SW) that are mainly composed out of fiberglass with epoxy resin and two girders that are mainly composed out of carbon.
- The box is positioned such that SW1 is located close to the maximum chord (in order to provide a support to aft panels).
- Since the girder accounts mainly for the flapwise stiffness of the blade, its size (length-thickness) must account for the correct flapwise stiffness distribution.
- The trailing edges (TE) are reinforced in order to account for a higher load capacity and also to increase edgewise stiffness.
- Large thickness drops are avoided at the transition spots of the leading edge (LE), girder (Cap) and panels.

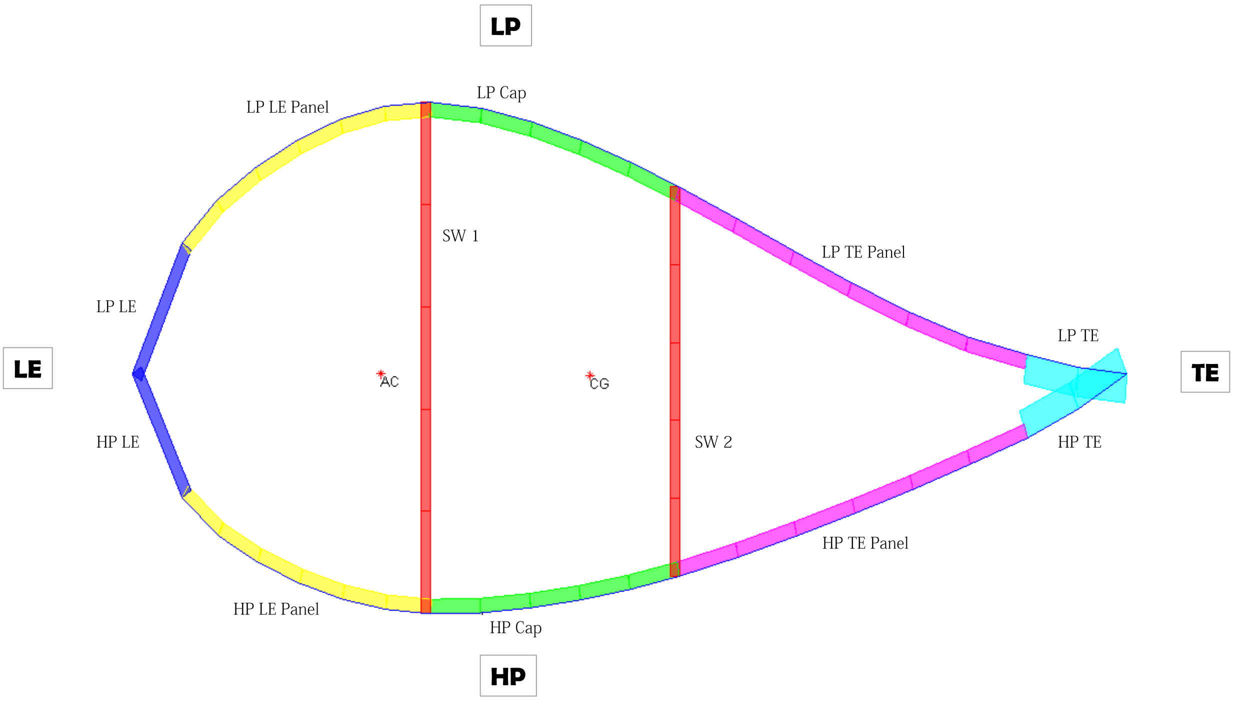

Figure 5.2: Chordwise sections with different materials

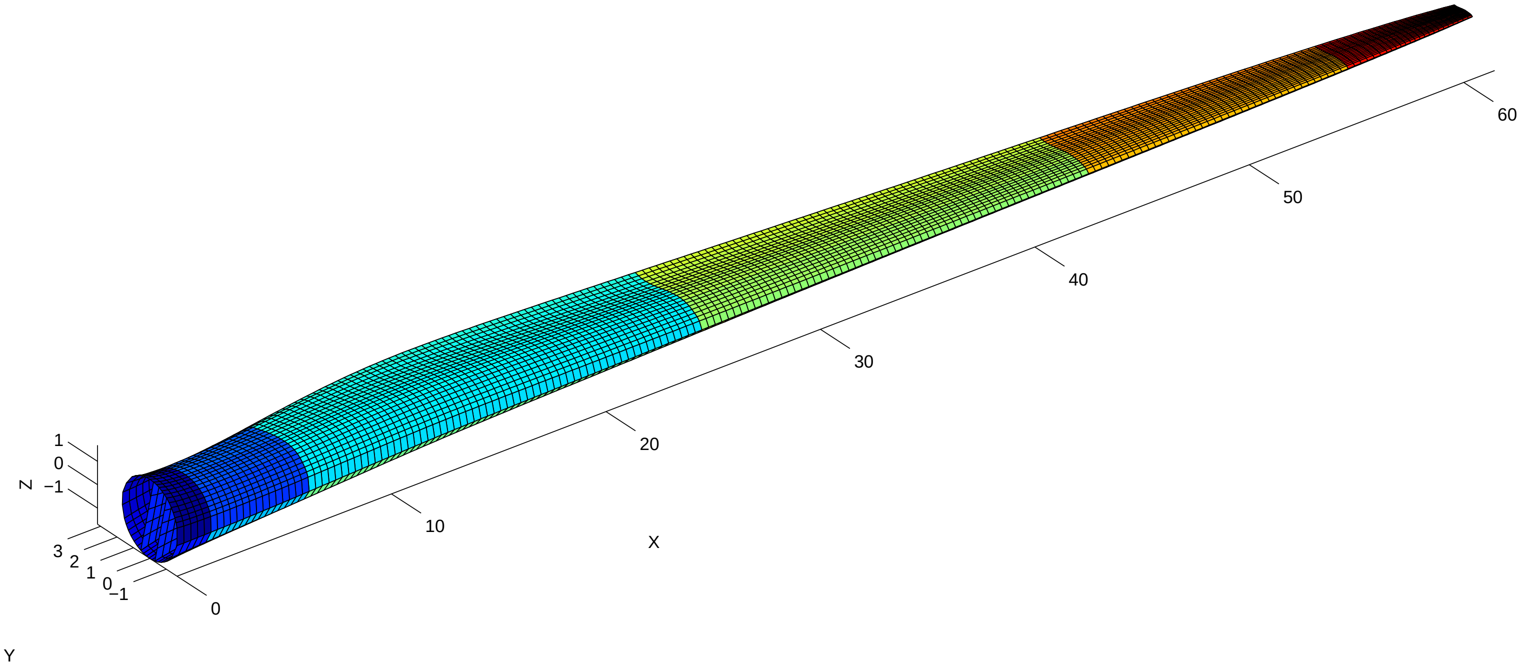

Figure 5.3: Flapwise sections with different materials

In the NREL/DOWEC blade reports no composite layup was provided, so Sandia in their 100m blade project made a selection of materials in order to match the scaled mass/stiffness properties of the NREL/DOWEC projects and at the same time be realistic-manufacturable. However, in their 61.5m reference blade, Sandia provides a very detailed layup. The final design of that layup came after testing and optimizing those materials. All the elastic, maximum stress information are included in the Sandia material database. The main material used in every stack (and at most at the skin) is the SNL Triax material which is a conceptual material and its elastic properties are an average of the E-LT-5500/EP-3 (E-glass/epoxy laminate)uniaxial material and the Saertex/EP-3 biaxial material, which are actual materials tested and reported in the DOE/MSU materials database. EP-3 is the epoxy resin that is used as a matrix material and E-LT-5500/EP-3 is a uni directional E-glass/epoxy laminate. In table 5.3 the properties of the materials used are presented.

5.2.1 Layout

At table 5.4, the stacks and the materials included in each stack are presented. At the first column the identification number of each stack is shown. If the stack is a sandwich material then the parameter t_f appears which shows the thickness of the foam core. In that case the materials presented in the corresponding stack constitute only one of the

Materials	lay-up (-)	E_{xx} (GPa)	E_{yy} (GPa)	G_{xy} (GPa)	v_{xy} (-)	X_t (MPa)	X_c (MPa)	Y_t (MPa)	Y_c (MPa)	S (MPa)	ρ (kg/m^3)
SNL Triax	$[\pm45]_2[0]_2$	27.7	13.65	7.2	0.39	600	500	600	500	70	1850
Foam	-	0.256	0.256	0.256	0.3	1	1	1	1	70	200
Saertex	$[\pm45]_4$	13.6	13.3	11.8	0.49	144	213	144	213	70	1780
Carbon	[±45/(0)4C]S	114	8.39	5.99	0.27	1546	1047	46.4	250	70	1220
E-LT-5500	$[0]_2$	41	14	2.63	0.28	972	720	46.4	250	70	1920

Table 5.3: Material Properties

two panels. Most stacks (except one) are cross-ply and symmetric which means that the B matrix and A_{16}, A_{26}, D_{16}, D_{26} are 0.

Stack Number	Ply 1	Ply 2	Ply 3	Ply 4	Ply 5	Ply 6
1	Triax (0.0026)	Triax (0.047)	Triax (0.0026)	-	-	-
2	Triax (0.0026)	Triax (0.0026)	-	-	-	-
3 (t_f=0.02)	Triax (0.0026)	Triax (0.021)	Glass (0.0025)	Triax (0.0026)	-	-
4 (t_f=0.09)	Triax (0.0026)	Glass (0.0025)	Triax (0.0026)	-	-	-
5	Triax (0.0026)	Triax (0.021)	Carbon (0.02)	Triax (0.0026)	-	-
6	Triax (0.0026)	Carbon (0.04)	Triax (0.0026)	-	-	-
7 (t_f=0.04)	Saertex (0.002)	-	-	-	-	-
8	Triax (0.0026)	Carbon (0.036)	Triax (0.0026)	-	-	-
9	Triax (0.0026)	Carbon (0.033)	Triax (0.0026)	-	-	-
10 (t_f=0.06)	Triax (0.0026)	Glass (0.0025)	Triax (0.0026)	-	-	-
11 (t_f=0.02)	Triax (0.0026)	Triax (0.0105)	-	-	-	-
12 (t_f=0.09)	Triax (0.0026)	-	-	-	-	-
13 (t_f=0.06)	Triax (0.0026)	-	-	-	-	-
14 (t_f=0.02)	Triax (0.0026)	-	-	-	-	-
15	Triax (0.0026)	Triax (0.047)	Triax (0.0026)	Triax (0.0026)	Triax (0.047)	Triax (0.0026)
16	Triax (0.0026)	Triax (0.021)	Triax (0.0026)	-	-	-
17	Triax (0.0026)	Carbon (0.015)	Triax (0.0026)	-	-	-

Table 5.4: Stacks

At each chordwise and spanwise section the identification number of a stack is assigned as shown in table 5.5.

Span/Chord	C1	C2	C3	C4	C5	C6	C7	C8	C9	C10	C11
S1	1	1	1	1	15	15	1	1	1	1	7
S2	16	16	5	11	3	3	11	5	16	16	7
S3	2	14	6	12	4	4	12	6	14	2	7
S4	2	14	8	13	10	10	13	8	14	2	7
S5	2	14	9	14	14	14	14	9	14	2	7
S6	2	14	17	14	2	2	14	17	14	2	7

Table 5.5: Stack assignment on each spanwise/edgewise section

5.2.2 Thickness distribution

The mass correction algorithm developed by Roscher [24] leads to a change in mass from 17.823 to 17.734 tn. In other words, the cubic spline interpolation algorithm results to a 0.5% decrease of the overall mass but with a more realistic thickness distribution than the initial step function distribution. The thickness distibution can be shown in figure 5.4.

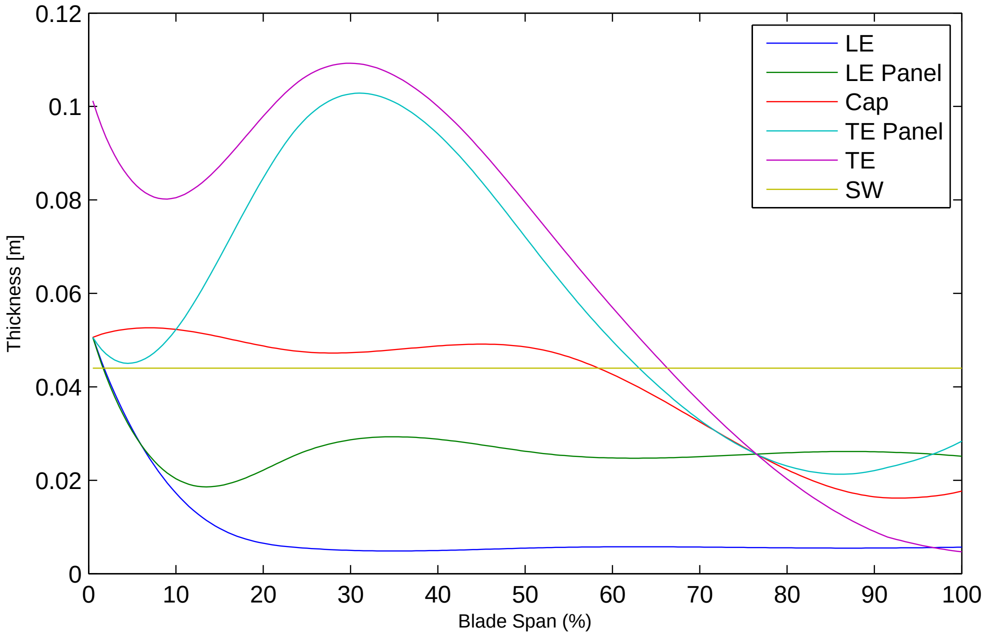

Figure 5.4: Thickness distribution of each chordwise section along the blade's span

5.3 Aerodynamic Loads

Regarding the aerodynamic loads, one load case was investigated and will be presented in this section. In the load case considered, the wind is taken equal to 11.4 m/s which is the rated wind speed of the NREL 5MW wind turbine at hub height. The tip speed ratio for rated wind speed is equal to 7 as it can be seen from the NREL report [16].

Along the blade, 8 different airfoils are used. Inside the range of each airfoil type the coordwise pressure coefficient distribution remains unchanged for each spanwise section(the span is divided into 200 sections). In table 5.6 the aerodynamic sections ranges are presented together with the airfoil at each section, the average Re and the average α values of each section. The pressure coefficients at the circular section close to the root are considered equal to 0 since they produce no lift.

Section Nr	Span	Airfoil	α (°)	Re
1	0-0.025	Circle	-	-
2	0.025-15	Interp0041	23	9E+5
3	0.15-0.233	DU99-W-405	13	4.5E+6
4	0.233-0.367	DU99-W-350	7.2	7E+6
5	0.367-0.433	DU97-W-300	4.6	8.6E+6
6	0.433-0.567	DU91-W-250	3.9	9.5E+6
7	0.567-0.7	DU93-W-210	3.9	1E+7
8	0.7-1	NACA-64-618	4.2	1.1E+7

Table 5.6: Aerodynamic sections range and Re, α for 180 ° azimuth

For future research, the ability to analyze multiple load cases and translate the results into optimization constraints would create a more a realistic optimized design.

5.4 Safety Factors

The safety factors used are presented in table 5.7 and are the same with those Sandia used for their analysis. As stated in the Sandia report these safety factor are based on the IEC standards [27].

Criterion	SF Loads	SF Materials	SF Consequences of Failure	SF Total
Ultimate Stress	1.35	1.3	1	**1.755**
Deflection	1.35	1.1	1	**1.485**
Fatigue	1	1.2	1.15	**1.38**
Buckling	1.35	1.2	1	**1.62**

Table 5.7: Safety factors for all criteria

5.5 Validation

As previously mentioned, the performance of the FEM input part of the tool is verified by calculating the distributed blade properties such as the flapwise/edgewise stiffness, flapwise/edgewise moment of inertia, mass density, chord, twist and the blade's eigenfrequencies.

5.5.1 Distributed Blade Properties

The NREL bladed file was processed and the structural properties of the Sandia blade were input in DNV GL Bladed using the same controller. Identical aerodynamic conditions were created with those of the HAWT initial design and the flapwise bending moment and tip deflection were computed in order to see the validity of the aerodynamic loads applied together with the deflection response to this excitation. As it can be seen in figure 5.5 the flapwise bending moments distribution and the deflection of the HAWT initial design are similar to Sandia. In figure 5.6 a comparison can be seen between the distributed spanwise blade properties of the initial design with the Sandia blade.

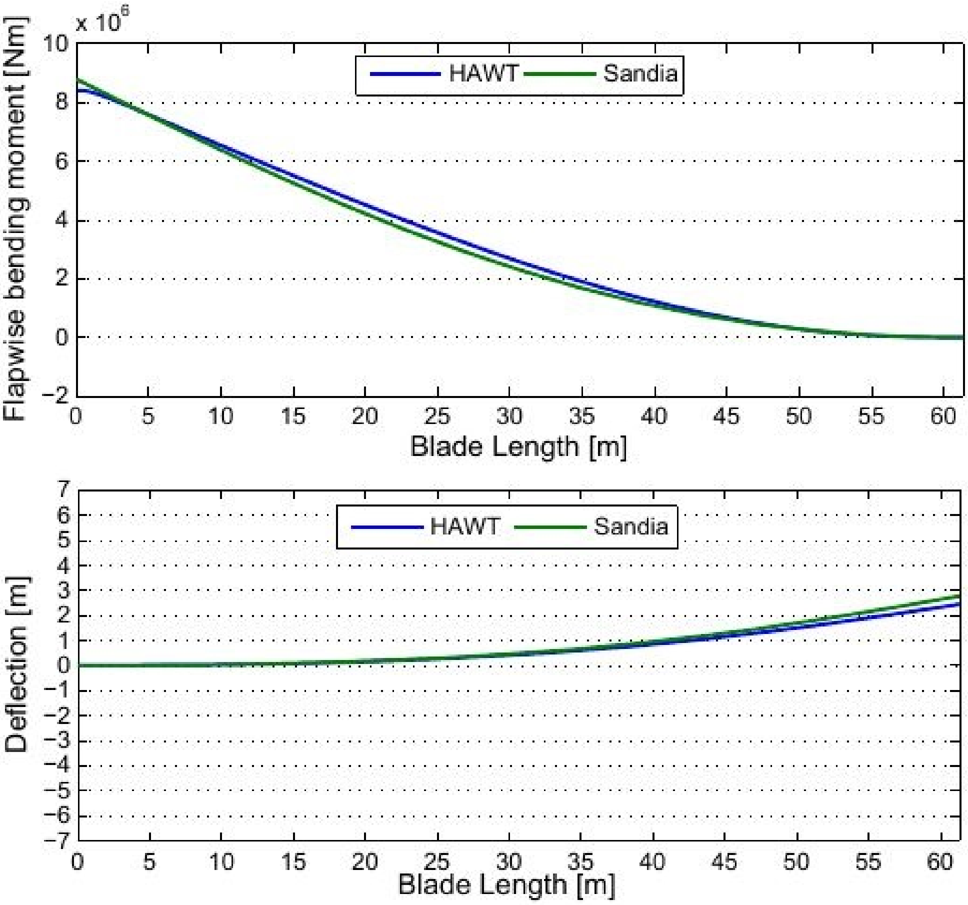

Figure 5.5: Tip deflection for the initial design of the conventional blade

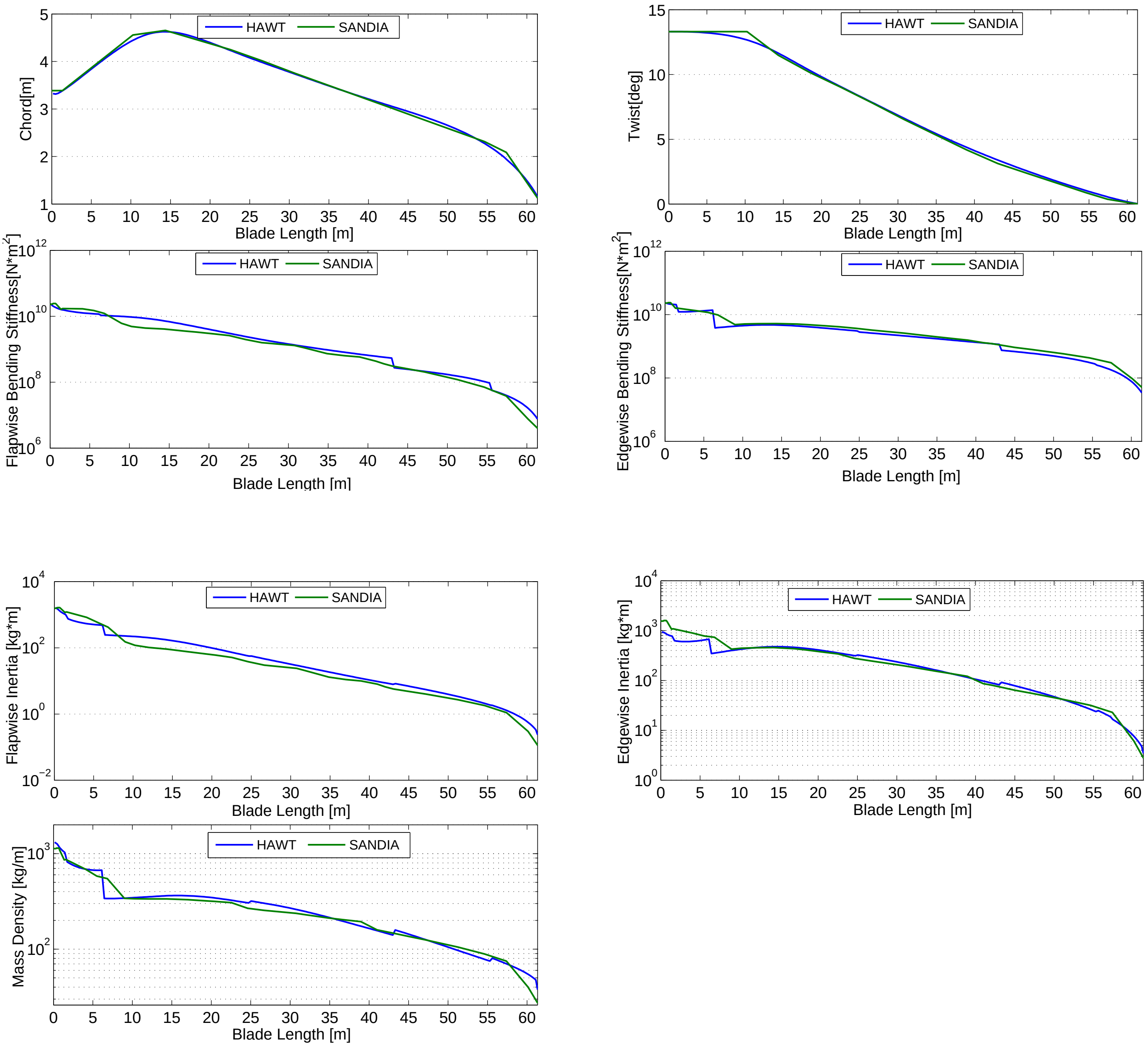

Figure 5.6: Comparison of structural properties between Sandia 5MW blade and the model's initial design

The chord distribution follows the Sandia distribution but with a smoother distribution due to the cubic splines. The twist distribution also matches the Sandia one with the only deviation occurring at the transition point from the root's circular airfoil to DU99-W-405 also due to the spline interpolation. The flapwise bending stiffness distribution follows that of Sandia, with a declination appearing between 7-17m. The first reason behind this declination is due to the different material properties calculation technique in combination with the mass and thickness spline interpolation. As previously mentioned, Sandia specifies manually the properties of each element while in the current model the materials are applied at the beginning of each section (6 sections along the span) and their thickness is then interpolated. The second reason behind this declination is due to the different methodology that Sandia used for the calculation of the flapwise stiffness (Sandia used the software PreComp). Similar deviations can be noticed in the edgewise stiffness and moments of inertia distributions for the same aforementioned reasons.

5.5.2 Mode Analysis

In table 5.8 the eigenfrequencies of the first six modes are compared with those obtained from the Sandia report. A minor divergence from the Sandia values was expected due to the different design methodology followed. More precisely, the geometry generation technique and material properties calculation technique of the Sandia blade differ from the approach followed in this project. Nevertheless, the comparison of the modal frequencies is an indication that the two different techniques resulted to a similar mass and stiffness distribution.

Modes	Description	Sandia (Hz)	HAWT (Hz)	Difference (%)
1	1^{st} flapwise bending	0.87	0.91	-4.4
2	1^{st} edgewise bending	1.06	1.02	3.92
3	2^{nd} flapwise bending	2.68	2.67	0.37
4	2^{nd} edgewise bending	3.91	3.74	4.55
5	3^{rd} flapwise bending	5.57	5.46	2.01
6	1^{st} torsion	6.45	6.61	-2.42

Table 5.8: Mode shapes comparison between HAWT and Sandia blades

5.6 Mesh Convergence

In order to perform the FEA the appropriate mesh has to be created. The fist step is to define a number of sections in the coordwise and spanwise direction. The airfoil is discretized in 11 segments along its coord and each of those segments contains a specified number of elements. Along the span, the blade is discretized into 15 segments, with a different number of spanwise panels in order to make the mesh denser towards the tip. The reason behind this is to achieve a homogeneous element aspect ratio (element x-side)/element y-side) along the span. In case that this tool is used for another blade design then the user may easily select a different number of panels in the coordwise and spanwise direction along with the density of panels in the spanwise direction.

In figure 5.7 the mesh convergence of the maximum stress factor (MSF), the buckling load factor, the strain energy and the simulation time are displayed. At all graphs the y-axis values have been divided by the respective maximum value in order to show the deviation of each value from the densest grid. For a blade structure with a number of elements equal with $\geq$ 10,000, the MSF and strain energy values seem to have converged at a value that shows $\sim \pm$ 1.5% variation. On the other side, buckling values were observed to converge at 27,500 elements; however, an optimization procedure with 27,500 elements would result to a high simulation time. Therefore, for the initial design 10,000 elements were used. More precisely, 200 cross sections were created with 48 nodes and 50 elements per cross section. The final optimization results in the scenarios that include buckling are analyzed with a dense mesh.

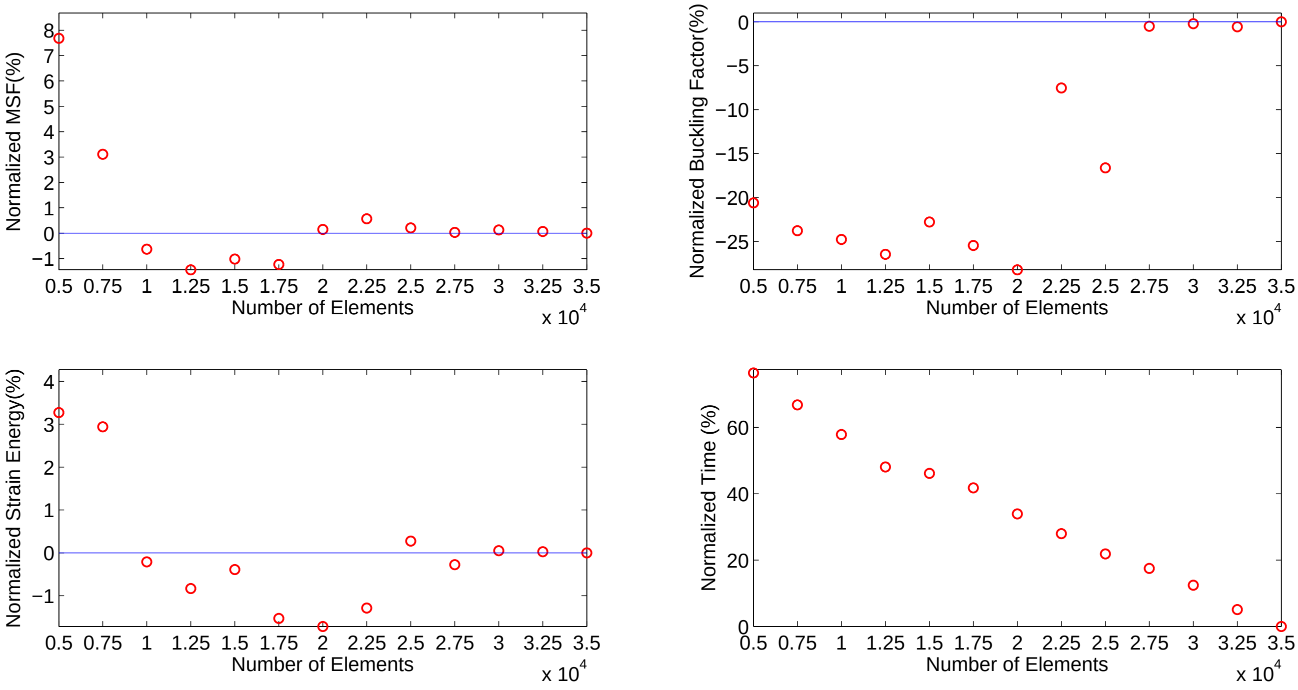

Figure 5.7: Maximum stress factor, buckling load factor, strain energy and time convergence for increasing number of elements

5.7 Optimization

As previously mentioned, the blade has been divided in 6 spanwise sections and 11 chordwise sections which results 66 sections in total. It is possible for fmincon to use 66 design variables; however, due to the great optimization time this optimization would require, the design variables have been narrowed down to 18. So, each chordwise section is separated in 3 sections instead of 11, one that includes the shear web elements (1/11 sections), one for the spar cap elements (2/11 sections)and one for the panels and leading/trailing edge (8/11 sections). Figure 5.8 shows the grouped chordwise sections.

Since no manufacturing or physical restrictions could be set for the thickness of each section, no boundary conditions have been applied on the design vector. If such restrictions appear in a future design they could be easily implemented at the input file of the tool. After iterations developed by Schelbergen [25] the values of DiffMinChange and DiffMaxChange were set equal to 1e-2 and 2e-1 respectively. The values for TolFun and TolX were both set equal to 1e-6.

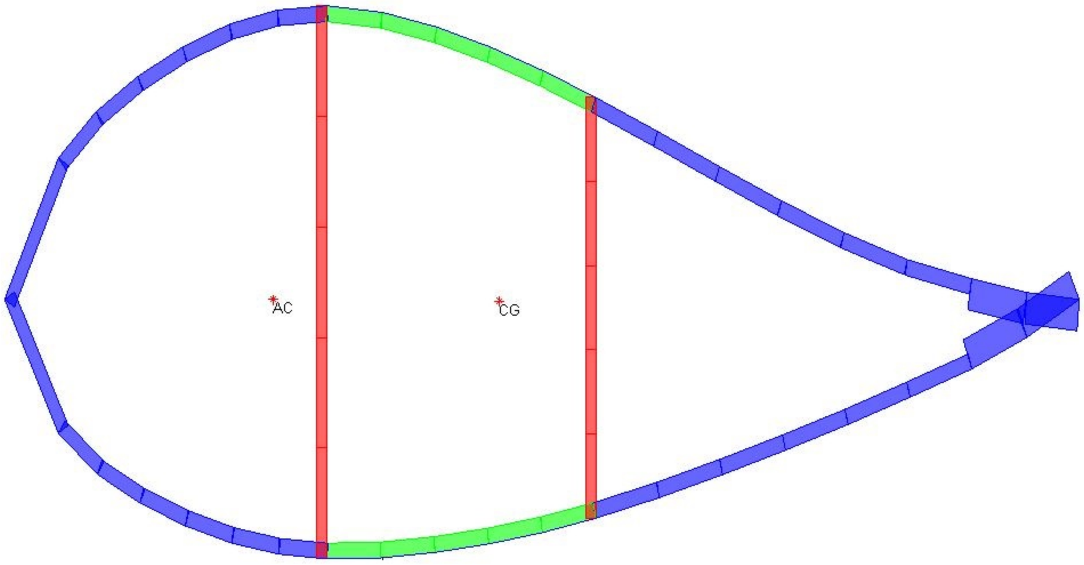

Figure 5.8: Design vector sections (blue: panels, red: shear webs, green:spar cap

5.8 Smart Rotor Initial Design

Similar to the research of Smit [26], a flap was positioned at 78-98% of the span and 90-100% of the chord. In order to find the most suitable flap angle, NACA64618 airfoils with various deformed trailing edge angle were generated (5°,4°,3° and 2°). For those angles, the pressure distributions were computed in XFOIL and simulations were executed to calculate the bending moments on the blade. These bending moments were compared as shown in table 5.9, in order to decide which flap angle will be used. A negative flap angle was used at the 0° azimuth position in order to decrease the lift/bending moment and a positive flap angle was used at the 180° azimuth position in order to increase the lift/bending moment. The bending moments (M_y) at 0° and 180° have the greatest difference among all azimuth positions due to wind shear. The goal is to use the flap to reduce this M_y difference because then the stress deviation will also decrease which means that the fatigue loads will decrease. However, at the same time we should also have a smart rotor max M_y (between all azimuth positions) smaller than the HAWT max M_y, because otherwise the buckling, ultimate stress and tip deflection criteria (which appeared to be dominant in the optimizations) will be higher in the smart rotor and the smart rotor will have a larger mass than the HAWT. The flap angle that satisfied best the criteria was the 2° flap and this angle was used for the optimization.

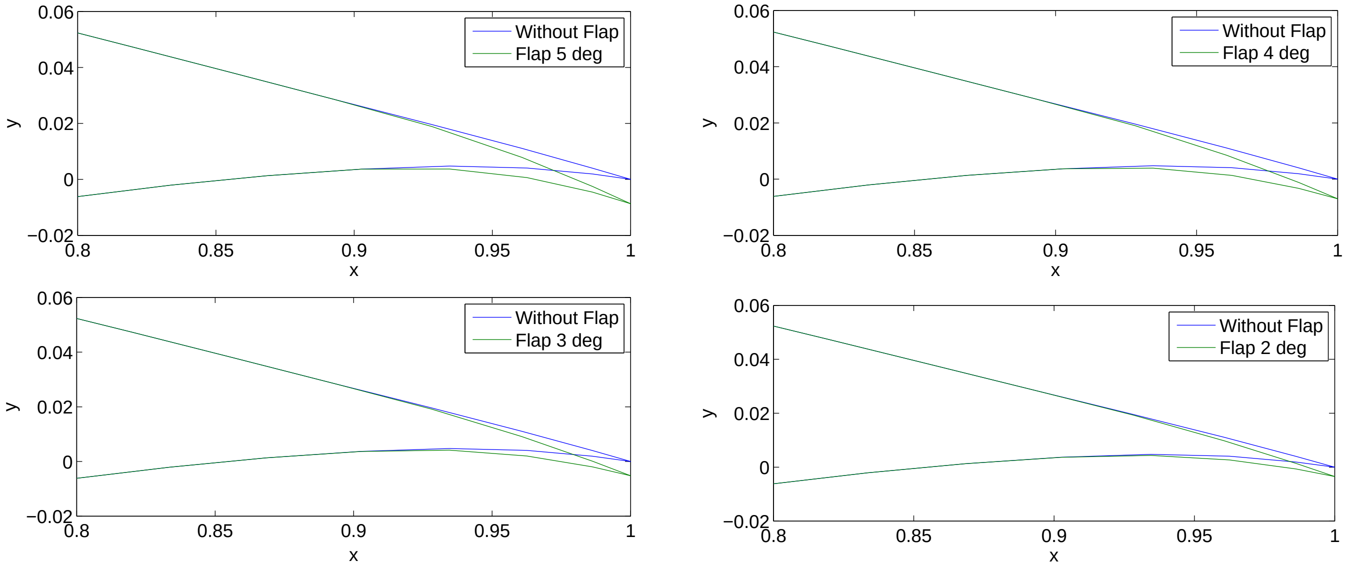

Figure 5.9: NACA-64618 airfoil with various flap angles

flap angles	My 180°	My 0 °	Diff 180-0	Below HAWT max My
No flaps	7.99	8.39	-4.7%	(-)
5°	8.54	7.52	13.5%	NO
4°	8.40	7.64	9%	NO
3°	8.27	7.78	5.9%	YES
2°	8.13	7.94	2.3%	YES

Table 5.9: Bending moment comparison of the various flap arrangements at 0° and 180° azimuths

Chapter 6

Analysis Results

In the previous chapters the generation of the FEM input and the reasoning behind the failure criteria and optimization were described. Summarizing, the scope of this project can be divided into the following sub-goals concerning the tool created.

- A HAWT blade design can be created and meshed in a flexible way, with a small number of variables (as described in chapter 3).
- This blade can be analyzed for various failure criteria and its weight can be minimized by altering the thicknesses of the blade, always satisfying a set of constraints (as described in chapter 4).
- Once the algorithm is created, a HAWT and a smart rotor design were created and parts of the algorithm were validated (as presented in chapter 5).
- The final goal was to analyze both designs, optimize and compare them in order to examine the potential load reduction capability of the smart rotor.

In this chapter the final goal will be presented. For each blade, two kinds of optimization were performed, one that included ultimate stress, tip deflection and fatigue constraints (UL-TD-FA) and one with ultimate stress, buckling, tip deflection and fatigue constraints (UL-BU-TD-FA).

6.1 Conventional Blade (HAWT)

In this section the results of the initial design and the two optimization cases of the HAWT blade will be described and compared. During the initial design, it was found that calculating the fatigue on the blade using 3,4 or 8 azimuth points had a great difference compared to using 16 azimuth points. Thus, the four optimization scenarios and the two initial designs presented were run for 16 azimuth points. It is worth mentioning that as the number of azimuth increases, also the simulation time increases. In case someone wishes to perform a complete structural analysis on a blade it would take approximately 5 minutes for 16 azimuth points with a commercial quad core processor; however, a complete optimization simulation might even take up to 5 full days with the same processor using its cores in parallel. In case a full optimization is performed, it is strongly recommended to use a cluster of processors and enable the parallel processing option which will reduce the optimization time significantly.

6.1.1 Initial Design

As previously mentioned, the MSF is the failure index of ultimate stress and MR is the failure index of fatigue. These failure indices range from 0 to 1 and they are related to the strength of the stack assigned at each element. The maximum MSF value appears on the skin at approximately 10% of the span and it is equal to 26 % of the allowable stress of that element. The maximum MR value is equal to 3.24e^{-10} and appears at the girder at about 7% of the span. The maximum MSF and MR values are detected at the 0° azimuth position where the aerodynamic loading is maximum due to wind shear. Moreover, they are located relatively close to the root where the internal moments are maximum. Nevertheless, these values are not detected at the root but rather close to it, because the root is highly reinforced with extra carbon material. The distribution of MSF for the three blade components is shown in Figure 6.1 and MR in Figure 6.3.

The tip deflection was presented in Figure 5.5 of chapter 5. It is worth mentioning that the allowable tip deflection is equal to 7.07m as stated in the Sandia report. As it can been from Figure 5.5 the deflection is approximately 35% of the allowable. No direct comparison of these results can be made with the structural analysis results of the Sandia report due to the difference of the load cases examined.

In Figure 6.2, the first buckling mode shape and its eiqenvectors are presented. The minimum eivenvalue was observed at the leading skin panel and the girder, at an azimuth angle of 45° and is equal to 2.4104. At this azimuth position the blade has a greater probability to buckle due to it's own weight. The maximum buckling eigenvalue was noticed at 180° where the weight effect is minimum and the aerodynamic loading is the lowest due to wind shear. The rest buckling modes are contained in Appendix A. Furthermore, as presented in Figure 6.4, a Campbell diagram was created. The first and third mode are safe from resonance but the second mode shows that a possible resonance might occur at 5P for rated wind speed. It was observed that the thickness of the carbon of the girder affected greatly the mode shape frequencies, so an increase or reduction of the girder's carbon thickness would aid to avoid resonance.

At table 6.1 the MSF, MR and TD failure indices results are presented along with their location on the blade.

Criterion	Max Index	Span Location	Component
Maximum Stress Factor (MSF)	0.26	10%	Skin
Fatigue (MR)	$3.24e^{-10}$	7%	Girder
Tip Deflection (TD)	0.35	100%	-

Table 6.1: Failure indices and their location for the initial design

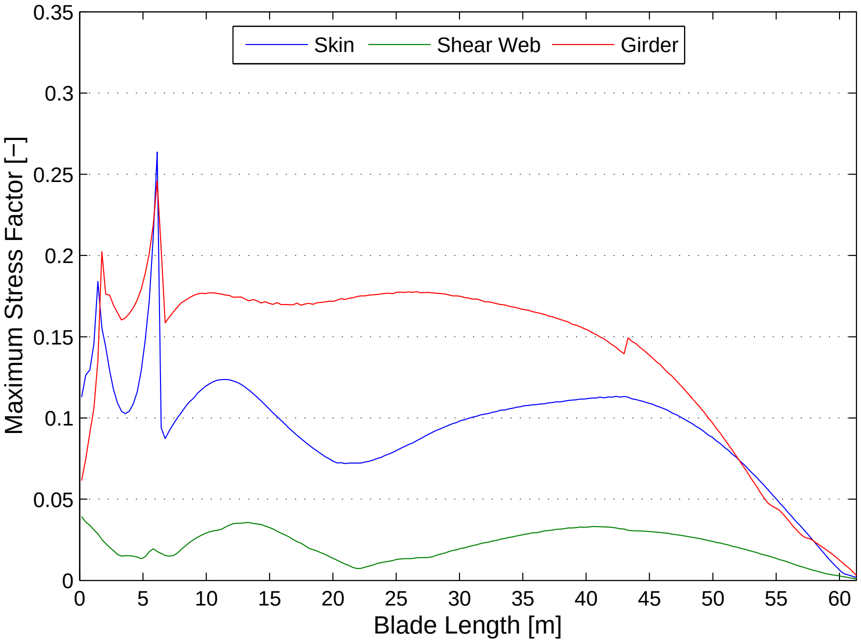

Figure 6.1: Maximum stress factors along the blade for the initial design of the conventional blade

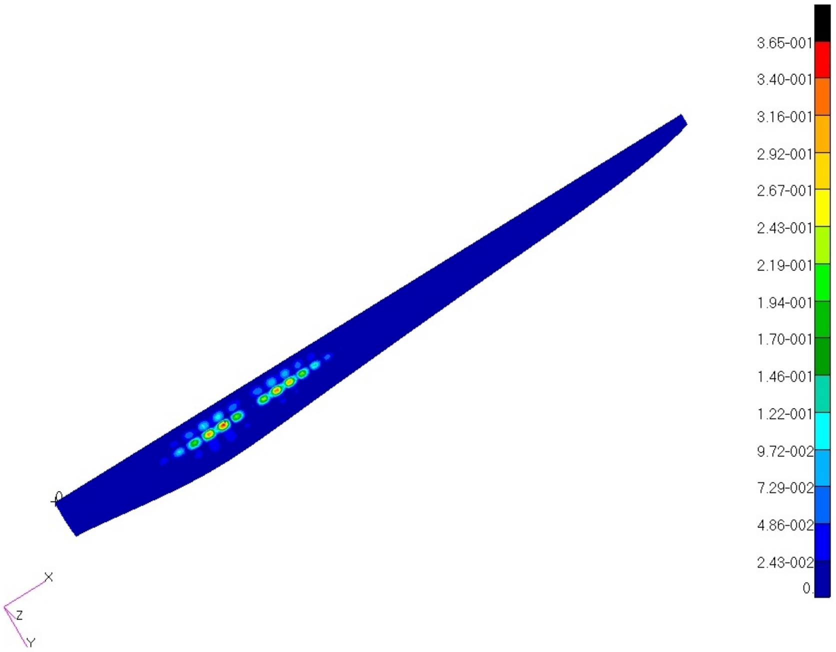

Figure 6.2: First buckling mode for the initial design of the conventional blade

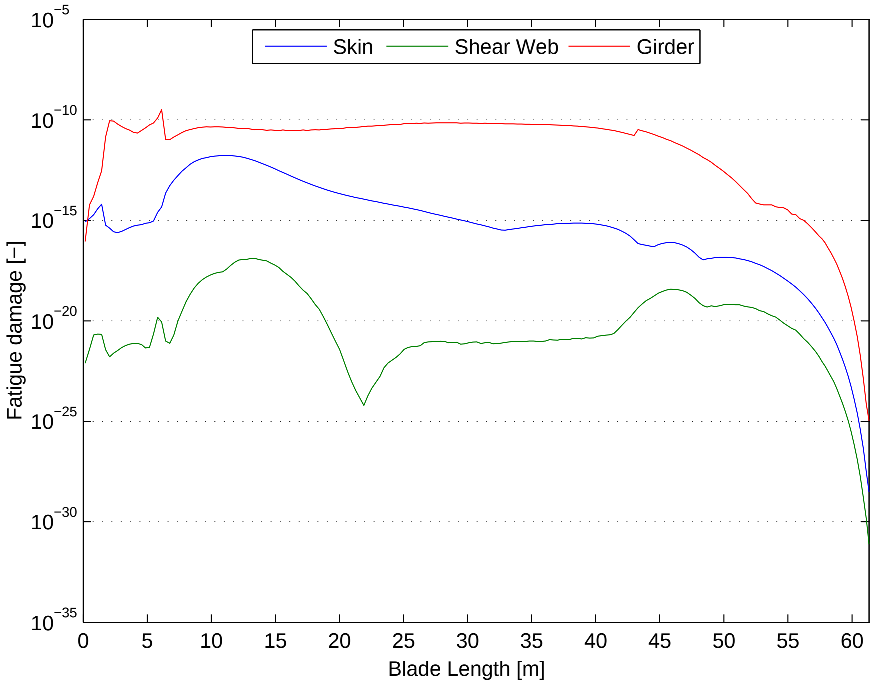

Figure 6.3: Fatigue damage along the blade for the initial design of the conventional blade

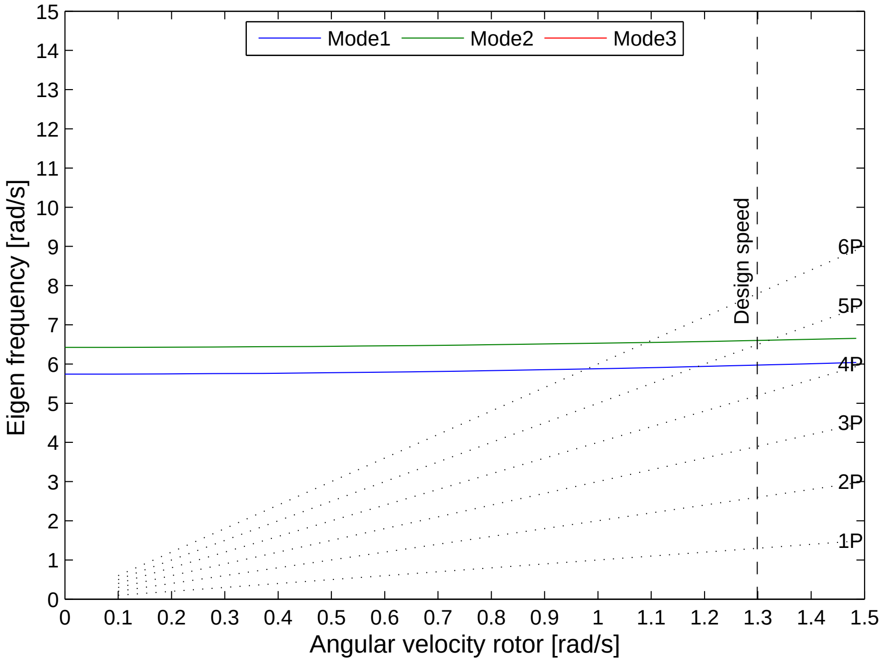

Figure 6.4: Campbell diagram for the initial design of the conventional blade

6.1.2 Optimized Design

The final designs presented in this section constitute blade designs at limit states where they marginally violate the structural constraints. The thickness distribution of each optimized design is significantly altered in order to obtain the minimum weight for each scenario. At any case the final optimized designs do not form feasible blade designs. First of all, the simulations take into account one load case. In the wind turbine design industry, in order to get certification numerous load cases are examined according to the standards. An enhanced algorithm capable of analyzing multiple load cases and create combined structural constraints would result into a more realistic blade initial and optimized design. Secondly, manufacturing issues arise which could be solved by adding realistic boundary conditions.

US-TD-FA

In figure Figure 6.5, the fmincon optimization plot is presented for the US-TD-FA analysis. At the top right the objective function value for each iteration can be seen, at top left the final design vector, at the bottom right the step for each iteration and at the bottom left the constraint violation for each iteration. The final objective function value was 0.2549 which is translated to a blade's mass equal to 4.519tn. As it will be shown in the next section the first main reason for this great reduction lies behind the fact that the blade is buckling driven. The second main reason is because the blade is not created to withstand only the rated wind speed loads but it also has to be durable under extreme conditions.

The new thickness distribution along the span can be seen in figure Figure 6.8. The thicknesses of the leading edge, trailing edge, leading edge panel and trailing edge panel were reduced by approximately 80% and the thickness of the girder by 55%. Furthermore, the thickness distribution of the girder and the shear web showed a great differentiation compared to the initial design. At the initial design, the girder had a constant thickness distribution from 0-60% of the span and after that the thickness was gradually reduced. The shear web on the other hand had a constant thickness distribution along the whole span. In the optimized design, the thickness of the girder exhibits a wobbly behavior in the 0-60% of the span, having a peak at 10% where the maximum stresses appear. The shear web displayed a more complex distribution reducing its thickness until 10% of the span and then gradually increasing until the tip where it reaches its pick value.

The maximum fatigue damage (figure Figure 6.6) of the optimized design was 4.82e^{-4} and the MSF (Figure 6.7) slightly surpassed the limit and reached to 1.0035. As it was described in chapter 4, the optimization convergence stopping criterion is actually an upper limit at the difference of the step size or objective function between two iterations. The converged design slightly violates a set of constraints by a value lower than the variable TolCon. Similar to the initial design, the maximum MR and MSF appeared close to the root. Moreover, since the highest flapwise bending moment is observed at 0° azimuth, the maximum MSF appears at this position. Likewise, the maximum tip deflection is also observed at 0° and is equal to 98,39 % of the allowable deflection. Nevertheless, the tip deflection at 180° (95% of the allowable) deserves attention since at this azimuth a possible impact on the tower might occur. Local reinforcement of the blade's skin close to the root will reduce the maximum MSF value below the allowable limit.

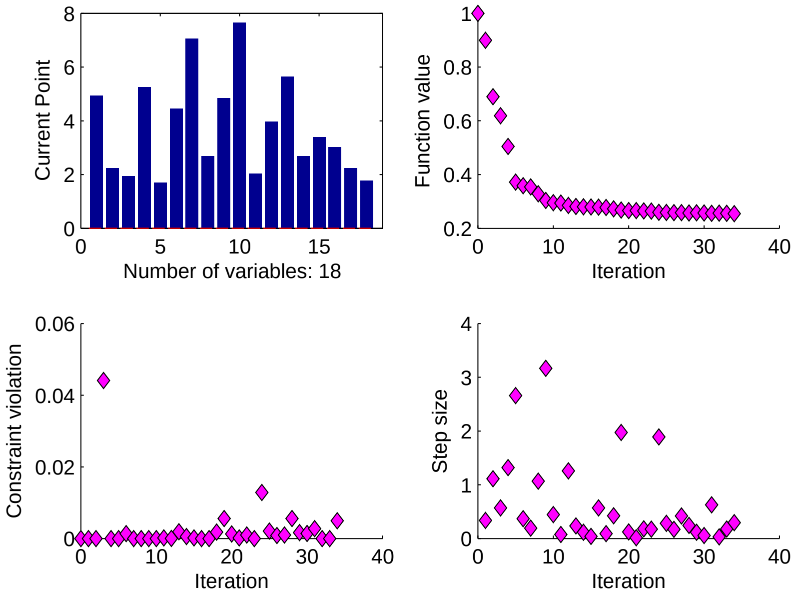

Figure 6.5: Optimization plots for the US-TD-FA load case of the conventional blade

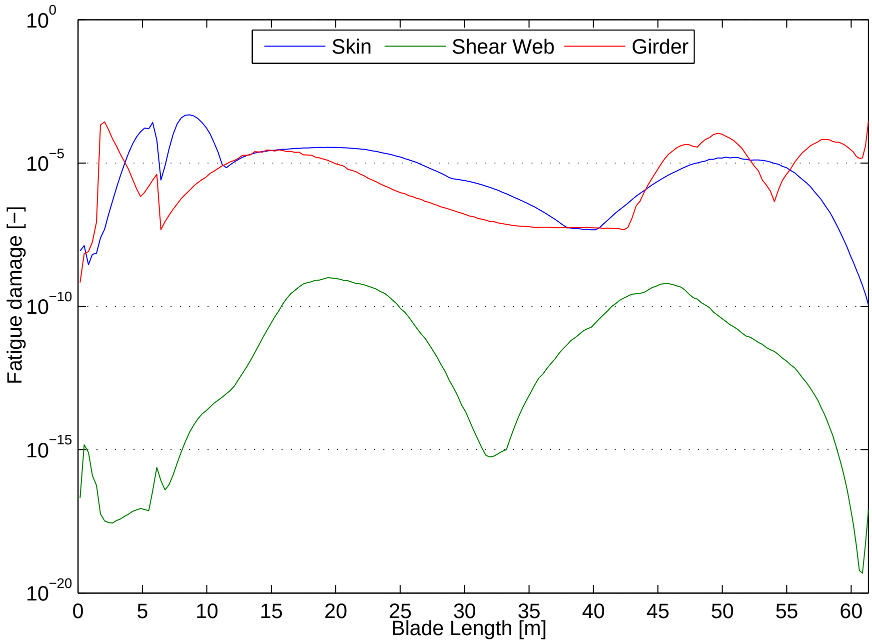

Figure 6.6: Fatigue damage along the blade for the US-TD-FA load case of the conventional blade

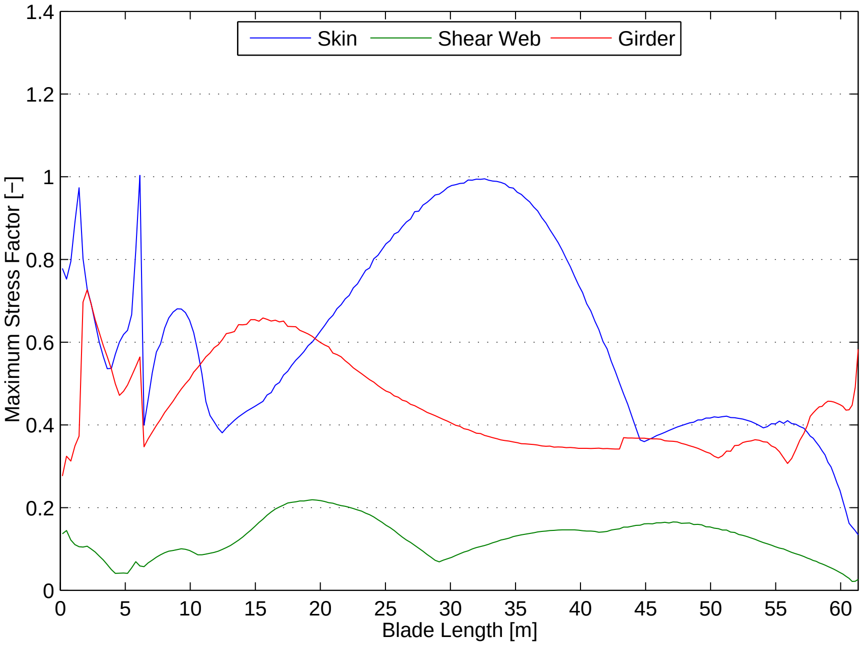

Figure 6.7: Maximum stress factor along the blade for the US-TD-FA load case of the conventional blade at 0° azimuth

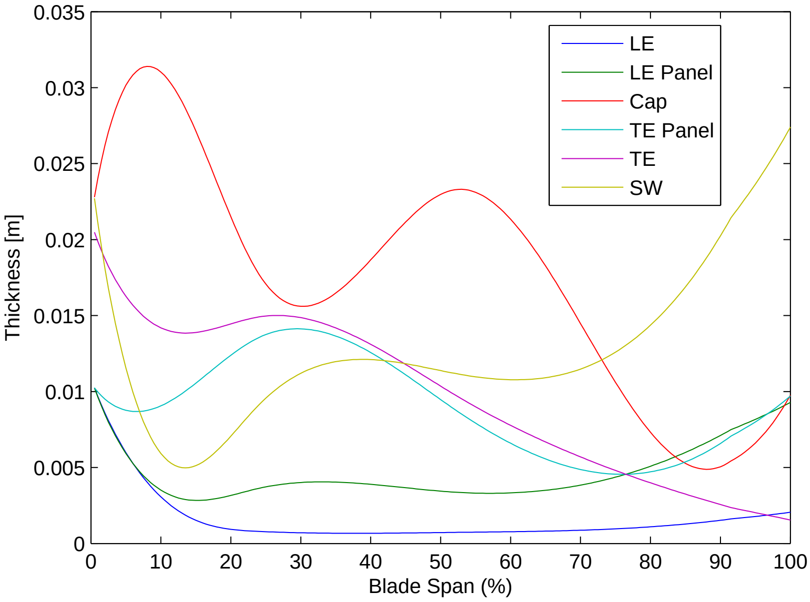

Figure 6.8: Thickness distribution for the US-TD-FA load case of the conventional blade

US-BU-TD-FA

As it is shown in Figure 6.9, the optimization ended faster than the UL-TD-FA case. The final design resulted to a heavier blade with an objective function equal with 0.654 which is translated to a blade's mass equal to 11.598 tn. The reason for this change is due to the addition of the buckling constraint which is the limiting factor of the optimization.

The minimum buckling load factor of the optimized design was equal to 0.998 and was observed at 0° azimuth. This buckling load factor value indicates a marginal failure of the blade. The first buckling mode of this azimuth position and its eigenvectors can be seen in Figure 6.12. This local buckling is observed at around 10% of the span on the trailing edge skin panels. Nonetheless, as previously mentioned in chapter 5, buckling calculations require a denser mesh but due to convergence time limitations this was not possible. The blade showed a first buckling mode load factor equal to 0.4 when analyzed with a fine mesh. This value does not match the 25% difference in the buckling load factor that appeared in the mesh convergence testing explained in Figure 5.7. Nevertheless, the buckling load factor has still converged at 30,000 elements. This difference probably occurs due to the fact that the difference in the buckling factor with a varying number of elements does not follow an analogue relationship. However, if the thickness of the spar cap was increased by 30%, the problem was resolved. Conceptual optimizations were examined that included extra buckling safety factors ranging from 0.25-0.4 to account for buckling convergence, although the final design still showed buckling failure when analyzed with a dense mesh.

The maximum MSF value (Figure 6.10) was 0.4259 and was found similarly to the initial design on the skin panels at around 10% of the span, while the maximum fatigue damage (Figure 6.11) had a value equal to $3.83e^{-8}$ and is met at the girder again at approximately 7% of the span. The tip deflection was reduced to 0.4822 of the allowable.

In Figure 6.13, the thickness distribution of the optimized blade can be seen. The thicknesses of the leading edge, trailing edge, trailing edge panel and leading edge panel were reduced by approximately 40% instead of 80% of the previous optimization scenario. The thickness of the spar cap, shear web and leading edge panel showed a different distribution compared to the initial design. In fact, the shear web and the leading edge panel showed an increasing trend towards the tip. A local reinforcement on the spar cap and the skin panels is recommended at the sections close the root to increase local stiffness and decrease buckling.

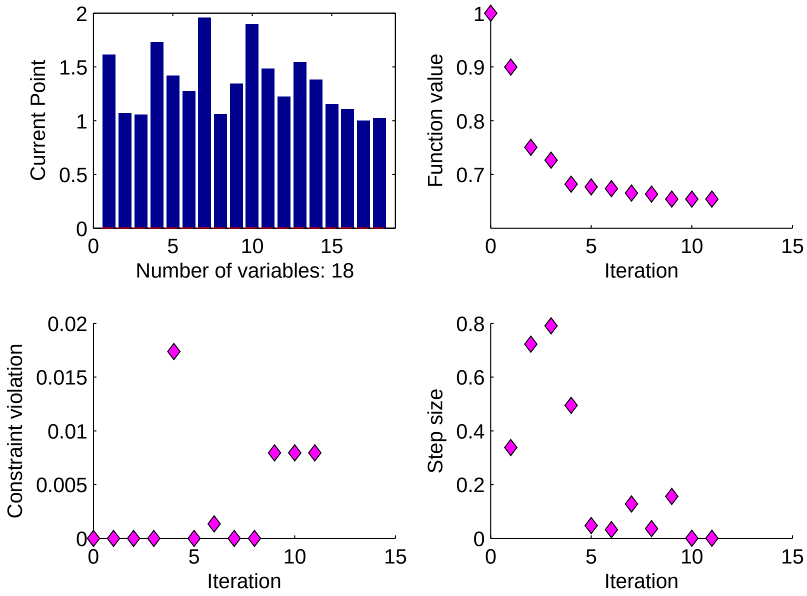

Figure 6.9: Optimization plots for the US-BU-TD-FA load case of the conventional blade

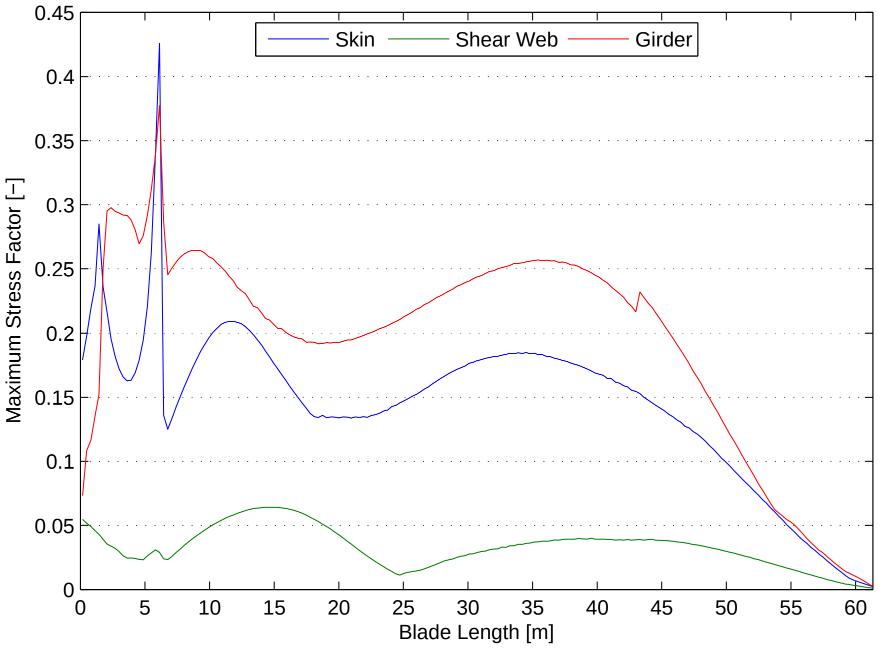

Figure 6.10: Maximum stress factor along the blade for the US-BU-TD-FA load case of the conventional blade

Figure 6.11: Fatigue damage along the blade for the US-BU-TD-FA load case of the conventional blade

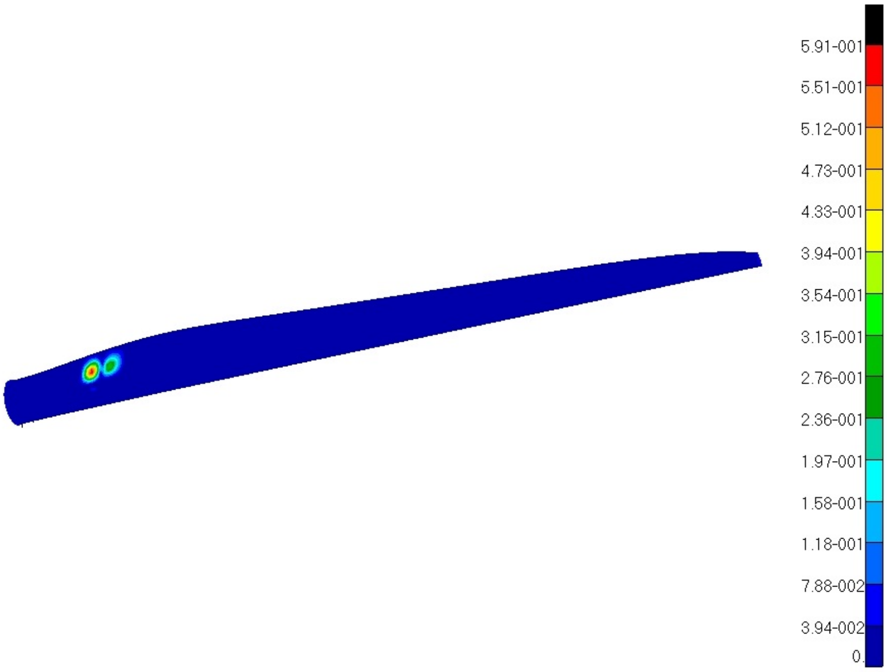

Figure 6.12: First buckling mode for the US-BU-TD-FA load case of the conventional blade

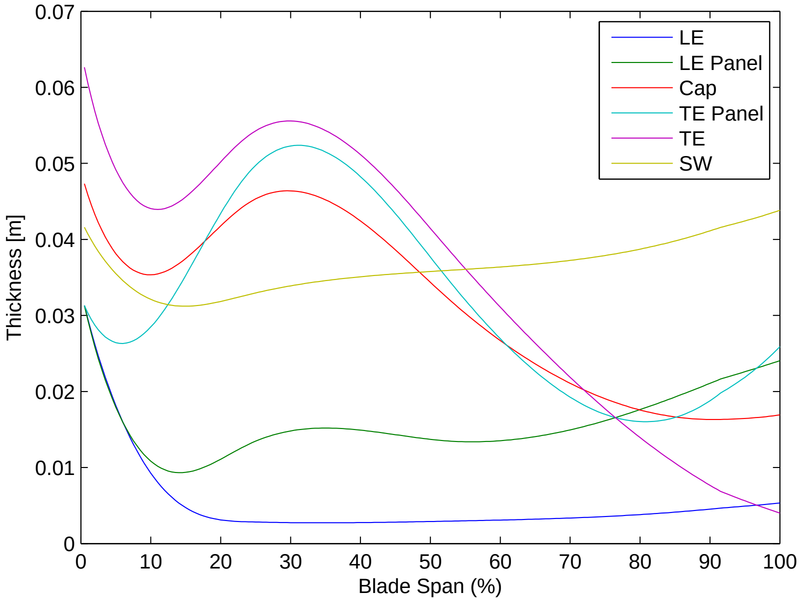

Figure 6.13: Normalized buckling length for the US-BU-TD-FA load case of the conventional blade

6.1.3 Comparison of Conventional Blade Case Studies

At Figure 6.14 a comparison of the thickness distributions for each section is made between the initial design and the two optimization scenarios. The following observations can be made:

- The girder was the section that showed the less thickness reduction which is reasonable since the girder is the largest contributor on flapwise and local stiffness.
- There is a trend to have a uniform thickness distribution of the trailing edge, trailing edge panel, leading edge and leading edge panel along the span in the optimization without buckling included. Without buckling these components do not need to provide any variation on the local stiffness therefore they remain fairly constant along the span. The same components at the optimization including buckling follow a downscale trend of the initial design.
- The thickness of the shear webs generally decreased in both cases, however they showed an increasing trend from 15% and towards the tip at both optimized designs. The skin shells and the shear webs are the main carriers of shear loads. The great reduction of the skin shells thicknesses leads to an increase of the shear web thickness towards the tip, where the aerodynamic loads are larger, in order to account for the loss of shear strength because of the skin shells thickness reduction.
- At both scenarios, stiffening of the blade is essential. At the scenario without buckling the optimized blade marginally fails under ultimate stress, therefore an increase in the blade's skin panels close to the root is recommended. At the scenario that includes buckling, the blade marginally fails under buckling, therefore an increase of the local stiffness is recommended close to the root either by increasing the thickness of the panels or by increasing the girder's thickness.

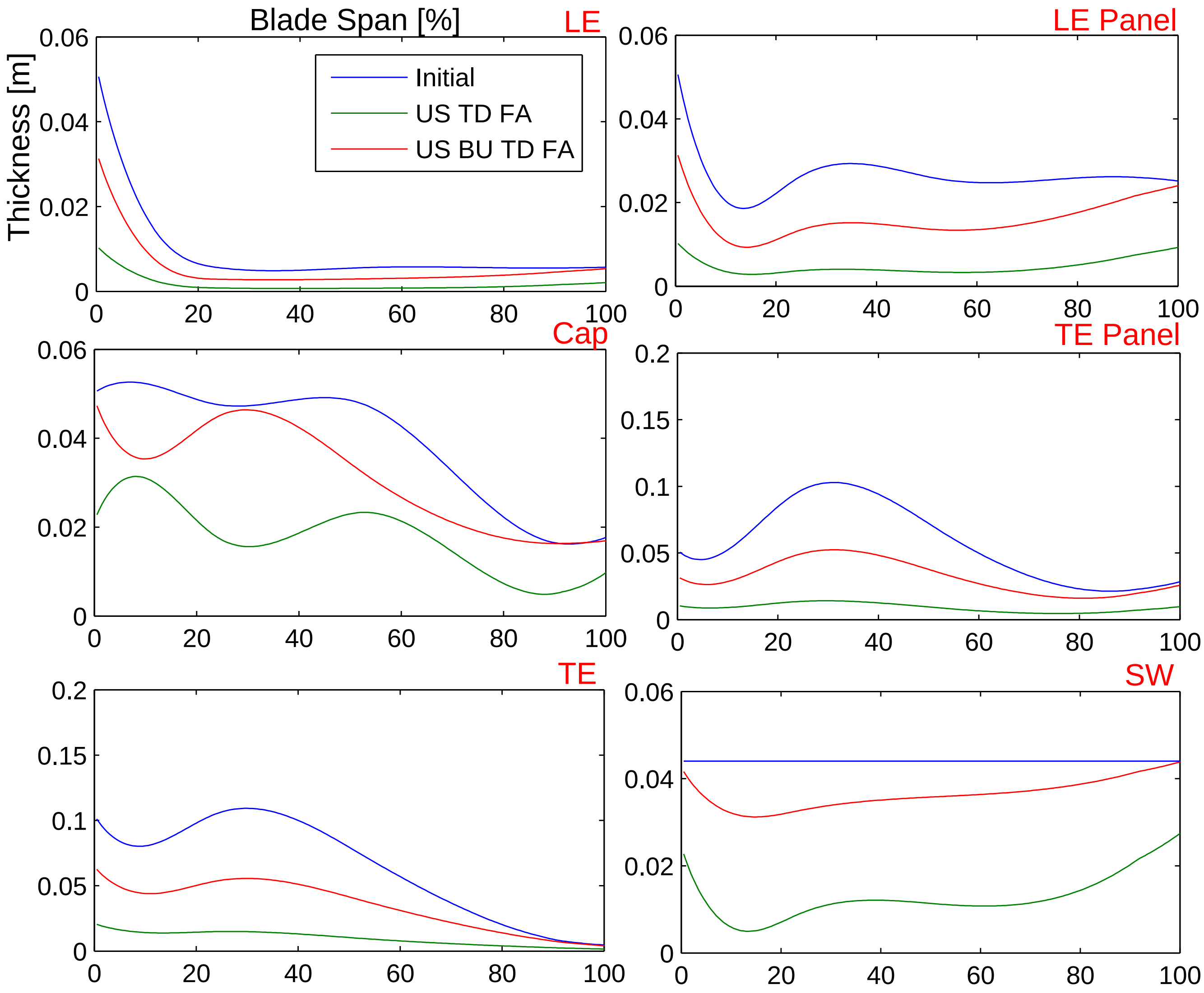

Figure 6.14: Thickness comparison between the optimized design and the initial for the conventional blade

6.2 Smart Rotor Blade (SR)

6.2.1 Initial Design

At the initial design of the smart rotor the only parameter that was altered was the aerodynamic loading on the blade as described in chapter 4 and chapter 5. The minimum buckling load factor was the same as the conventional design since it appeared at the rotor positions 90 ° and 270° where no flaps were used. However, the MSF and the fatigue damage were altered because of the change on the bending moments. In Figure 6.15 the difference in MSF is shown for the skin, the shear web and the girder at the span positions were the maximum MSF appears.

Nevertheless, the introduction of TRF altered significantly the load distribution on the blade. A comparison of the flapwise moments at the root can be seen in Table 5.9. The use of TRF led to a reduction of the loads on the critical points closer to the root but increased significantly the loads closer to the tip. Nevertheless, the MSF and fatigue damage close to the tip appeared still lower compared to the root values. A **2% decrease** in the maximum **MSF** was noticed from the HAWT scenario. Similar to the conventional blade, the maximum MSF was noticed at the skin at 10% of the span. In figure Figure 6.16 the difference in the fatigue damage is shown for the skin, the shear web and the girder at the blade span where the maximum damage appears. Similar to the HAWT scenario, the maximum damage appeared at the girder at 10% of the span. A **16.5% decrease** of the maximum **fatigue damage** was noticed from the HAWT scenario. Moreover, the fatigue on the skin was decreased significantly compared to the conventional blade.

6.2.2 Optimized Design

US-TD-FA

The optimization results of this case study showed similar results with the corresponding study of the conventional blade. As shown in figure Figure 6.17 the optimization of the smart rotor blade ended at 30 iterations with an objective function value equal to 0.2489 which is translated into a blade's mass equal to 4.413tn. This means that the mass was 0.1tn lower compared to the respective optimization of the conventional blade. The maximum MSF factor was equal to 1.0036 (figure Figure 6.19), the tip deflection equal to 1 and the maximum fatigue damage equal to $4.69e^{-4}$ (figure Figure 6.18). Similar to the conventional blade optimization a local reinforcement of the blade's skin close to the root will reduce the maximum MSF value below the allowable limit.

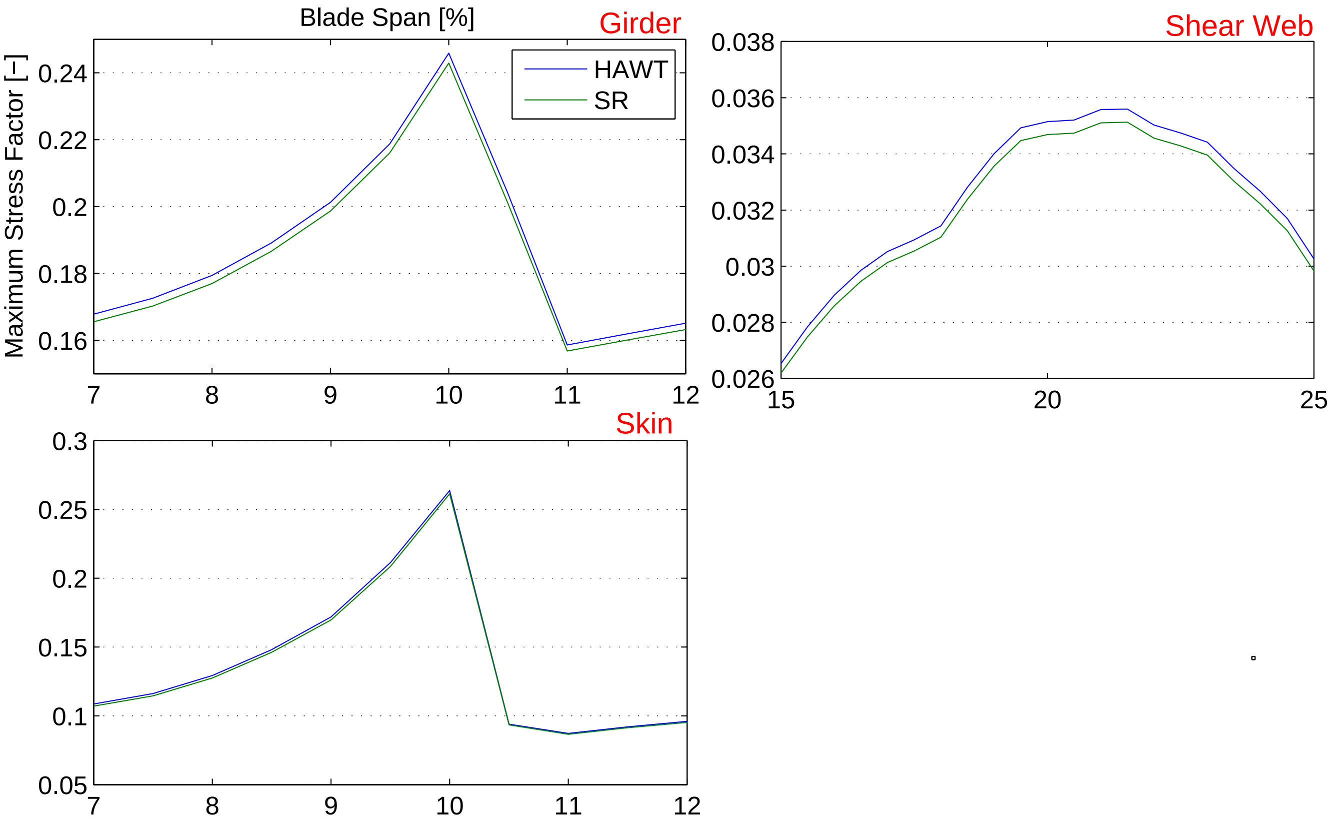

Figure 6.15: Comparison of maximum stress factor at the blade span where maximum appears

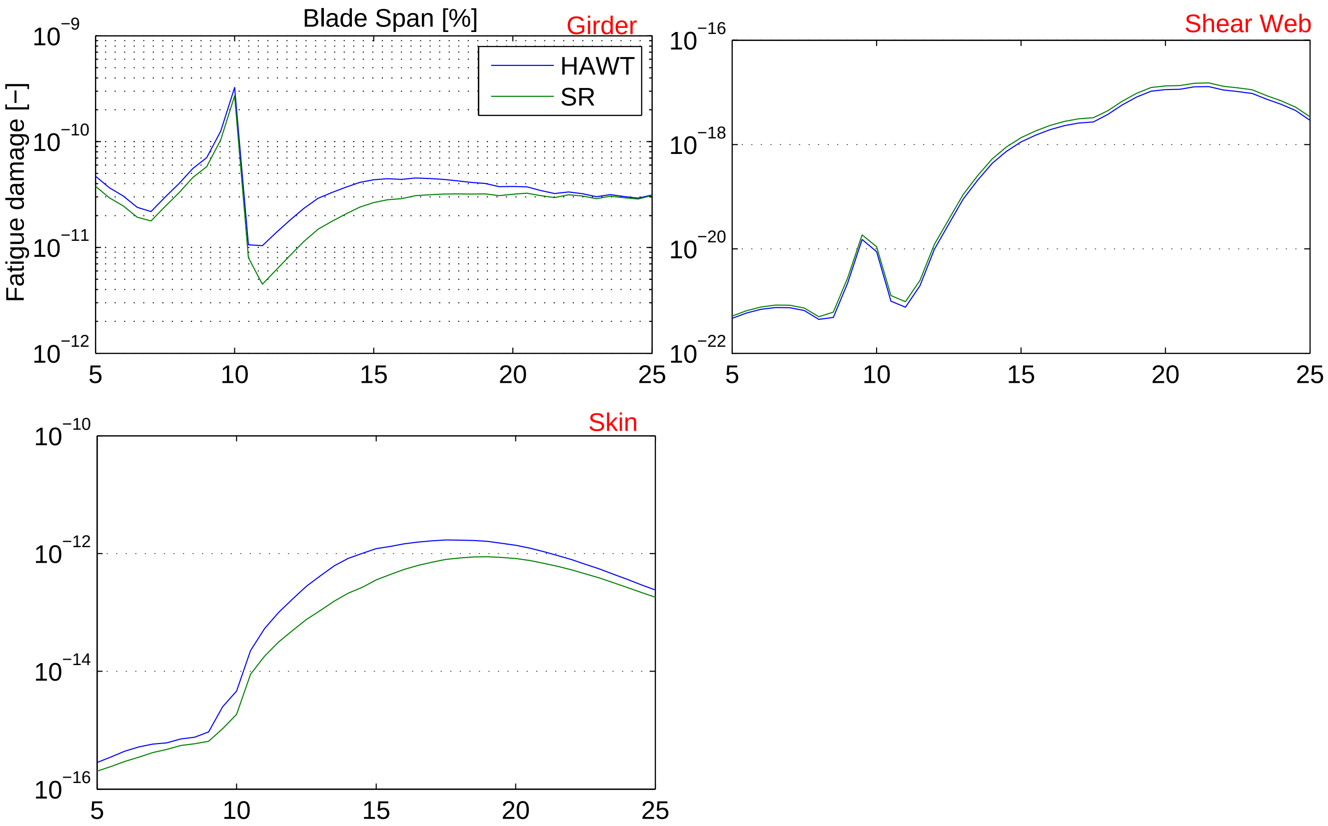

Figure 6.16: Comparison of fatigue damage at the blade span where maximum appears

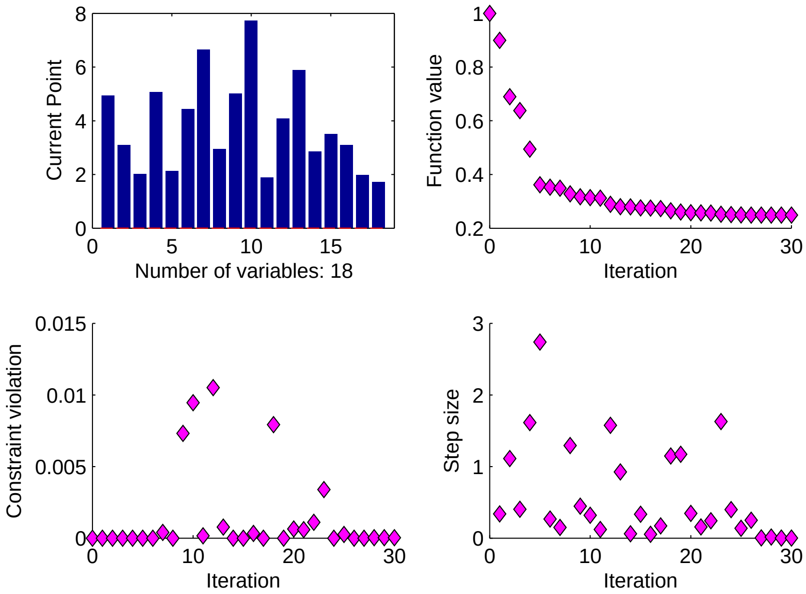

Figure 6.17: Optimization plots for the US-TD-FA load case of the smart rotor blade

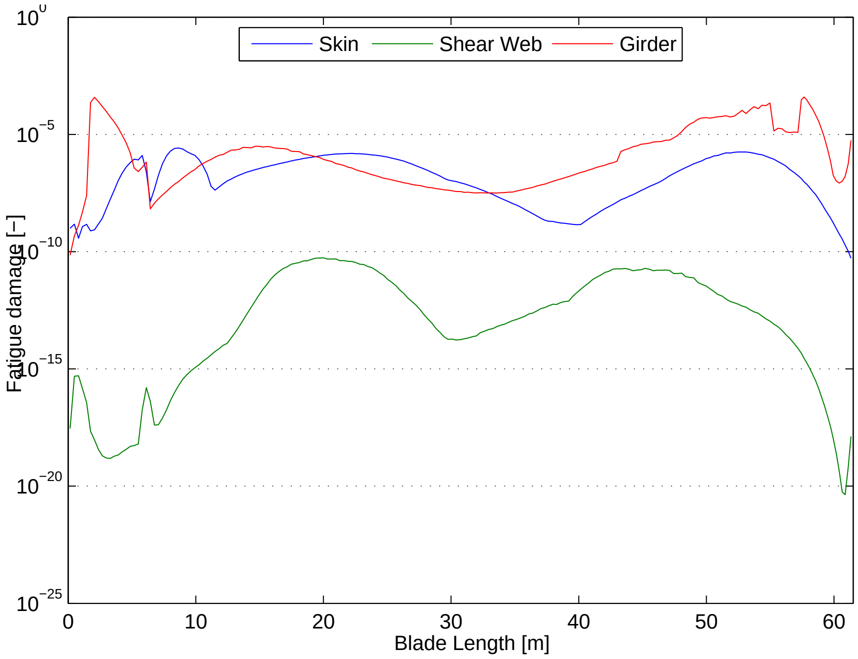

Figure 6.18: Fatigue damage along the blade for the US-TD-FA load case of the smart rotor blade

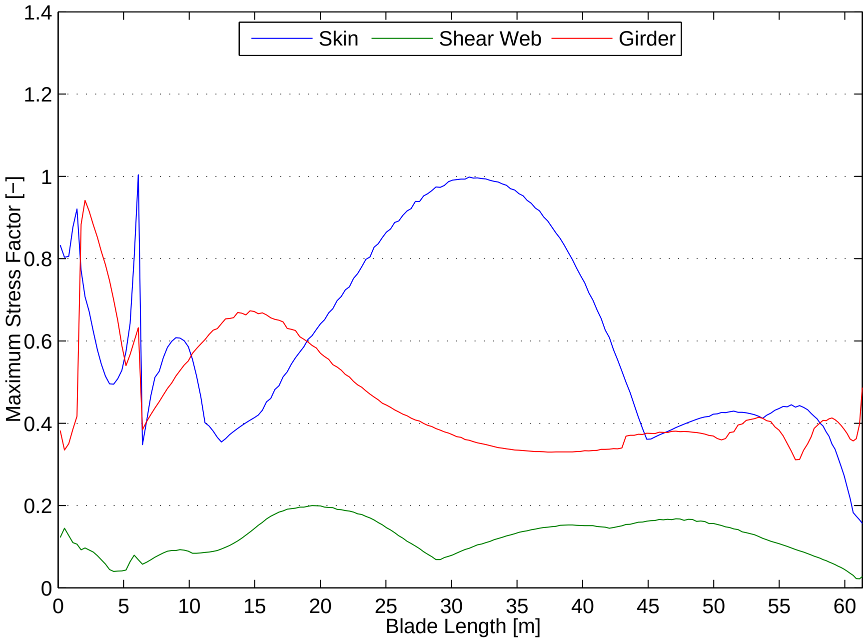

Figure 6.19: Maximum stress factor along the blade for the US-TD-FA load case of the smart rotor blade

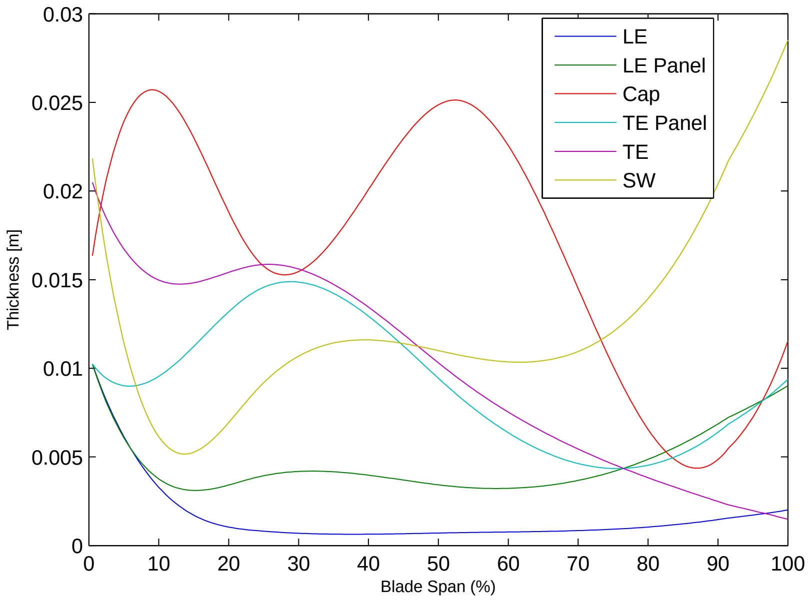

Figure 6.20: Thickness distribution for the US-TD-FA load case of the smart rotor blade

US-BU-TD-FA

In the US-BU-TD-FA optimization of the smart rotor an optimization error occurred at the optimizer. Probably due to the addition of the buckling constraint, at the 5th iteration the gradient became zero which led fmincon to crash. Actually, a further sensitivity analysis on the optimization inputs is required in order to solve this issues. Nevertheless, due to time limitations a different solution was chosen. Instead of trial and error on the optimization parameters, the is also the option to execute a new optimization with a new starting point the final point of the previous optimization. Therefore, a second optimization was executed as shown in Figure 6.22.

The failure criteria results were similar to those of the corresponding optimization of the conventional blade. The final objective function value was equal to 0.6323 which is translated to a mass equal to 11.137 tn which is 2.5% less than the conventional blade. The maximum MSF (Figure 6.23) was equal to 0.4198, the tip deflection was equal to 0.5138 of the maximum allowable deflection and the maximum fatigue damage equal to $3.41e^{-8}$. The thickness distribution of the optimized design is presented in Figure 6.26. The smallest buckling eigenvalue was equal to 0.98 and is located at the leading edge skin panel close to the root. Similar comments as those described in subsection 6.1.3 regarding the two optimization runs can be made.

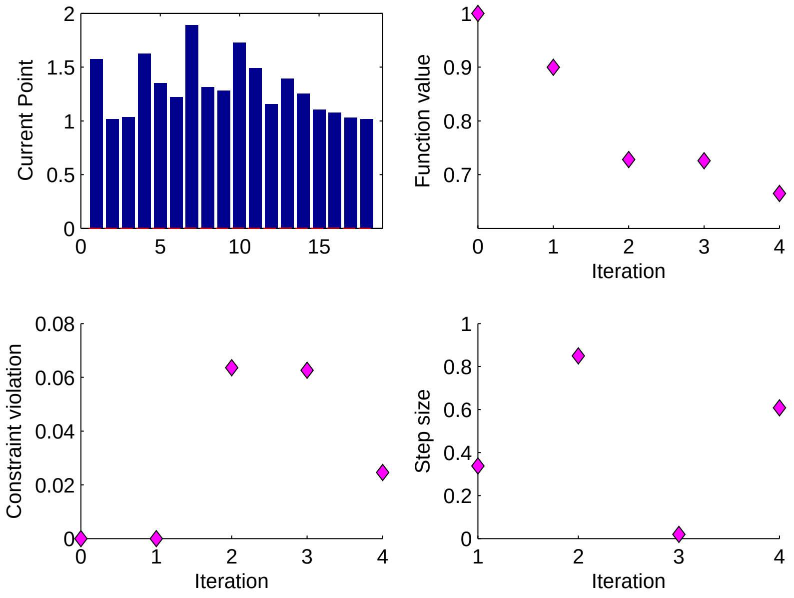

Figure 6.21: Optimization plots for the US-BU-TD-FA load case of the conventional blade

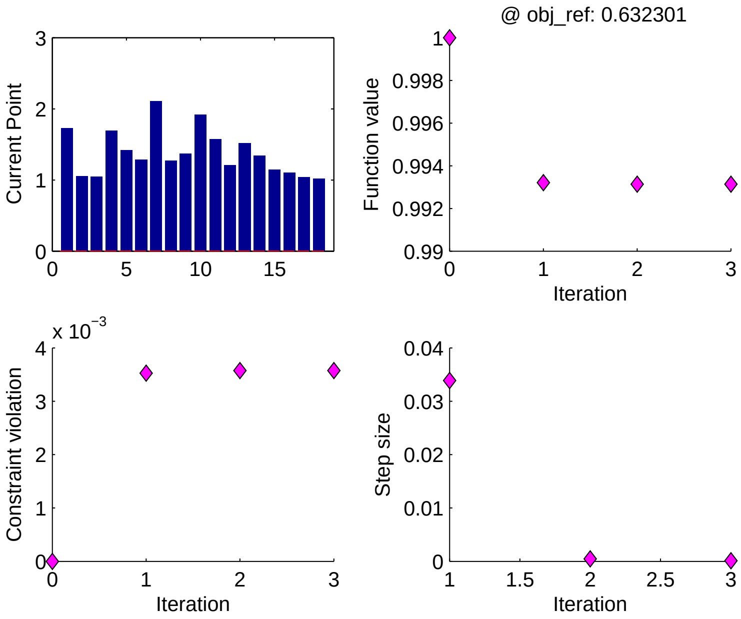

Figure 6.22: Optimization plots for the US-BU-TD-FA load case of the conventional blade

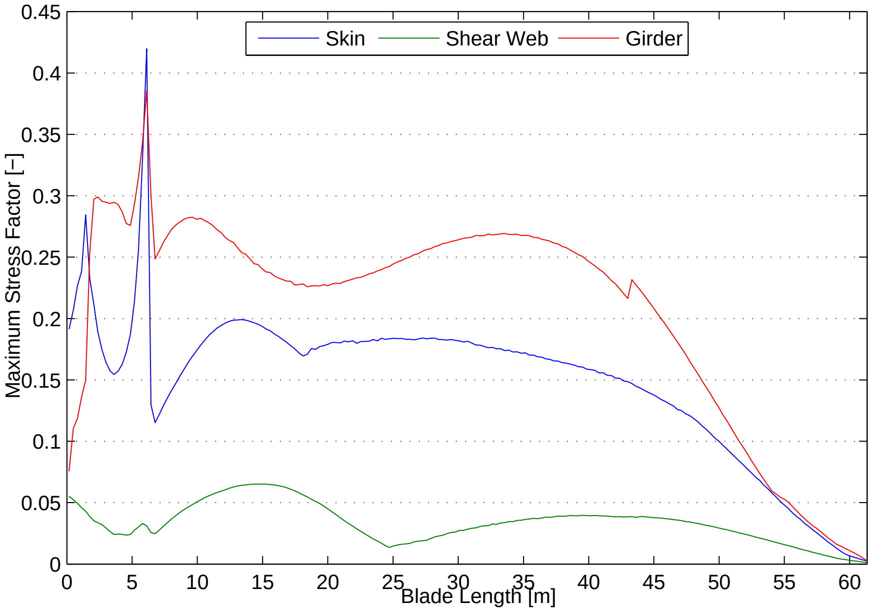

Figure 6.23: Maximum stress factor along the blade for the US-BU-TD-FA load case of the smart rotor blade

Figure 6.24: Fatigue damage along the blade for the US-BU-TD-FA load case of the smart rotor blade

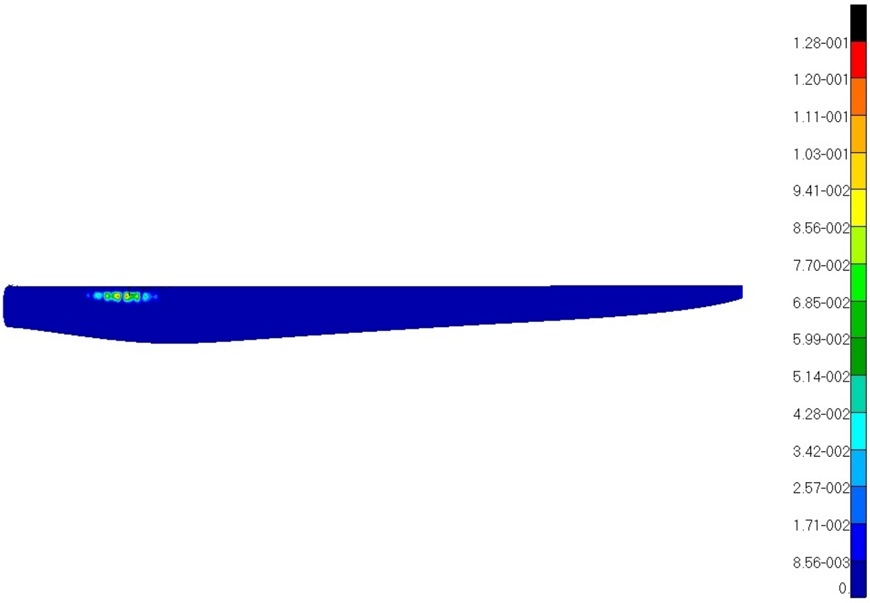

Figure 6.25: First buckling mode for the US-BU-TD-FA load case of the smart rotor blade

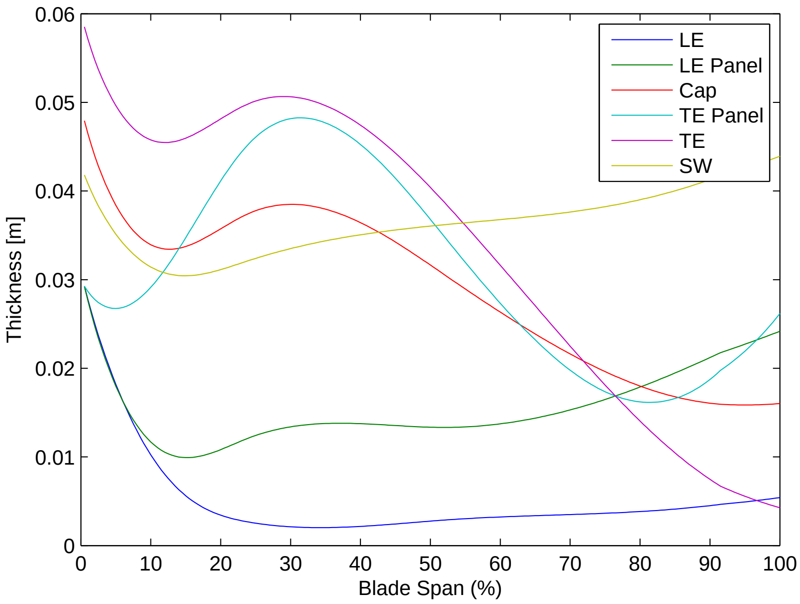

Figure 6.26: Thickness distribution for the US-BU-TD-FA load case of the smart rotor blade

6.3 Comparison of Conventional and Smart Rotor Blades

At Table 6.2, a comparison of the failure criteria for each case study examined is presented along withe the corresponding mass.

Cases	Max MSF(-)	Max TD(-)	Min Buckling(-)	Max MR(-)	Mass(tn)
Initial Design HAWT	0.2637	0.3502	2.4104	3.24e^{-10}	17.734
Initial Design SR	0.2582	0.3379	2.4104	2.71e^{-10}	17.734
US TD FA	1.0035	0.9839	-	4.82e^{-4}	4.519
SR US TD FA	1.0036	1	-	4.69e^{-4}	4.413
US BU TD FA	0.4259	0.4822	0.99	3.83e^{-8}	11.598
SR US BU TD FA	0.4198	0.5138	0.98	3.41e^{-8}	11.137

Table 6.2: Summary of results of each case study

The implementation of trailing edge flaps on the blade led to a 2% decrease of the maximum stress factor and 16.5% of the maximum fatigue damage. Thus, the smart rotor optimizations showed a 0.5% further mass reduction in the scenario without buckling and 2.5% in the scenario with buckling included. The minimum buckling load factor shifted from the 45° azimuth position to 0° azimuth position at both optimizations. Furthermore, buckling appeared to drive the optimization; however, at the optimizations without buckling ultimate stress and tip deflection appeared to be the limiting factors.

As it can be seen in Table 6.3 the MSF appeared in all cases at skin panels close to the root. The buckling load factor on the other hand appeared at skin panels close to the trailing edge at the same spanwise location but in a different form in the conventional and the smart rotor optimization scenarios. Compared to the initial design, local buckling shifted closer to the root in the two optimization designs. The maximum fatigue damage was met at the girder at all cases except the optimization scenario without buckling of the conventional blade where it was found at the skin. Nevertheless, at the initial and optimized designs of the conventional design, the skin fatigue damage was significantly closer to the girder fatigue damage compared to the smart rotor design. More precisely, the fatigue damage on the skin might not be the highest but it was significantly reduced with the introduction of TRF.

Cases	MSF	Buckling Factor	Fatigue Damage
Initial Design	skin (∼10%)	skin/girder (∼10-35%)	girder (∼7%)
US TD FA	skin (∼10%)	-	skin (∼10%)
SR US TD FA	skin (∼10%)	-	girder (∼7%)
US BU TD FA	skin (∼10%)	skin(∼5-10%)	girder (∼7%)
SR US BU TD FA	skin (∼10%)	skin(∼5-10%)	girder (∼7%)

Table 6.3: Location of maximum of each failure criterion for each case study

The main difference in mass reduction between the two blade designs can be understood from Figure 6.27. The girder thickness of the smart rotor blade was further reduced in the optimization including buckling. The main differences can be observed between 20% and 40% of the span. As mentioned in the previous sections, local reinforcement at the skin panels and the girder close to the root is recommended.

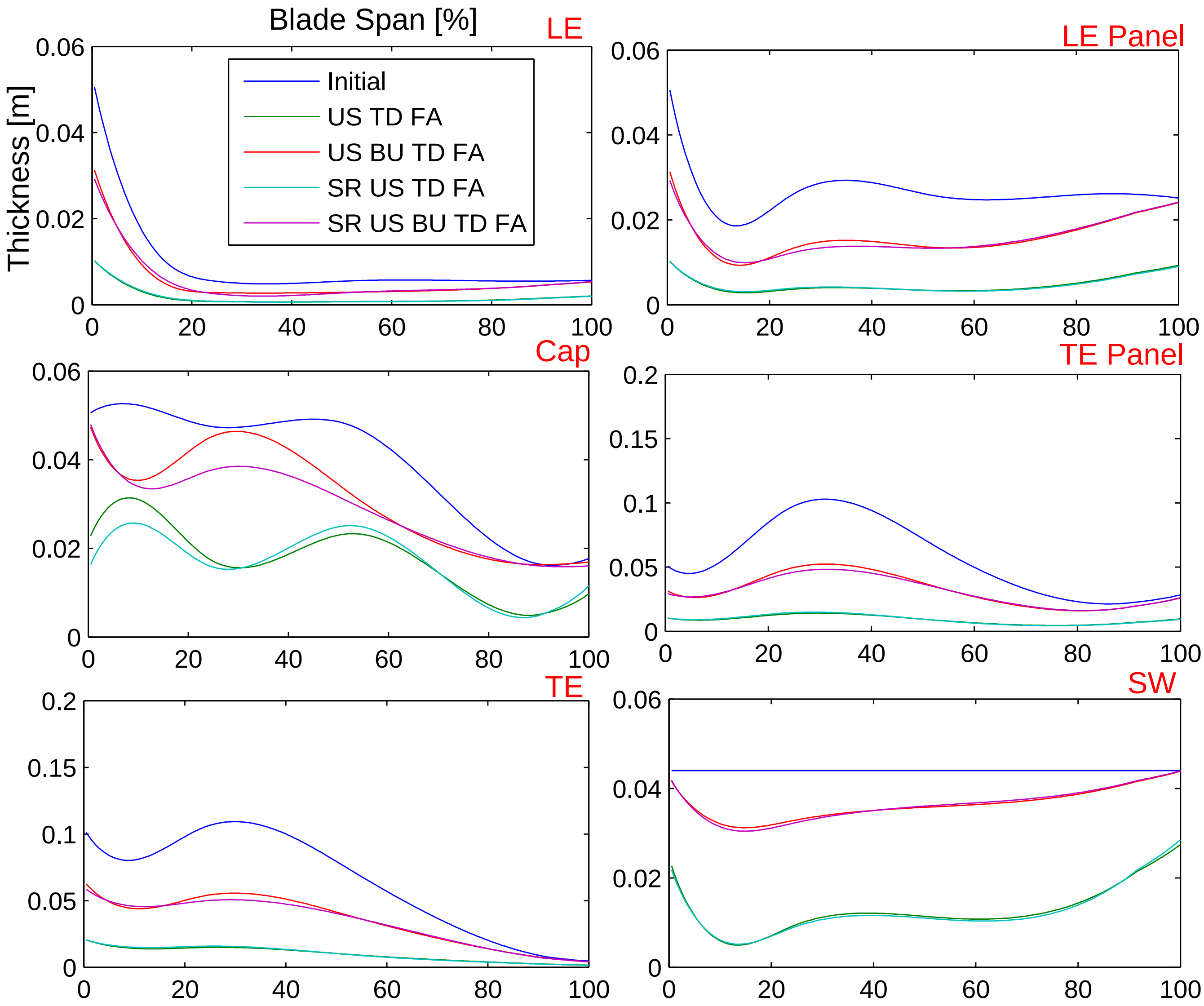

Figure 6.27: Thickness comparison

Chapter 7

Conclusions and Recommendations

7.1 Discussion on the Methodology

Summarizing the scope of this project, its main goals can be regarded as the following:

1. To alter and extend the capabilities of an existing MATLAB tool in order to accurately design a Horizontal Axis Wind Turbine (HAWT) blade and mesh it in a flexible way with a limited amount of variables.
2. To modify a coupled algorithm for the structural analysis of the HAWT blade using Finite Element Analysis (FEA).
3. To further develop a post processing algorithm of the FEA results.
4. To adjust an optimization algorithm for the minimization of the blade's weight and provide also the option to analyze a HAWT blade equipped with trailing edge flaps (TRF).
5. To create a conventional HAWT blade based on the SANDIA 5MW blade and a smart rotor design and compare them in order to investigate the load reduction capabilities of smart rotors.

The logic of the algorithm developed can be divided into a set of sub-processes. A detailed tree of the subscripts is presented in Appendix C. The most significant main sub-processes of the algorithm are listed below in the corresponding row:

1. The blade's geometry, materials and mesh are defined.
2. The blade design is translated to a FEA input.
3. The FEA solver (MSC Nastran) is called and the blade is analyzed (linear static, buckling or modal analysis).

4. The results are post processed and translated into structural constraints (ultimate stress, fatigue, deflection and buckling).
5. A multidisciplinary design optimization algorithm (fmincon) is used the minimization of the blade's weight by altering the element thicknesses locally.

The blade design can be divided into three main stages: 1) geometry creation and meshing of the blade, 2) generation and application of the materials and 3) generation and application of the loads on the blade. The geometry can be accurately represented using Non-Uniform Rational Basis Splines (NURBS). The use of NURBS offers great flexibility for the creation of the blade's curvature with a limited amount of parameters. The main geometry variables can be limited to airfoil, twist and chord at various points along the span. Moreover, through the use of NURBS an easier discretization/meshing of the blade can be achieved.

The material algorithm that was developed offers a high flexibility in the selection and application of materials at various blade location with also a limited amount of input parameters. This algorithm uses as input the properties of the ply materials, the sequence of plies on each stack and the positioning of each stack along the span and the chord. Using classical lamination theory (CLT) the stiffness matrix of each stack is computed and used as input in MSC NASTRAN. Furthermore, the Tsai Hill criterion is used in order to determine the maximum allowable stresses of each element.

An aerodynamic loading algorithm is used in order to calculate the pressure force on each node. Using BEM theory, the angle of attack (AOA) and Reynolds number (Re) are computed at each specified spanwise and azimuth position. Having known the AOA and Re, the pressure distribution for the various airfoils at different spanwise locations is generated using the software XFOIL and post processed in Matlab in order to apply a single pressure vector on each node. The loading algorithm requires a minimum amount of parameters (wind speed, rotor rotational speed, wind shear parameters, number and location of each aerodynamic section); however, the generation of the pressure distribution files in XFOIL can be fairly time consuming.

The blade is analyzed using the FEA numerical technigue. Compared to other structural analysis methods, the subdivision of the structure into smaller parts offers more accurate geometry and material representation, higher accuracy and better capture of the local effects. Nevertheless, these positive attributes come at the cost of higher simulation time. Furthermore, an analysis on the number of elements was conducted. The aim of this analysis was to find a balance between simulation time and accuracy of the results. Ultimate stress, strains, mass and deflection results did not show any significant variation above 10.000 elements;however, in order to adequately analyze buckling a fine mesh is required ($\geq$30.000 elements). Nonetheless, a fine mesh would lead to long computational time. By using 10.000 elements the convergence time of the optimization ranged from 3 to 5 days using 4 parallel processors. A sensitivity analysis of the optimization inputs had to be conducted due to the fact that occasionally the optimization got stuck at a bad minimum after several iterations. Assuming that 30.000 elements were used instead of 10.000, this would lead to a 60% higher simulation time which would also make the sensitivity analysis more problematic.

The performance of the geometry and material algorithm was validated by comparing the structural characteristics (mass, stiffness, chord, twist and moment of inertia distributions) of the initial design with those obtained from the SANDIA report. Of course, minor deviations were expected due to the completely different methodology that was followed compared to SANDIA and surely there would still be room for several improvements on those algorithms. Moreover, a modal analysis of the blade was conducted using the FEA solver and the first six mode frequencies were found to be almost identical with those obtained from the SANDIA report. Furthermore, the performance of the aerodynamic loading algorithm was partly validated since the tip deflection and the bending moments matched those of a SANDIA model that was developed and simulated in DNV GL Bladed. There was no actual validation of the FEM output post processing algorithm for all criteria. However, in order for the deflection to be valid, the output of MSC Nastran and the material/geometry inputs to MSC Nastran should be valid. Since the deflection results are related to the strain results and the stiffness is also validated, it is logical to have obtained valid ultimate stress results due to the direct relationship between those quantities. This is an indication that the algorithm that calls SOL 101, executes MSC Nastran and post processes the SOL 101 results operates finely under the examined load case. Nevertheless, there was no direct way to validate the fatigue and buckling calculation sections of the algorithm.

In order to analyze fatigue, several numbers of azimuth positions were examined in order to ensure an adequate stress sampling. Nonetheless, a number of azimuths lower than 16 showed great difference in the fatigue results compared to 32 azimuth positions. This means that fatigue calculations increase the simulation time greatly since 16 linear static analyses have to be executed for each evaluation of the design vector.

The conventional and smart rotor blade design were analyzed for ultimate stress, deflection, fatigue and buckling for normal operation of the turbine at rated wind speed without taking into account any turbulence or dynamic phenomena. The skin, girder and shear web thicknesses for six spanwise sections were used as the optimization design vector. The algorithm developed offers the ability to include boundaries on the design vector, linear or non-linear equality and inequality constraints; however, only non-linear inequality constraints were applied. Depending on the type of analysis, the FEA results were post processed to inequality constraints. The conventional and smart rotor blades were optimized for two set of constraints: 1)ultimate stress, fatigue and deflection constraints (UL-TD-FA) and 2) ultimate stress, buckling, fatigue and deflection constraints (UL-BU-TD-FA).

7.2 Conclusions

As described at the previous section, a set of goals was determined in the context of this thesis project. Regarding the first goal that was described in section 7.1, the algorithm was developed to provide the ability for a flexible, more comprehensive and more accurate modeling of the shape and materials of a HAWT blade with a limited amount of variables. Several design and programming obstacles were encountered during this procedure. The tool that was developed by Schelbergen [25] dealt with the upscaling of vertical axis wind turbines (VAWT) and not with the accurate representation of a VAWT blade. This means that the blade was far from a realistic structure which led to a redevelopment of the majority of the blade design and load design algorithms. The most significant additions in order to accomplish this goal are presented below.

- *From VAWT to HAWT*
  The first challenge concerned the fact that the basis algorithm was developed for analyzing VAWT.
- *Geometry*
  Important additions were made in the geometry algorithm and a blade with multiple airfoils and more complex geometry can be created. Due to the reduction of the chord and the difference in the airfoil shape along the span, the elements sizes differ greatly, so in order to have a more homogeneous mesh the spanwise and chordwise discretization techniques were also altered.
- *Materials*
  The previous algorithms were significantly enhanced in order to have the ability to add multiple materials in a stack, create numerous stacks, discretize the blade in a flexible way and assign the different stacks at spanwise or chordwise any location.
- *Aerodynamic Loading*
  The previous BEM code was enhanced in order to account for varying aerodynamic loading along the span and more parameters were included. A decoupled algorithm was used to create an airfoil geometry with a deformed trailing edge and calculate its Re and AOA. This makes the implementation of a smart rotor uncomplicated since the difference between the conventional and the smart rotor blade resides only in the aerodynamic pressure distribution.

Concerning the second goal that was set, as described in chapter 4 the FEM input file processing tool was adjusted to the new blade design features after a demanding debugging process. The same applies for the third and fourth goal that concerned the post processing of the FEM results and optimization of the blade's thickness. A separate coupled structural properties calculation algorithm was also developed with different methodology compared to that designed by Roscher [24]. It is worth mentioning that all design inputs and analysis options (in forms of switches) have been included into one single script in order to provide a flexibility at the simulations. Additionally, an option to include tip deflection as a constraint was added to the tool. Furthermore, a mode shape constraint option was also introduced which provides the ability to alter the blade's thicknesses in such a way that resonance can be avoided. Through the modifications and the adjustment on the FEM input algorithm, FEM output processing algorithm and fmincon, a HAWT blade can be structurally analyzed and its weight can be minimized for a specific load case without the occurrence of structural failure.

Regarding the smart rotor case study, after comparison of the effect of the TRF on flapwise bending moment for various flap angles, a ± 2° flap was selected and placed at 90-100% of the chord and 78-98% of the span. The application of TRF on the blade at 0° and 180° azimuth positions decreased the maximum ultimate loads by 2% and the maximum fatigue loads by 16.5%. The optimized conventional blade resulted to a reduced mass from 17.76tn to 4.52tn at the UL-TD-FA scenario and to 11.6tn at the UL-BU-TD-FA scenario. The optimized smart rotor blade had a final mass 2.3 % lower than the conventional blade at the UL-TD-FA scenario and 3.97% at the UL-BU-TD-FA scenario.

Since the optimization stopping criterion required a slight surpass of the limiting constraint, local reinforcement is needed at all cases at the skin panels and at the girder close to the root. In that way, the strength at the location where maximum stress occurs will be increased and the local stiffness of the blade will be enhanced in order to prevent local buckling. It was noticed that the girder was the structural element that remain less unchanged due to its importance on the blade's local and global stiffness. Furthermore, since offshore wind turbine blades are usually long slender structures, they are buckling driven. In this research, buckling appeared to be the limiting factor of the optimizations. Moreover, the use of TRF led to a reduction of the loads to the critical points closer to the root but increased significantly the loads close to the tip.

The introduction of trailing edge flaps on a wind turbine blade is a subject under investigation by the research institutes and the industry. The tool developed offers a positive starting point for more complex geometrical design, structural analysis and optimization of smart rotors. Some of the most important recommendations for further development of this tool are presented at the following section.

7.3 Recommendations

The tool developed consisted of several a structural design algorithm coupled with a FEA solver and an optimization algorithm. The algorithms developed offer room for several improvements.

- *Shape optimization option.*
  The algorithm developed is not capable of optimizing the aerodynamic shape (airfoil shape, twist etc.) of a HAWT blade. Furthermore, the aerodynamic optimization can not be achieved without applying major changes at the algorithms. However, the blade could be scaled up or down during the optimization without major modifications. In fact, the algorithm already offers the option to include the radius as an optimization parameter but no full optimization including this option was executed. The chord vector input is normalized by the radius, so a variation of the radius will also result to a scaled chord distribution. Nevertheless, each section with an assigned airfoil does not understand the chord length and the airfoil height as two decoupled quantities. This means that the scaled chord distribution is actually a scale of the airfoil. In that case, the objective function will have to also include the area of the blade in order to relate the mass of the blade with the energy the rotor extracts.
- *Different methodology for altering the stacks thicknesses.*
  Regarding the analysis of the stiffness and stress properties of the stacks classical lamination theory was used and the thicknesses of the laminate and sandwich layups were altered by varying the thickness of the whole stack which is not of common practice in reality. A more realistic approach would allow the optimizer to evaluate layers and add or remove layers on the corresponding stacks. Concerning sandwich structures, the adjustment of the stack's foam thickness during the optimization is recommended. Moreover, it would be of interest to include a representative cost of each ply and include the cost of the whole blade in the objective function. Otherwise,

if the optimizer had the option to add or remove a specific ply, it is probable that the final design would result from mainly carbon plies which might not be the most cost effective solution. Additionally, the change of the ply angles during the optimization would be an even more complex addition.

- *More comprehensive aerodynamic loading.*
  Several dynamic phenomena were excluded from the BEM aerodynamic model that was used for the calculation of the aerodynamic loads on the blade. In order to realistically analyze a wind turbine blade, load cases from industry standards have to be analyzed. This means that models have to be included at the load generation algorithm to take into account turbulence and other parameters.
- *Analyze and combine more load cases.*
  The optimization that took place in this thesis concerned a blade under normal operation at rated wind speed. Of course, the optimized blade design has no physical meaning since it is the outcome of only one specific loading scenario. Thus, further load cases (extreme conditions, parked, braking etc.) have to be examined with different wind speeds and tip speed ratios and if possible develop the algorithm such that the optimization takes into account constraints created from multiple of load cases. This could be achieved through a loop process that develops multiple FEM inputs and post processes the FEA results of each load case. Afterwards, the worst case value for each element could be found among the load cases and calculate the optimization constraints. Furthermore, each load case could be separately simulated and compared with the model created in DNV GL Bladed to further validate the code.
- *Use a more realistic fatigue calculation technique for composite stacks.*
  Since every ply has a different S-N curve, the fatigue damage for each ply separately and not for the whole stack will have to be computed. Furthermore, other fatigue models for composite materials will have to be examined whether they can predict the fatigue damage more accurately.
- *Make use of the tool for structural analysis and optimization of other wind turbine components.*
  Due to NURBS, the algorithm developed could also offer easy representation and structural analysis of other wind turbine components such as the tower. In that case, the aerodynamic loads calculation algorithm would require significant alterations. Nonetheless, the simple implementation of a load due to wind shear and the rotor's thrust could be achieved with minor changes. with the use of the appropriate linear constraints or boundaries an optimized thickness distribution of the tower could be achieved. Besides ultimate stress, buckling and fatigue, the final design could also be optimized to avoid resonance.
- *Include the option to create a blade with a deformed TRF geometry.*
  In that way a more accurate representation of the influence of TRF can be obtained. The local structural behavior of the flaps and the nearby elements can be analyzed in that way and not only their impact on the blade's loading. Hence, various flap materials and geometries can be also tested for their structural performance.
- *Reduce computational time.*
  By replacing the FEM model with analytical models, it is believed that convergence of the optimization could be improved.

References

[1] Matlab constrained nonlinear optimization algorithms. `http://nl.mathworks.com/help/optim/ug/constrained-nonlinear-optimization-algorithms.html`.

[2] Matlab fmincon manual. `http://nl.mathworks.com/help/optim/ug/fmincon.html`.

[3] Lectures of design and manufacturing of wind turbine blades, 2014.

[4] P.B. Andersen. *Advanced Load Alleviation for Wind Turbines using Adaptive Trailing Edge Flaps: Sensoring and Control.* Ph.d. thesis, 2010.

[5] T. Ashuri. *Beyond Classical Upscaling: Integrated Aeroservoelastic Design and Optimization of Large Offshore Wind Turbines.* Ph.d. thesis, TU Delft, Delft, 2012.

[6] P. Baek. *Unsteady Flow Modeling and Experimental Verification of Active Flow Control Concepts for Wind Turbine Blades.* Ph.d. thesis, Technical University of Denmark, 2011.

[7] Christian Bak, Mac Gaunaa, Peter Bjørn Andersen, Thomas Buhl, Per Hansen, Kasper Clemmensen, and Rene Moeller. Wind tunnel test on wind turbine airfoil with adaptive trailing edge geometry. In *45th AIAA Aerospace Sciences Meeting and Exhibit*, page 1016, 2007.

[8] Thanasis K Barlas and GAM Van Kuik. Review of state of the art in smart rotor control research for wind turbines. *Progress in Aerospace Sciences*, 46(1):1–27, 2010.

[9] L. Bergami. *Adaptive Trailing Edge Flaps for active load alleviation in a Smart Rotor configuration.* Ph.d. thesis, Technical University of Denmark, 2013.

[10] L.O. Bernhammer, G.A.M. van Kuik, and R. De Breuker. Assesment of fatigue and extreme load reduction of fatigue and extreme load reduction of hawt using smart rotors. In *9th PhD Seminar on Wind Energy in Europe*, 2013.

[11] T. Buhl, C. Bak, M. Gaunaa, and P. B. Andersen. Load alleviation on wind turbine blades using variable airfoil geometry.

[12] Thomas Buhl, Mac Gaunaa, and Christian Bak. Potential load reduction using airfoils with variable trailing edge geometry. *Journal of Solar Energy Engineering*, 127(4):503–516, 2005.

[13] Tony Burton, David Sharpe, Nick Jenkins, and Ervin Bossanyi. *Wind energy handbook*. John Wiley & Sons, 2001.

[14] E.A. Ferede, M. Abdalla, and G.J.W. van Bussel. Nurbs-based parametric modelling of wind turbine blades. In *9th PhD Seminar on Wind Energy in Europe*, 2013.

[15] D Todd Griffith and Thomas D Ashwill. The sandia 100-meter all-glass baseline wind turbine blade: Snl100-00. *Sandia National Laboratories, Albuquerque, Report No. SAND2011-3779*, 2011.

[16] Jason Mark Jonkman, Sandy Butterfield, Walter Musial, and George Scott. *Definition of a 5-MW reference wind turbine for offshore system development*. National Renewable Energy Laboratory Golden, CO, 2009.

[17] HJT Kooijman, C Lindenburg, D Winkelaar, and EL van der Hooft. Dowec 6 mw pre-design. *Energy Research Center of the Netherlands (ECN)*, 2003.

[18] Matthew A Lackner and Gijs van Kuik. A comparison of smart rotor control approaches using trailing edge flaps and individual pitch control. *Wind Energy*, 13(2-3):117–134, 2010.

[19] Helen Markou, Peter Bjørn Andersen, and Gunner Chr Larsen. Potential load reductions on megawatt turbines exposed to wakes using individual-pitch wake compensator and trailing-edge flaps. *Wind Energy*, 14(7):841–857, 2011.

[20] MD/MSC Nastran. *Linear Static Analysis Users Guide*, 2010.

[21] MD/MSC Nastran. *Quick Reference Guide*, 2010.

[22] T. Phillipides. *Mechanics of Composite Materials.*

[23] Brian Ray Resor. Definition of a 5mw/61.5 m wind turbine blade reference model. *Albuquerque, New Mexico, USA, Sandia National Laboratories, SAND2013-2569 2013*, 2013.

[24] B. Roscher. Structural optimization of a vertical axis wind turbine with aeroelastic analysis. Msc thesis, TU Delft, 2014.

[25] M. Schelbergen. Structural optimization of multi-megawatt, offshore vertical axis wind turbine rotors. Msc thesis, TU Delft, 2013.

[26] Jeroen Smit, Lars O Bernhammer, Sachin T Navalkar, Leonardo Bergami, and Mac Gaunaa. Sizing and control of trailing edge flaps on a smart rotor for maximum power generation in low fatigue wind regimes. *Wind Energy*, 2015.

[27] IEC TC88-MT. Iec 61400-3: Wind turbines–part 1: Design requirements. *International Electrotechnical Commission, Geneva*, 2005.

[28] N. Troldborg. Computational study of the ris-b1-18 airfoil equipped with actively controlled trailing edge flaps. Msc thesis, 2004.

[29] Upwind. Design limits and solutions for very large wind turbines. Technical report, 2011.

[30] J.W. Van Wingerden, A.W. Hulskamp, T. Barlas, B. Marrant, G.A.M. Van Kuik, D.P. Molenaar, and M. Verhaegen. On the proof of concept of a smartwind turbine rotor blade for load alleviation. *Wind Energy*, 11(3):265–280, 2008.

Appendix A

Buckling Graphs

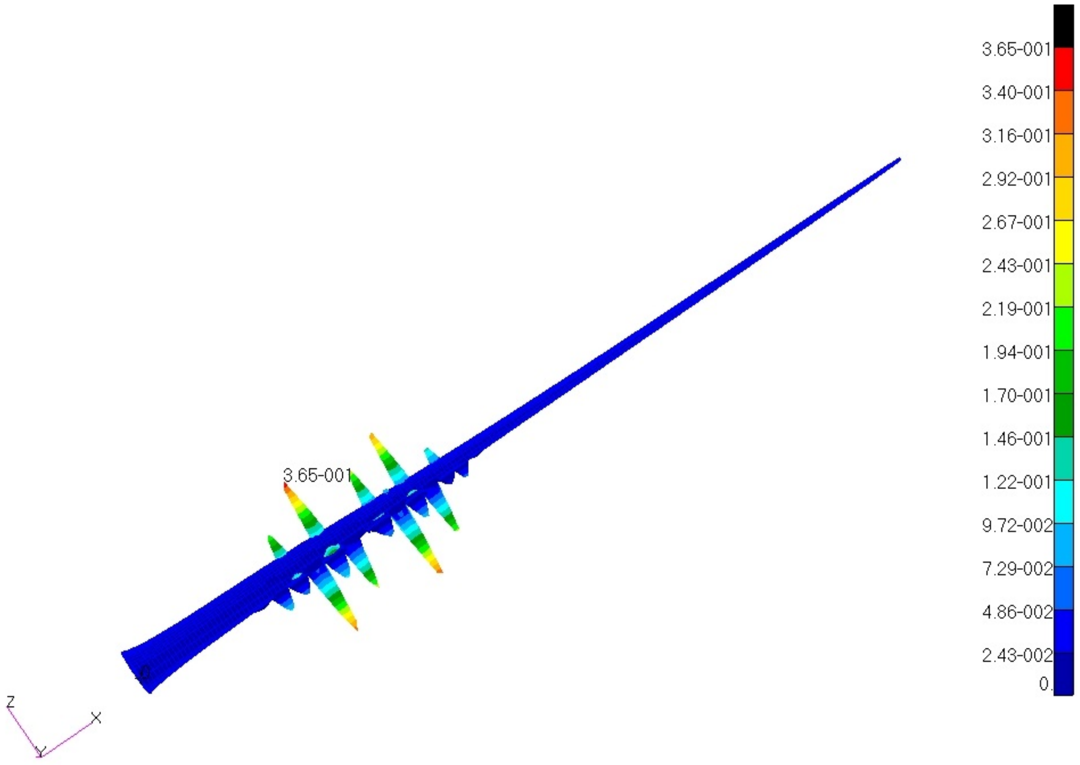

Figure A.1: Second figure of the first buckling mode for the initial design of the conventional blade

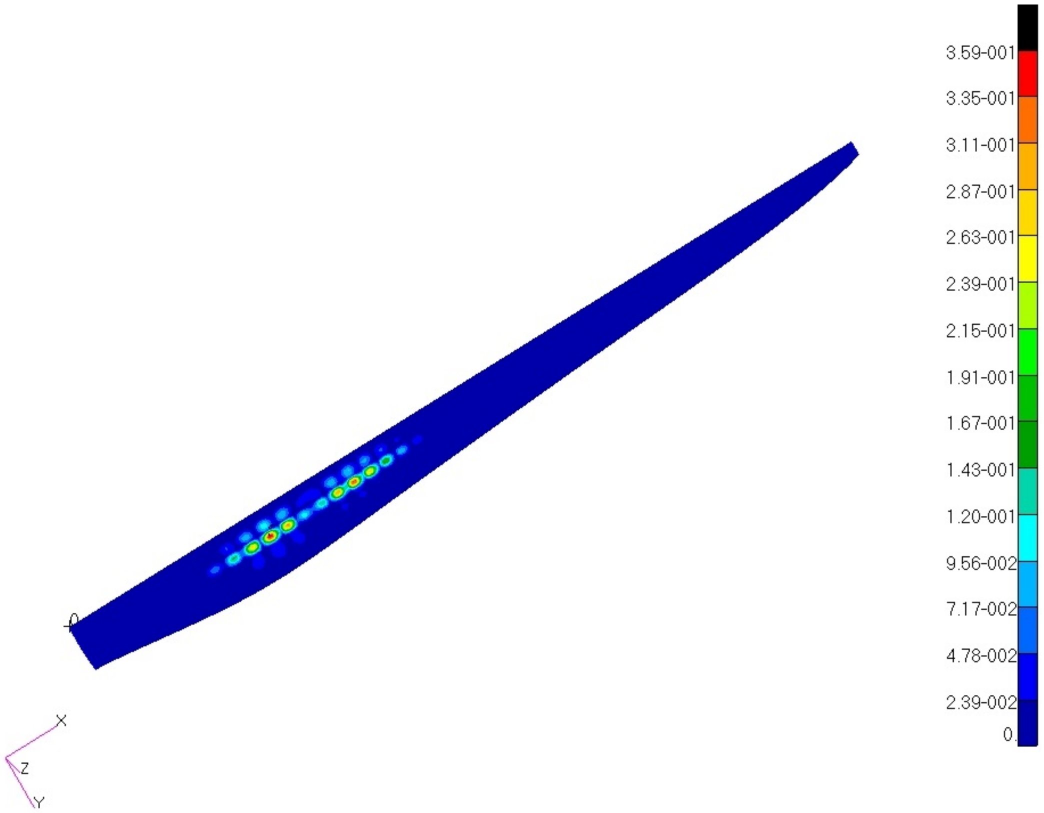

Figure A.2: Second buckling mode for the initial design of the conventional blade

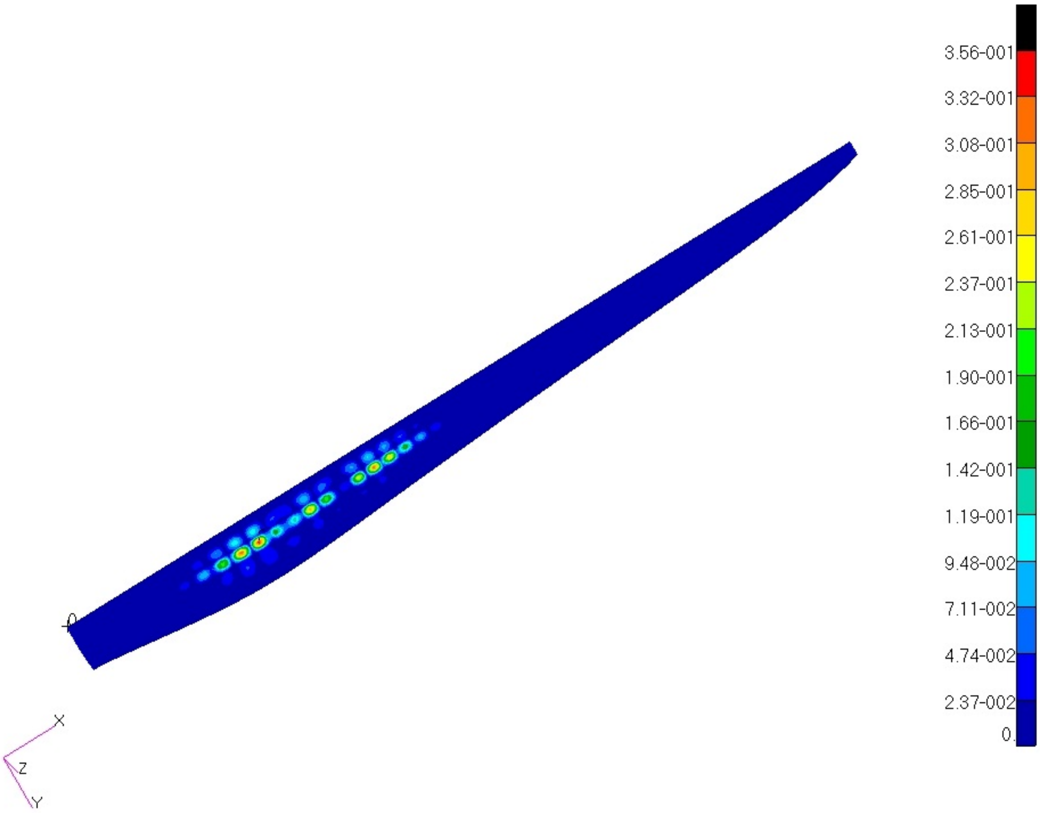

Figure A.3: Third buckling mode for the initial design of the conventional blade

Appendix B

Campbell Diagrams of Optimized Designs

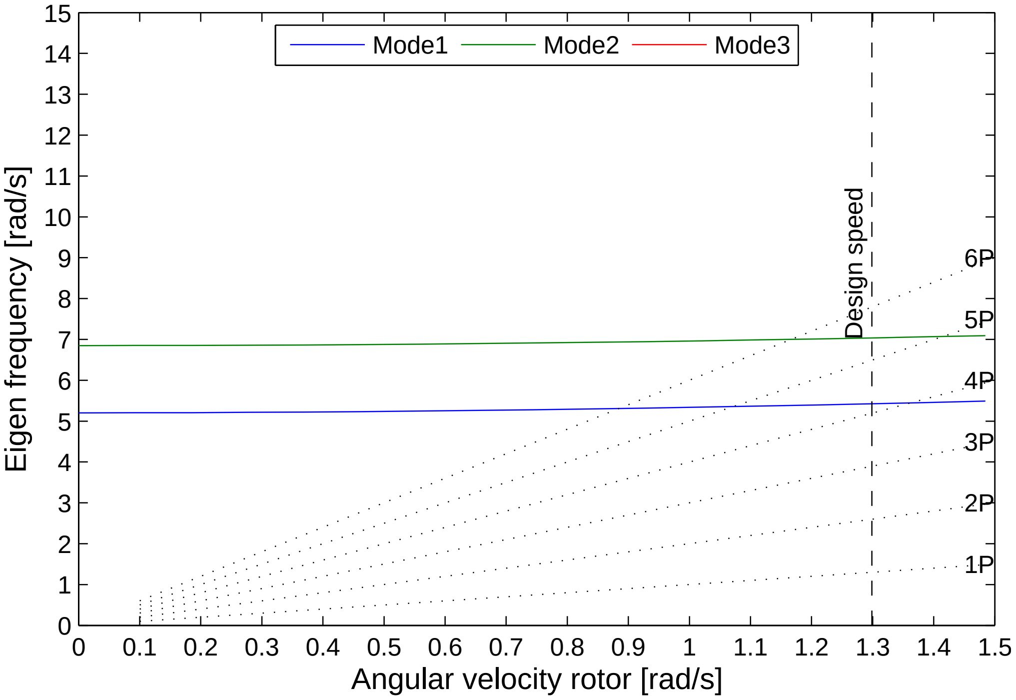

Figure B.1: Campbell diagram of the US TD FA blade

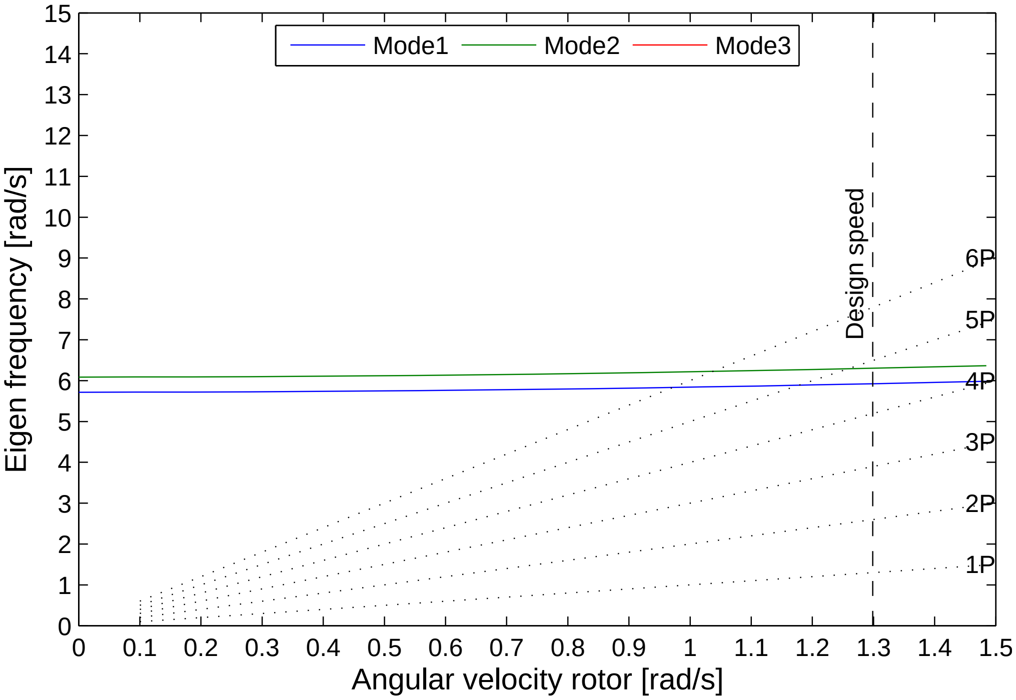

Figure B.2: Campbell diagram of the US-BU-TD-FA blade

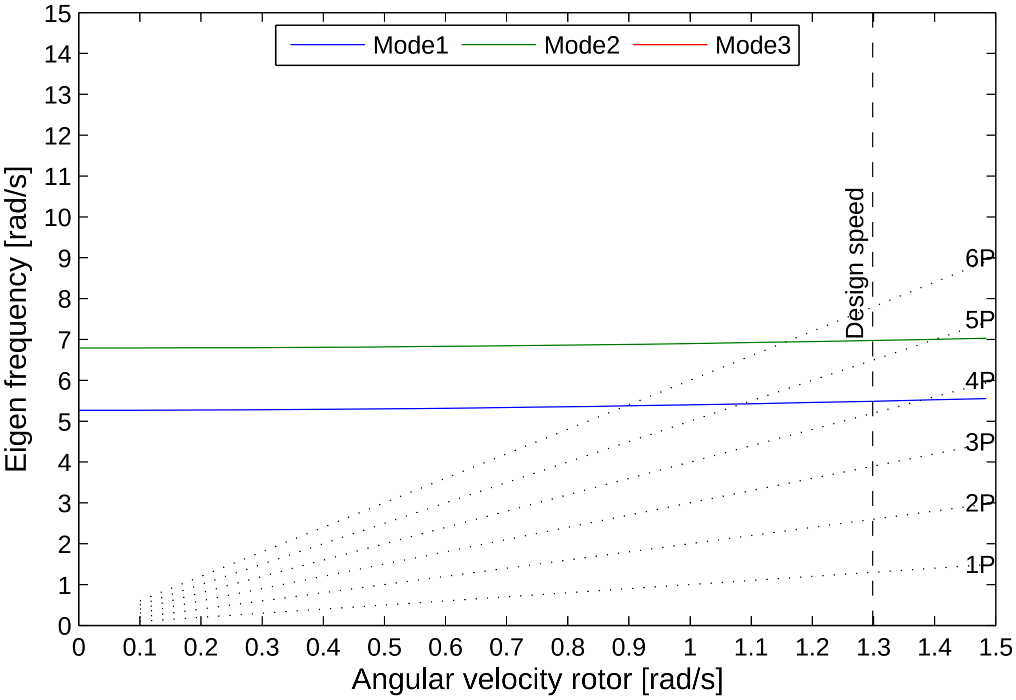

Figure B.3: Campbell diagram of the SR-US-TD-FA blade

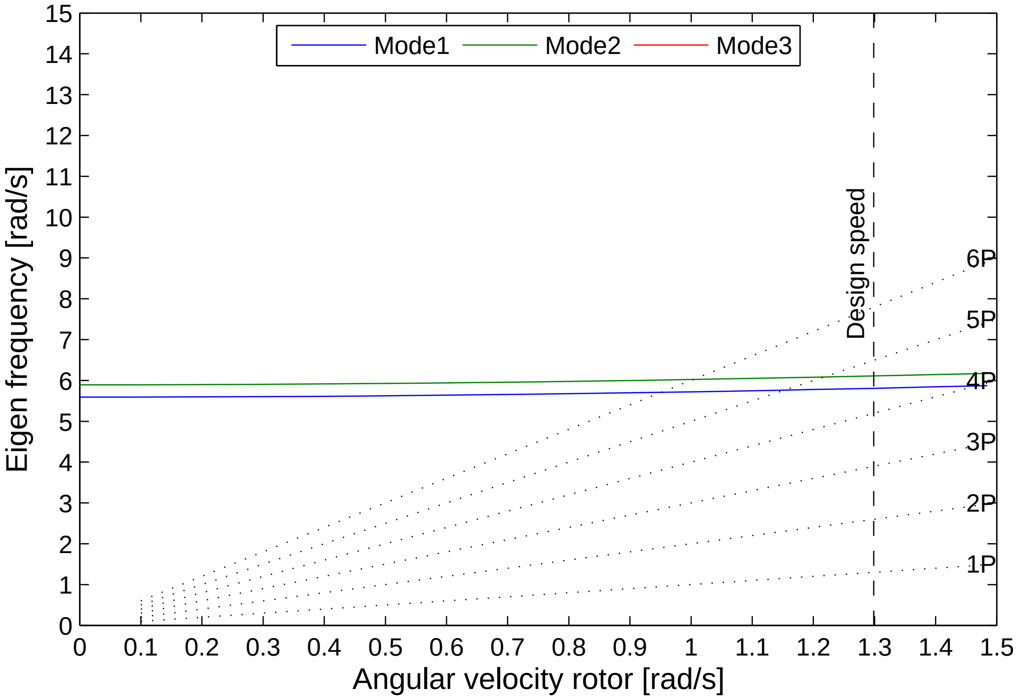

Figure B.4: Campbell diagram of the SR-US-BU-TD-FA blade

Appendix C

Scripts flowchart

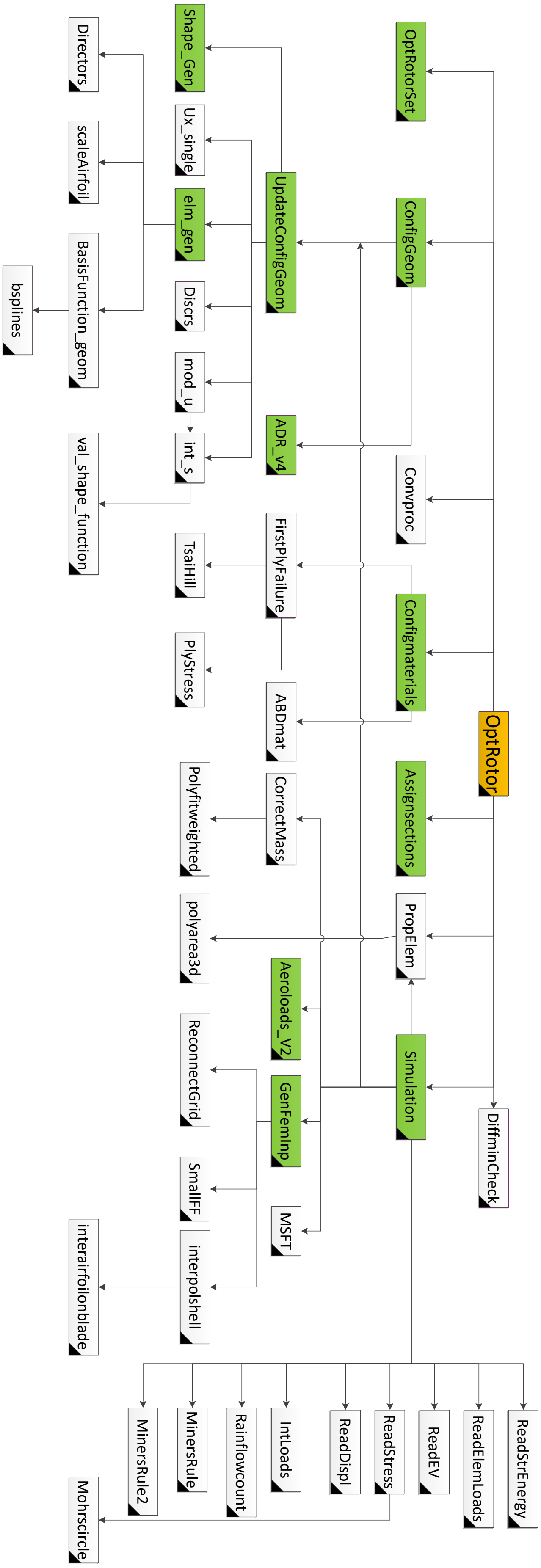

Figure C.1: Scripts flowchart